

**APPLICATIONS OF PLASMONICS IN TWO DIMENSIONAL
MATERIALS & THIN FILMS**

by

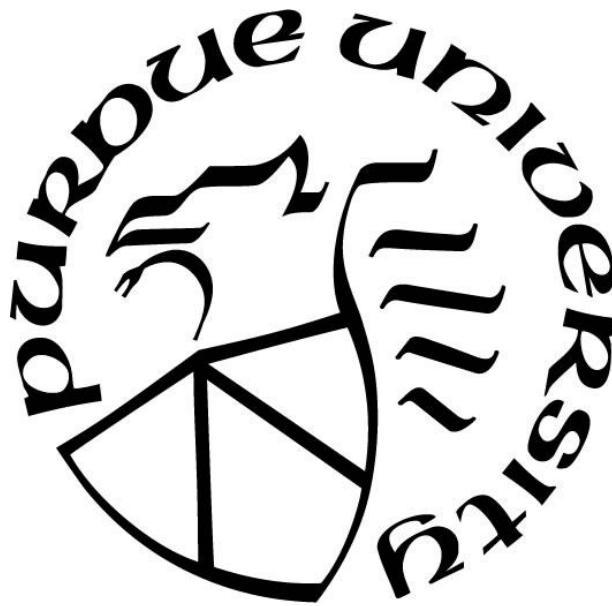
Prabhu Kumar Venuthurumilli

A Dissertation

Submitted to the Faculty of Purdue University

In Partial Fulfillment of the Requirements for the degree of

Doctor of Philosophy



School of Mechanical Engineering

West Lafayette, Indiana

May 2021

THE PURDUE UNIVERSITY GRADUATE SCHOOL

STATEMENT OF COMMITTEE APPROVAL

Dr. Xianfan Xu, Chair

School of Mechanical Engineering

Dr. Jong H. Choi

School of Mechanical Engineering

Dr. Liang Pan

School of Mechanical Engineering

Dr. Peide Ye

School of Electrical and Computer Engineering

Approved by:

Dr. Nicole Key

ACKNOWLEDGMENTS

I would like to sincerely thank my advisor Prof. Xianfan Xu for his guidance and support during my PhD. He has given me opportunity to work in this exciting world of plasmonics and 2D materials. I thank him for the privilege given to me to learn the clean room fabrication and many other things. I also express my gratitude to Prof. Piede Ye, Prof. Liang Pan, and Prof. Jong Hyun Choi for serving on my advisory committee. I acknowledge my collaborators Dr. Xiaolei Wen for near-field measurements and Vasudevan Iyer for building the setup for optical measurements. I am particularly grateful to Prof. Piede Ye for the valuable discussion on black phosphorus project and Prof. Yong Chen and his group for growing the bismuth telluride selenide samples. I would like to acknowledge Zhou Zeng, Nick Winovich and Prof. Guang Lin for the collaborative efforts on HAMR project.

I would like to thank all my friends and colleagues for their wonderful support during my stay at Purdue. I am thankful to my officemates Anurup, Emroz, Mauricio, Paul, Shouyuan, Vasu and Zhou for the numerous discussions. I am grateful to Luis, Woongsik and Yexin for teaching me clean room work and Anurup for teaching me HFSS simulations and near-field measurements. I would like to thank Roger for teaching optical measurements and techniques and thank Gang and Yexin for teaching me photocurrent measurements. I am grateful to Krishnakali, Rahul and Vaibhav for the valuable discussions on black phosphorus project and would like to thank Aaditya, Harsha, Koushik, Rahul and Vasu for their help on bismuth telluride selenide project. I am thankful to Gang, Harsha, Krishnakali, Naeem, Prof. Yi Xuan, Punya, Rahul, Vaibhav and many others for their cleanroom help. I would like to thank Anurup, Saaketh for all the discussions on HAMR project. I owe special thanks to Rahul for all his help and valuable discussions. I would like to thank all my lab mates for their assistance.

I would like to acknowledge all my friends who supported me in various ways throughout this journey. At the end, I would like to express my deep gratitude to my parents for their love, sacrifice, support, and encouragement at every step of my life.

TABLE OF CONTENTS

LIST OF TABLES	6
LIST OF FIGURES	7
ABSTRACT.....	13
1. INTRODUCTION	15
1.1 Surface Plasmons	16
1.1.1 Surface Plasmon Polaritons at the Plane Interface	16
1.1.2 Localized Surface Plasmons	20
1.2 Two-Dimensional Materials	23
1.3 Topological Insulators	24
1.4 Heat Assisted Magnetic recording	26
1.5 Outline of the Report	28
2. PLASMONIC RESONANCE ENHANCED POLARIZATION SENSITIVE PHOTO DETECTION BY BLACK PHOSPHORUS	29
2.1 Introduction.....	29
2.2 Design of plasmonic structures.....	32
2.3 Fabrication of Plasmonic Devices	39
2.4 Experimental Results	44
2.5 Summary	55
3. NEAR-FIELD IMAGING OF SURFACE PLASMONS FROM THE BULK AND SURFACE STATE OF THE TOPOLOGICAL INSULATOR BISMUTH TELLURIDE SELENIDE	57
3.1 Introduction.....	57

3.2	Optical Measurements and Modelling of Optical constants	60
3.3	Imaging of the Surface Plasmons from the Bulk	65
3.4	Imaging of the Surface Plasmons from the Surface State.....	71
3.5	Summary	76
4.	INVERSE DESIGN OF NEAR-FIELD TRANSDUCER FOR HEAT- ASSISTED MAGNETIC RECORDING USING TOPOLOGY OPTIMIZATION.....	77
4.1	Introduction.....	77
4.2	Inverse thermal and electromagnetic design.....	78
4.3	Inverse design for generating a heat spot of 30 nm x 60 nm in recording medium.....	82
4.4	Generating smallest heated spot in the recording medium	86
4.5	Generating heated spot with higher aspect ratio	88
4.6	Effect of waveguide in HAMR model	90
4.7	Effect of write pole in HAMR model	93
4.8	Effect of moving recording medium.....	96
4.9	Summary	105
5.	SUMMARY AND FUTURE WORK	106
5.1	Summary	106
5.2	Ongoing work	107
5.3	Future work.....	114
	REFERENCES	116
	VITA.....	133
	PUBLICATIONS.....	134

LIST OF TABLES

Table 3-1 Parameters of Tauc-Lorentz & Drude model fitted to the optical measurements.....	63
Table 4-1 Heated spot size and gradients along both the axes at 430 K and 400 K, with different rectangular targeted heated spot size, and the corresponding power required for peak temperature rise of 450 K.....	87
Table 4-2 The effect of curvature in NFT. All scale bars are 50 nm.	88
Table 4-3 Heated spot size and gradients along both the axes at 430 K and 400 K, with different targeted heated spot size for generating high aspect ratio heated spot in the recording medium, and the corresponding power required for peak temperature rise of 450 K.	89
Table 4-4 Temperature hot spot area and gradient along both axes at 430 K, and the power required to generate the hot spot with and without a waveguide.	92
Table 4-5 Temperature hot spot area and gradient along both axes at 400 K, with and without a waveguide.	93
Table 4-6 Temperature hot spot area and gradient along both axes at 430 K and 400 K, and the power required to generate the hot spot with and without the write pole.....	96
Table 4-7 The temperature hot spot size and gradients for scaled temperature rise at 430 K and 400 K along both x and y axes, for $h = 2 \times 10^8 \text{ W/m}^2\text{K}$	104
Table 4-8 The temperature hot spot size and gradients for scaled temperature rise at 430 K and 400 K along both x and y axes, for $h = 2 \times 10^7 \text{ W/m}^2\text{K}$	104

LIST OF FIGURES

Figure 1.1 Plasmonics: Synergy between photonic and electronic devices. Adopted from [1]. ..	16
Figure 1.2 SPP at the interface of a metal and dielectric	17
Figure 1.3 Dispersion of SPP at the interface of dielectric and metal (a) loss less Drude metal with air and silica (b) silver, Silver/air and Silver/silica interface. Adopted from [4].	20
Figure 1.4 Homogenous sphere in a dielectric medium with uniform static electric field	21
Figure 1.5 Scattering spectra of single silver nano particle of various shapes. Adopted from [5].	22
Figure 1.6 Band structure of Graphene. Adopted from [16].....	23
Figure 1.7 Schematic of the band structure of 3D topological insulator	25
Figure 1.8 (a) Schematic of write process in HAMR. Adopted from [34]. b) Schematic of HAMR head. Adopted from [31].	27
Figure 2.1 Lattice structure of BP. Adopted from [56].....	30
Figure 2.2 Comparison of bandgap of black phosphorus with other two dimensional and conventional semiconductors. Adopted from [60].	31
Figure 2.3 Optical property of BP: Optical transmittance T, reflectance R, and absorptivity A, of (a) 64 nm thick BP, (b) 145 nm thick BP, at 1550 nm wavelength along armchair and zigzag directions.	34
Figure 2.4 Simulated response of a BP device with bowtie antenna array. (a) Schematic of a unit cell of the simulation model. (b) Calculated absorption in BP, with and without bowtie structures when illuminated along the armchair direction. (c) Electric field distributions (i) top view of the XY plane at the exit of bowtie antenna, (ii) cross-sectional view of the XZ plane, and (iii) cross-sectional view of the YZ plane, for illuminations along the armchair and zigzag directions at 1550 nm wavelength.	35
Figure 2.5 Absorption in BP by varying the different dimensions of bowtie antenna. (a) Length (b) Period y.	36
Figure 2.6 Simulated response of a BP device with array of bowtie apertures. (a) Schematic of a unit cell of the simulation model. (b) Calculated absorption in BP with the fabricated dimensions for two different polarizations, armchair (along the y-direction of figure 6a) and zigzag (along the x-direction of figure 6a). (c) Electric field distributions (i) top view of the XY plane at the exit of bowtie aperture, (ii) cross-sectional view of the YZ plane, and (iii) cross-sectional view of the XZ	

plane, for illuminations along the armchair and zigzag directions.	37
Figure 2.7 Percentage of absorption in BP vs. wavelength by varying the different dimensions of bowtie aperture. (a) length (b) width.	38
Figure 2.8 Calculated absorption in BP for the bowtie aperture design with armchair polarization, (a) Different in plane optical constants at 64nm and 145 nm. (b) Sensitivity of BP absorption vs. dielectric constant for the armchair polarization.	39
Figure 2.9 Liftoff of bowtie apertures on Silicon substrate (without acetone gun).....	40
Figure 2.10 Lift off using acetone gun (a) Without ultrasonic (b) With ultrasonic for 2 seconds.	41
Figure 2.11 Bowtie antenna BP photodetector. (a) Optical image of two BP devices on one flake, (i) without plasmonic nanostructures and (ii) with array of bowtie antennas. (b) Scanning Electron Microscopy (SEM) image of array of bowtie antenna structures. Scale bar is 2 μm . (c) AFM height profile across the boundary of the BP flake (green line in the inset). Inset shows the AFM topography image of the BP flake. (d) Polarized Raman spectra for identifying the armchair direction in BP (the x – direction in Figure 2.11a).	42
Figure 2.12 Bowtie aperture BP photodetector. (a) Optical image of the BP photodetector with the array of bowtie apertures. (b) (i) SEM image of array of bowtie apertures and contacts on the BP flake. Scale bar is 1 μm . (ii) Zoomed in image of the array of bowtie apertures. Scale bar is 1 μm . (c) AFM topography image of the BP flake. Inset shows the AFM height profile of the green line.	43
Figure 2.13 Schematic of the bowtie antenna and bowtie aperture photodetector	44
Figure 2.14 Experimental setup of photo detection	45
Figure 2.15 Dark current of the device with bowtie antennas and without bowtie antennas	46
Figure 2.16 Response of bowtie antenna BP photodetector at 1550 nm wavelength (a) Photocurrent map of device with plasmonic structures at zero bias, with 470 μW incident laser power. Scale bar is 20 μm . (b) Illumination current minus dark current ($I_{\text{light}} - I_{\text{dark}}$) vs. bias voltage at 1.05mW of laser power for both devices, with and without bowtie antennas, and both polarizations along armchair and zigzag directions. (c) Photocurrent vs. laser power at 150 mV bias. (d) Photoresponsivity vs. laser power at 150 mV bias.	48
Figure 2.17 Scanning photocurrent measurements (a-e) Photocurrent maps with 470 μW incident power at 1550 nm wavelength. (a) With bowtie antennas at zero bias, zigzag polarization. (b) With bowtie antennas at 100 mV bias, zigzag polarization. (c) Without bowtie antennas at 100 mV bias, zigzag polarization. (d) With bowtie antennas at 100 mV bias, armchair polarization. (e) Without bowtie antennas at 100 mV bias, armchair polarization. (f) Photocurrent map with 200 μW incident power at 633 nm wavelength in the device with bowtie antennas, at zero bias and with armchair polarization. All Scale bars: 20 μm and color bars in μA	49

Figure 2.18 Transient current measurement of device with bowtie structures at 100mV bias, for armchair polarization at different modulating frequencies.	51
Figure 2.19 Polarization ratio vs. power for both devices, with and without bowtie antennas at 150 mV bias.	52
Figure 2.20 Response of the bowtie aperture photodetector. (a) Dark current and illumination current at 580 μ W vs. voltage for different polarizations at 1550 nm. (b) Photocurrent vs. power at 150 mV bias for different polarizations at 1550 nm. (c) Responsivity vs. power at 150 mV bias for different polarizations at 1550 nm. (d) Comparing polarization ratio vs. laser power at 150 mV bias, with and without bowtie apertures (BA) and at wavelengths of 1550 nm and 633 nm.	53
Figure 2.21 Dark current and illumination current at 470 μ W vs. voltage for different polarizations of a bowtie aperture photodetector.	54
Figure 3.1 Lattice structure of BTS. Adopted from [26]	58
Figure 3.2 Schematic of the band structure of BTS. Adopted from [26].	59
Figure 3.3 Raman characterization of BTS flakes on SiO ₂ /Si substrate.	60
Figure 3.4 Optical measurements of BTS flake. (a) , (b) Reflectance and transmittance of 15 nm BTS flake on CaF ₂ substrate and (c) , (d) Reflectance and transmittance of 55 nm BTS flake on undoped Si substrate. R _{exp} and T _{exp} are the experimental reflectance and transmittance respectively. R _{model} and T _{model} are the reflectance and transmittance from the fitted dielectric constants.	61
Figure 3.5 Dielectric constants of BTS. (a) Bulk BTS. The inset shows the dielectric constants of the surface layer and (b) enlarged view of the bulk BTS properties in the visible and near IR region.	64
Figure 3.6 Absorption measured using FTIR on a 55nm BTS flake on Si substrate. A _{exp} is the experimental absorption and A _{model} is from the model.	65
Figure 3.7 Near-field amplitude image at 633 nm obtained using scattering NSOM. (i) AFM topography, (ii) NSOM amplitude, and (iii) amplitude profile of the blue line in figure ii, for different BTS flakes. (a) 77 nm thick and (b) 15 nm thick.	66
Figure 3.8 Near-field amplitude image at 633 nm on 63 nm thick flake. (i) AFM topography, (ii) NSOM amplitude, and (iii) amplitude profile of the blue line in figure ii.	67
Figure 3.9 Comparison of the numerical and experimental results at 633 nm. (a) Numerical calculation of a Gaussian beam of radius 2 μ m radiating on the nanoslit. Scale bar is 1 μ m. (i) Geometry of the simulation showing the slit. (ii) Electric field distribution on a plane, 2 nm above surface. (iii) Line profile of E _z at the center of the plane (along the x-axis) 2 nm above the surface. (b) Near-field amplitude image at 633 nm using scattering-type NSOM (i) AFM topography (ii) s-NSOM amplitude (iii) Amplitude profile of the black line in Fig. b(ii).	69

Figure 3.10 Line profile of the near-field amplitude on incident light side of the slit at 633 nm, using scattering-type NSOM for different slit orientation with in-plane component of incident light for 77 nm thick flake. Orientation (φ) of (a) 5° (b) 50° (c) 70° .	70
Figure 3.11 Near-field amplitude image at 10.6 μm using scattering-type NSOM. (i) AFM topography, (ii) s-NSOM amplitude, and (iii) Amplitude profile of the white line in figure ii, for different BTS flakes. (a) 15 nm thick and (b) 77 nm thick. All scale bars are 200 nm.	72
Figure 3.12 Near-field amplitude image at 10.6 μm on 63 nm thick flake. (i) AFM topography, (ii) NSOM amplitude, and (iii) amplitude profile of the yellow line in figure ii.	72
Figure 3.13 Line scans of near-field measurement at 10.6 μm wavelength for (a) 15 nm flake and (b) 77 nm flake. For both the flakes, (i) near-field signal (scale bar = 200 nm) and (ii) Line scan of the (displaced) near-field signal across the white lines shown in (i).	73
Figure 3.14 Fourier Transform of the line scan of the near-field signal at 10.6 μm wavelength for (a) 15 nm flake and (b) 77 nm flake.	74
Figure 4.1 Schematic of HAMR system considered in electromagnetic field simulation (a) Side view; Stack from incident light side: air, 60 nm-thick NFT (gold), 4 nm-thick air, 10 nm-thick FePt, air. (b) Top view showing the simulation domain of 500 nm x 500 nm, the design region of NFT 200 nm x 200 nm, and the field reconstructing region of 300 nm x 300 nm at the mid plane in the FePt medium which is also shown by the dotted line in (a).	79
Figure 4.2 Inverse thermal calculation for generating a 30 nm x 60 nm heat spot (a) Obtained volumetric heat generation (W/m^3). The inset shows the isometric view of the normalized volumetric heat generation (b) Temperature rise (K) in the recording medium with the volumetric heat generation in Figure 4.2a (c) Temperature rise along the x – axis in Figure 4.2b (d) Temperature rise along y – axis in Figure 4.2b.	83
Figure 4.3 Density evolution of NFT and the final NFT design for generating a targeted heated spot of 30 nm x 60 nm in the recording medium. Density 1 represents gold and 0 represents air (aperture). All scale bars are 50 nm.	84
Figure 4.4 Thermal calculations with the obtained NFT design for the targeted heated spot of 30 nm x 60 nm (a) Volumetric heat generation (W/m^3) in the recording medium with the obtained NFT design. (b) Scaled temperature rise (K) of recording medium with the obtained NFT design. (c) Temperature rise along the x – axis in Figure 4.4b. (d) Temperature rise along y – axis in Figure 4.4b.	85
Figure 4.5 Generating smaller heated spot in the recording medium, with different targeted heated spot size of (a) 30 nm x 60 nm, (b) 25 nm x 50 nm, (c) 20 nm x 40 nm, (d) 15 nm x 30 nm, (e) 10 nm x 20 nm, and (f) 8 nm x 16 nm. The obtained designs of NFTs are shown on the left and the scaled temperature rises in the recording medium are shown on the right for each case. All scale bars are 50 nm.	86

Figure 4.6 Generating high aspect ratio heated spot in the recording medium, with different targeted heated spot size of (a) 10 nm x 20 nm, (b) 10 nm x 30 nm, (c) 10 nm x 40 nm, (d) 10 nm x 60 nm, (e) 10 nm x 80 nm, and (f) 10 nm x 100 nm. The obtained designs of NFT are shown on the left and the scaled temperature rise in the recording medium are shown on the right for each case. All scale bars are 50 nm.	89
Figure 4.7 Adding 600 nm x 300 nm Ta ₂ O ₅ waveguide to the obtained design for a targeted heat spot of 10 nm x 80 nm (a) Schematic (b) Electric field distribution (i) at the exit plane of waveguide (ii) at the exit of the waveguide.	91
Figure 4.8 Temperature rise (K) in the recording medium with 600 nm x 300 nm Ta ₂ O ₅ waveguide	91
Figure 4.9 Adding 600 nm x 600 nm Ta ₂ O ₅ waveguide to the obtained design for a targeted heat spot of 10 nm x 80 nm (a) Electric field distribution at the exit plane of waveguide (ii) Temperature rise (K) in the recording medium.....	92
Figure 4.10 Adding the write pole to the obtained design for a targeted heat spot of 10 nm x 80 nm (a) Schematic (b) Top view showing CoFe write pole (red) and NFT (yellow).....	94
Figure 4.11 Adding CoFe write pole to the obtained design with a targeted heat spot of 10 nm x 80 nm (a) Electric field distribution at the center plane of FePt. (b) Zoomed in view of electric field shown in Figure 4.11a	95
Figure 4.12 Temperature rise (K) in the recording medium (a) Without write pole (b) With write pole.....	95
Figure 4.13 Temperature (K) of the stationary recording medium (a) At 1 ns (b) At 2 ns.	97
Figure 4.14 Temperature (K) of recording medium moving with a horizontal velocity of 10 m/s (a) At 1 ns (b) At 2 ns (c) 4 ns (d) 6 ns (e) 8 ns (f) 10 ns.	98
Figure 4.15 Temperature profile of the recording medium (a) Actual temperature (b) Displacing the temperature profiles by the displacement (c) Normalizing the curves in Figure 4.15b.....	99
Figure 4.16 Temperature (K) of the stationary recording medium with h (a) At 1 ns (b) At 2 ns.	101
Figure 4.17 Temperature (K) of the recording medium with a horizontal velocity of 10 m/s, with h (a) At 1 ns (b) At 2 ns (c) 4 ns (d) 6 ns (e) 8 ns (f) 10 ns.....	102
Figure 4.18 Comparing the temperature of moving and stationary recording medium with h. (a) Moving medium (b) Stationary medium (c) Temperature along the x and y axes for moving medium (d) Temperature along the x and y axes for stationary medium.	103
Figure 5.1 Schematic of generation of NFT designs (a) Choosing the random points for generation of radial basis function (b) Radial basis functions generated at these points are summed up. (c)	

Choosing the cutoff value decides the location of aperture. (d) Schematic of aperture in the first quadrant. (e) Schematic of the aperture of the design by performing symmetry operations..... 109

Figure 5.2 Schematic of the neural network training procedure..... 110

Figure 5.3 Forward calculation for one case (a) NFT design, where blue region indicates the aperture. (b) Temperature rise (K) in the recording medium for NFT design shown in Figure 5.3a. 111

Figure 5.4 Simulation results of 100 randomized designs. 112

Figure 5.5 Preliminary results of neural network from validation data. (a) and (b) show the results for two NFT designs. (i) Shows the prediction from the neural network and the solution. (ii) Shows the error in prediction by neural network. 113

Figure 5.6 Surface plasmon resonance in graphene at mid IR wavelengths. (a) SEM image of graphene nanoribbons (b) Extinction spectra of the graphene nanoribbons. Adopted from [144]. 114

ABSTRACT

The demand for the faster information transport and better computational abilities is ever increasing. In the last few decades, the electronic industry has met this requirement by increasing the number of transistors per square inch. This lead to the scaling of devices to tens of nm. However, the speed of the electronics is limited to few GHz. Using light, the operating speed of photonic devices can be much larger than GHz. But the photonic devices are diffraction limited and hence the size of photonic device is much larger than the electronic components. Plasmonics is an emerging field with light-induced surface excitations, and can manipulate the light at nanoscale. It can bridge the gap between electronics and photonics.

With the present scaling of devices to few nm, the scientific community is looking for alternatives for continued progress. This has opened up several promising routes recently, including two-dimensional materials, quantum computing, topological computing, spintronics and valleytronics. The discovery of graphene has led to the immense interest in the field of two-dimensional materials. Two dimensional-materials have extraordinary properties compared to its bulk. This work discusses the applications of plasmonics in this emerging field of two-dimensional materials and for heat assisted magnetic recording.

Black phosphorus is an emerging low-direct bandgap two-dimensional semiconductor, with anisotropic optical and electronic properties. It has high mobility and is promising for photo detection at infrared wavelengths due to its low band gap. We demonstrate two different plasmonic designs to enhance the photo responsivity of black phosphours by localized surface plasmons. We use bowtie antenna and bowtie apertures to increase the absorption and polarization selectivity respectively. Plasmonic structures are designed by numerical electromagnetic simulations, and are fabricated to experimentally demonstrate the enhanced photo responsivity of black phosphorus.

Next, we look at another emerging two-dimensional material, bismuth telluride selenide ($\text{Bi}_2\text{Te}_2\text{Se}$). It is a topological insulator with an insulating bulk but conducting electronic surface states. These surface states are Dirac like, similar to graphene and can lead to exotic plasmonic phenomena. We investigated the optical properties of $\text{Bi}_2\text{Te}_2\text{Se}$ and found that the bulk is plasmonic below 650 nm wavelength. We study the distinct surface plasmons arising from the bulk and surface state of the topological insulator, $\text{Bi}_2\text{Te}_2\text{Se}$. The propagating surface plasmons at a nanoscale slit in $\text{Bi}_2\text{Te}_2\text{Se}$ are imaged using near-field scanning optical microscopy. The surface state plasmons are studied with a below band gap excitation of 10.6 μm wavelength and the surface plasmons of the bulk are studied with a visible wavelength of 633 nm. The surface state plasmon wavelength is 100 times shorter than the incident wavelength in sharp contrast to the plasmon wavelength of the bulk.

Next, we look at the application of plasmonics in heat assisted magnetic recording (HAMR). HAMR is one of the next generation data storage technology that can increase the areal density to beyond 1 Tb/in². Near-field transducer (NFT) is a key component of the HAMR system that locally heats the recording medium by concentrating light below the diffraction limit using surface plasmons. In this work, we use density-based topology optimization for inverse design of NFT for a desired temperature profile in the recording medium. We first perform an inverse thermal calculation to obtain the required volumetric heat generation (electric field) for a desired temperature profile. Then an inverse electromagnetic design of NFT is performed for achieving the desired electric field. NFT designs for both generating a small heated spot size and a heated spot with desired aspect ratio in recording medium are demonstrated. The effect of waveguide, write pole and moving recording medium on the heated spot size is also investigated. The ongoing efforts explore the design of near-field transducer for HAMR using machine learning.

1. INTRODUCTION

The rapid growth of the electronics industry has led to the development of the high speed microprocessors and better computation capabilities. Our lives are propelled by the faster information transport and better processing abilities. Till date, this ever-increasing demand is met by doubling the number of transistors per square inch of an integrated circuit for every two years (Moore's law). This has led to the smaller critical dimension (few nms) of the devices. The operating speed and the critical device dimensions of the present day semiconductor electronics [1] is shown in Figure 1.1. However, scaling of these devices has led to two major challenges, heat generation and the signal delay by the electronic interconnects [2]. As the data rates and the packaging density of the components increase, electrical interconnects are limited by the RC delay [2]. Hence the operating speed of the semiconductor electronics is limited to ~ 10 GHz [1]. Optical interconnects are promising for the high-speed links between the computing units. In the optical communications, bit rate is fundamentally limited by the carrier frequency and can reach the higher operating speeds as compared to the semiconductor electronics [2]. However, the light propagation in these dielectric photonic components is subjected to diffraction. Hence the size of these devices is about two orders of magnitude larger than the electronic components and would be difficult for integration of both the devices due to size mismatch [3]. Plasmonics is an emerging field with light-induced surface excitations, and can manipulate the light at nanoscale by exploiting the optical properties of metallic nanostructures [3]. As shown in the Figure 1.1, Plasmonics can bridge the gap between the semiconductor electronics and dielectric photonics, with similar size of the semiconductor electronics and the operating speed of the photonics [1]. By integrating all these plasmonic, dielectric photonics and semiconductor electronics on the same chip, synergy can be attained by taking the advantage of each technology [3].

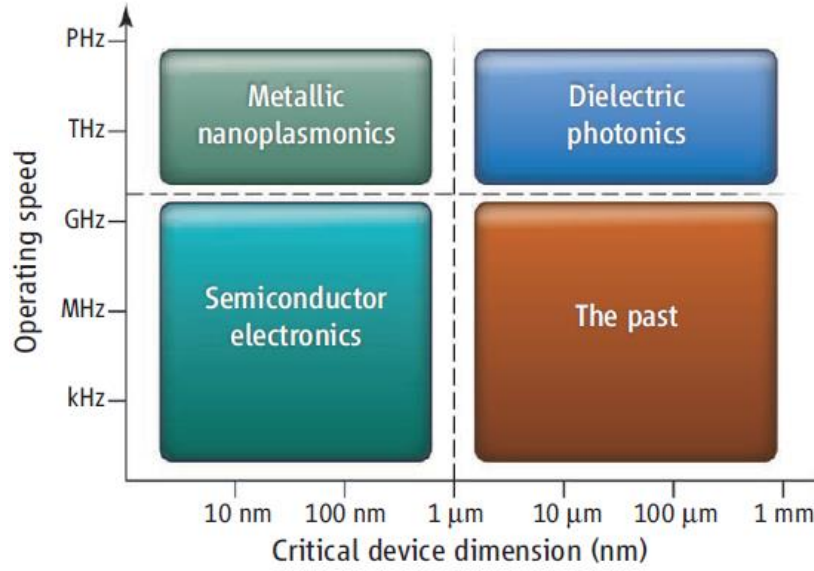


Figure 1.1 Plasmonics: Synergy between photonic and electronic devices. Adopted from [1].

1.1 Surface Plasmons

Surface plasmons (SP) are the electromagnetic oscillations at the interface of a dielectric and a conducting medium. Surface plasmons can be bound along the interface in either two or three dimensions. Surface plasmons which are bound in two directions and propagate along the interface are called surface plasmon polaritons (SPP) or propagating surface plasmons. But the surface plasmons which are bound in all three dimensions and confined to the surface are called localized surface plasmons (LSP).

1.1.1 Surface Plasmon Polaritons at the Plane Interface

SPP can exist at the interface of the dielectric and conducting medium. Consider the interface of a metal $\epsilon_1 = \epsilon'_1 + i\epsilon''_1$ (medium 1, $\epsilon'_1 < 0$ for metal) and non-absorbing dielectric ϵ_2 (medium 2) as shown in Figure 1.2. Surface plasmons can only exist for the TM polarization. They are confined to the surface and the electromagnetic fields of the surface plasmons decay in both the media from the interface as shown in Figure 1.2.

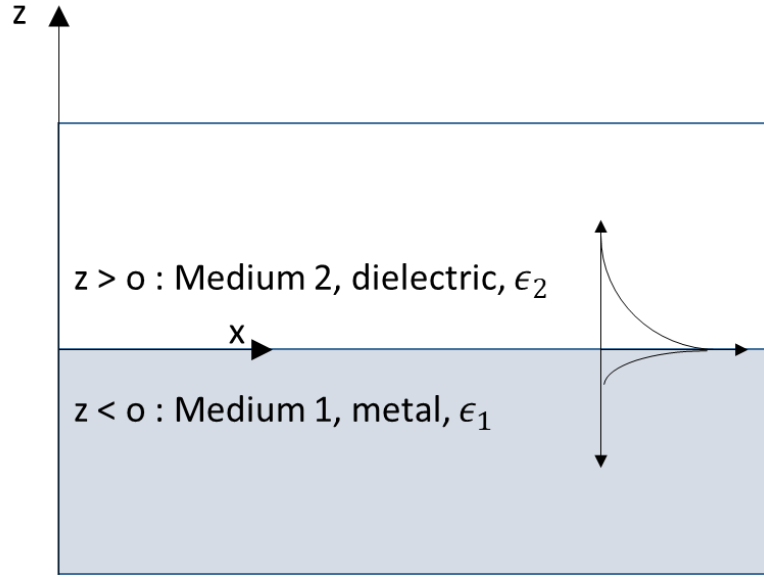


Figure 1.2 SPP at the interface of a metal and dielectric

The electric (E_x , E_z) and magnetic fields (H_y) decaying with z (away from interface) are given as [4] ,

In Medium2: ($z > 0$)

$$H_y(z) = A_2 e^{i\beta x} e^{-k_2 z} \quad (1.1)$$

$$E_x(z) = iA_2 \frac{1}{\omega \epsilon_0 \epsilon_2} k_2 e^{i\beta x} e^{-k_2 z} \quad (1.2)$$

$$E_z(z) = -A_1 \frac{\beta}{\omega \epsilon_0 \epsilon_2} e^{i\beta x} e^{-k_2 z} \quad (1.3)$$

In Medium1: ($z < 0$)

$$H_y(z) = A_1 e^{i\beta x} e^{k_1 z} \quad (1.4)$$

$$E_x(z) = -iA_1 \frac{1}{\omega \epsilon_0 \epsilon_1} k_1 e^{i\beta x} e^{k_1 z} \quad (1.5)$$

$$E_z(z) = -A_1 \frac{\beta}{\omega \epsilon_0 \epsilon_1} e^{i\beta x} e^{k_1 z} \quad (1.6)$$

where, β is the surface wave vector, k_i is the component of the wave vector perpendicular to the interface in the i^{th} media, A_i is the amplitude of the magnetic field in i^{th} media.

From the Maxwell equations and the continuity of the fields at the interface, we obtain that

$$A_1 = A_2 \quad (1.7)$$

$$\frac{k_2}{k_1} = -\frac{\epsilon_2}{\epsilon_1} \quad (1.8)$$

$$k_1^2 = \beta^2 - k_o^2 \epsilon_1 \quad (1.9)$$

$$k_2^2 = \beta^2 - k_o^2 \epsilon_2 \quad (1.10)$$

where, k_o is the wave vector in vacuum.

From equation (1.8) , we observe that $Re(\epsilon_1) < 0$ for the surface plasmons to exist at the interface of dielectric medium ϵ_2 . Hence surface plasmons can only exist at the interface of materials with opposite signs of real part of permittivity like metal and dielectric. Also a large negative value of ϵ_1 indicates a large k_1 , which means better confinement in the medium1.

From the equations (1.8)–(1.10), we obtain the dispersion of the surface plasmon polariton and is given by,

$$\beta = k_o \sqrt{\frac{\epsilon_1 \epsilon_2}{\epsilon_1 + \epsilon_2}} \quad (1.11)$$

The surface propagation vector can be complex, $= \beta' + i\beta''$, where β' and β'' are the real and imaginary part of the surface wave vector. The SPP wavelength (λ_{spp}) is given as $\frac{2\pi}{\beta'}$ and the SPP propagation length is given as $\frac{1}{2\beta''}$.

Consider a Drude metal without loss, ($\epsilon_1'' = 0$) and with a plasma frequency of ω_p , the frequency at which it is metallic for the frequencies below it ($\epsilon_1' < 0$). It is transparent for the frequencies above the plasma frequency and is non-metallic. The dielectric constant of lossless

Drude metal is given as $\epsilon_1(\omega) = 1 - \frac{\omega_p^2}{\omega^2}$. From the equation (1.11), we observe that at the frequency when $\epsilon_1(\omega) = -\epsilon_2$, $\beta \rightarrow \infty$ and the frequency is called surface plasmon frequency ω_{sp} and is given as $\omega_{sp} = \frac{\omega_p}{\sqrt{1+\epsilon_2}}$. The dispersion of the SPP at the interface of this metal, and a dielectric (for air $\epsilon_2 = 1$ and silica $\epsilon_2 = 2.25$) is shown in Figure 1.3 (a). We can see that $\beta \rightarrow \infty$ at the surface plasmon frequency. The dotted lines between the frequencies, surface plasmon frequency and plasma frequency show the prohibited propagation where β is imaginary. Also, it shows the radiative modes for the frequencies above the plasma frequency of the metal. In addition, it shows the light line (linear lines), the dispersion of the propagating waves in air and silica. Since the SPP are bound, the SPP excitations correspond to the region of the dispersion curves to the right of the respective light lines. At the frequencies where β is much larger than the light line, surface plasmon wavelength is much smaller than the incident wavelength. This explains the capability of sub-diffraction resolution by the surface plasmons. In metals with loss, β does not approach ∞ , but has a finite maximum value at the surface plasmon frequency. The dispersion at the interface of silver/air and silver/silica is shown in Figure 1.3b.

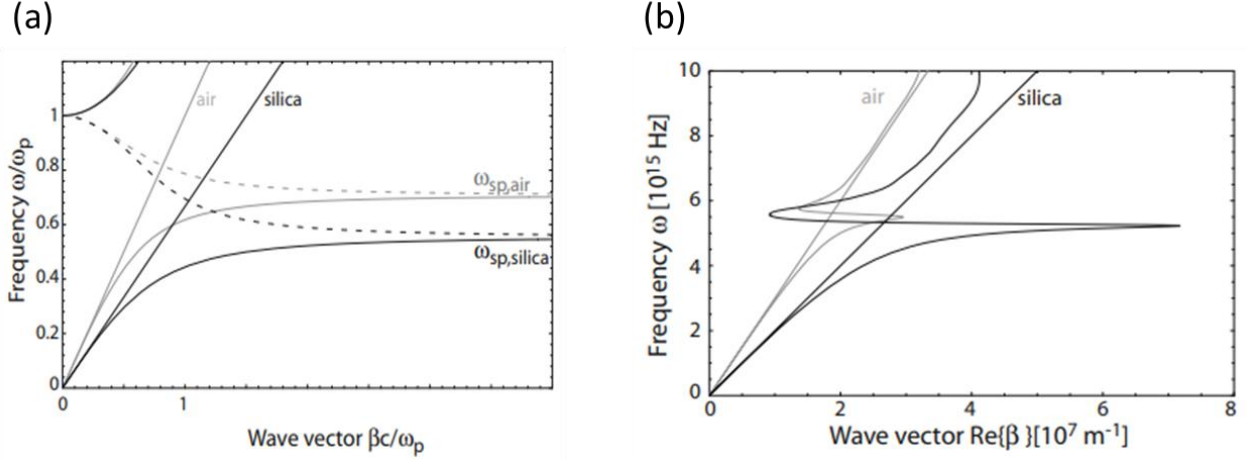


Figure 1.3 Dispersion of SPP at the interface of dielectric and metal **(a)** lossless Drude metal with air and silica **(b)** silver, Silver/air and Silver/silica interface. Adopted from [4].

But the SPP cannot be excited directly by the incident light due to the momentum mismatch between the light and SPP. So, different techniques are employed to provide the momentum such as prism coupling in Kretschmann and Otto configuration, and by grating coupling [4].

1.1.2 Localized Surface Plasmons

Localized surface plasmons are the non-propagating (localized) surface plasmons in metallic nanostructures. These are the excitation of conduction electrons in these nanostructures when coupled to electromagnetic field. Based on the geometry, optical properties of the metallic particles and the wavelength of the incident light, there could be a resonance of the electric field in the near-field of the nanostructures. Localized surface plasmons can be excited by direct light illumination.

Consider a metal sphere of radius a , with permittivity ϵ_1 at origin, surrounded by a dielectric medium ϵ_2 as shown in Figure 1.4, with static electric field of $E = E_0 \hat{z}$. The interaction of a metallic sphere whose radius is much smaller than the wavelength of the light ($a \ll \lambda$) can be analyzed by quasi-static approximation.

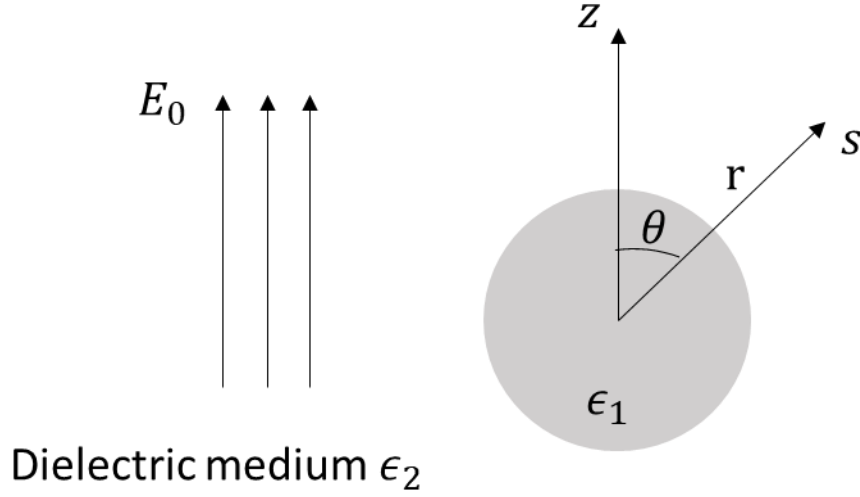


Figure 1.4 Homogenous sphere in a dielectric medium with uniform static electric field

The electrostatic potential ϕ , can be solved by the Laplace equation and the electric field can be obtained from the potential, $E = -\nabla\phi$. The potential inside and outside the sphere at point $s(r, \theta)$ is given as [4],

$$\phi_{in}(r, \theta) = -\frac{3\epsilon_2}{\epsilon_1 + 2\epsilon_2} E_0 r \cos\theta \quad (1.12)$$

$$\phi_{out}(r, \theta) = -E_0 r \cos\theta + \frac{\epsilon_1 - \epsilon_2}{\epsilon_1 + 2\epsilon_2} E_0 a^3 \frac{\cos\theta}{r^2} \quad (1.13)$$

The potential outside the sphere can be interpreted as the superposition of the potential due to the uniform field and a dipole at the center of the sphere, with dipole moment \mathbf{p} and the polarizability α given as,

$$\mathbf{p} = 4\pi\epsilon_0\epsilon_2 a^3 \frac{\epsilon_1 - \epsilon_2}{\epsilon_1 + 2\epsilon_2} \mathbf{E}_0 \quad (1.14)$$

$$\mathbf{p} = \epsilon_0\epsilon_2 \alpha \mathbf{E}_0 \quad (1.15)$$

$$\alpha = 4\pi a^3 \frac{\epsilon_1 - \epsilon_2}{\epsilon_1 + 2\epsilon_2} \quad (1.16)$$

The permittivity of the metal ϵ_1 is a function of light frequency ω . There is resonance in the polarizability when the $|\epsilon_1 + 2\epsilon_2|$ is minimum. This also creates the resonance of the dipolar fields, which decays with distance from the sphere. Also, the resonance in the polarizability leads to the resonance in the scattering and absorption cross-section of the nanoparticle.

Based on the geometry (like ellipsoid etc.) the coefficient in the denominator of equation (1.16) changes, and the resonance can occur at different wavelengths. The scattering spectra of individual silver nanoparticle of different shape is shown in Figure 1.5, which shows the resonance at different wavelengths[5] and helpful in designing the plasmonic structures at different wavelengths.

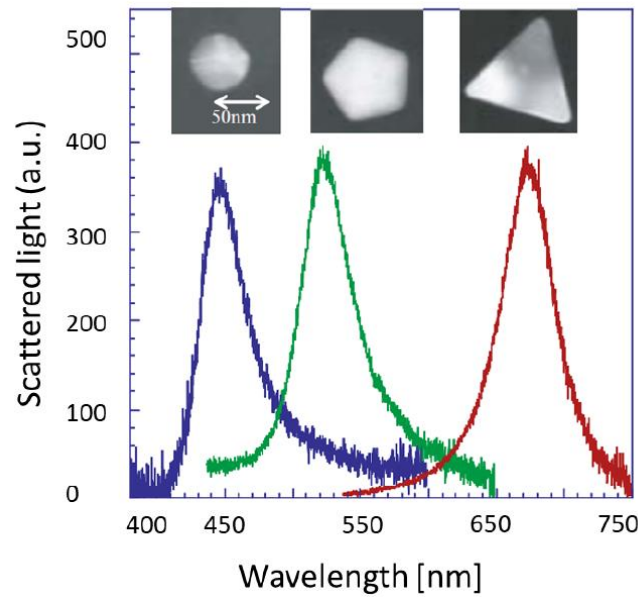


Figure 1.5 Scattering spectra of single silver nano particle of various shapes. Adopted from [5].

The field localization of LSP and the propagating SPP can be used in various applications including plasmonic waveguides [6], modulators [7][8], subwavelength hotspots in data storage [9], photodetection [10], lithography [11].

1.2 Two-Dimensional Materials

The pursuit of faster and better electronic devices has opened up several promising routes recently, including two-dimensional materials, quantum computing, topological computing, spintronics and valleytronics. Two dimensional-materials have extraordinary properties compared to its bulk. After the exfoliation of graphene in 2004 [12], the field of two-dimensional material has gained prominence. Graphene was exfoliated using an adhesion tape from bulk graphite. Graphene is a semi-metal, with high electron mobility [13], thermal conductivity [14], and mechanical strength [15]. There is no band gap in graphene, and the valence and conduction bands crossover at the Dirac point. The energy-momentum dispersion of graphene is linear around the Dirac point as shown in Figure 1.6.

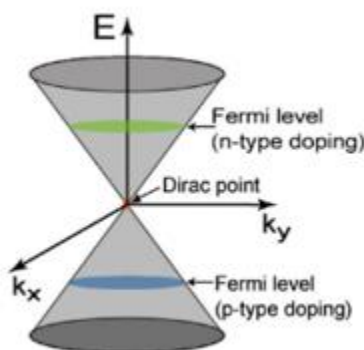


Figure 1.6 Band structure of Graphene. Adopted from [16].

Despite the extraordinary properties of graphene, the metallic nature (lack of bandgap) is limiting its use in switching devices [17] and could not be successfully used in transistors, a building block of modern computers. Hence there was a search for other two-dimensional layered semiconducting materials, which led to the discovery of many interesting compounds including transition-metal dichalcogenides, black phosphorus, oxides, halides, oxyhalides [18]. The layered

two-dimensional materials are covalently bonded within the plane and have van der Waals interactions between the layers (out of plane). Most of the 2D materials are tape exfoliated similar to graphene, limiting the wafer scale growth of these materials. Extensive research efforts are put in for the controlled large scale growth of these materials including chemical vapor deposition [19]. Black phosphorus is an emerging low-direct bandgap two-dimensional semiconductor, with unique properties (elucidated in detail in Chapter 2). It is promising for photo detection at infrared wavelengths due to its low band gap [20] and high mobility [21]. However, absorption in these 2D materials is low due to its ultra-thin nature. In this work, we design the plasmonic structures to enhance the photoresponsivity by localized surface plasmons.

1.3 Topological Insulators

Topological insulators are a new class of materials with bulk band gap and behaves as an insulator in its bulk but has protected conducting states on its surface or edge i.e., with a continuous set of energy states. The first topologically ordered states was found in 2D electron gas at very low temperature and strong magnetic field which underlies the quantum Hall effect [22]. Physicists have suggested that these edge states might be possible even in the absence of magnetic field in few materials, where strong-spin orbit coupling could play the role of magnetic field. This Quantum Spin Hall effect was experimentally realized in mercury telluride quantum wells in 2007 [23]. Subsequently, this lead to the new class of materials called topological insulators.

Topology is a branch of mathematics with spatial properties which are preserved under continuous deformation. For example, the invariant of closed surfaces. A closed surface with “n” holes can be smoothly modified (without cut and paste) into another closed shape with same “n” holes. A donut with single hole can be modified into coffee mug with a hole at the handle. And the number of holes is invariant during this process. Similar concept is extended to the electron bands, with an

invariant called Z_2 invariant [24]. If the overall Z_2 sum of all the occupied bands is even, then it is a regular insulator and if it is odd, it is a topological insulator. Hence the materials with band structure satisfying this Z_2 invariant and with spin-orbit coupling led to the discovery of topological insulators, with spin-momentum locking of surface states. The schematic of the band structure of a 3D topological insulator is shown in Figure 1.7. We see the bulk band gap between the valence and conduction bands and the gapless surface states. The dispersion of the surface state is linear, similar to graphene and they are spin polarized. Angle resolved photoemission spectroscopy has been used to study the band structure of topological insulators [22].

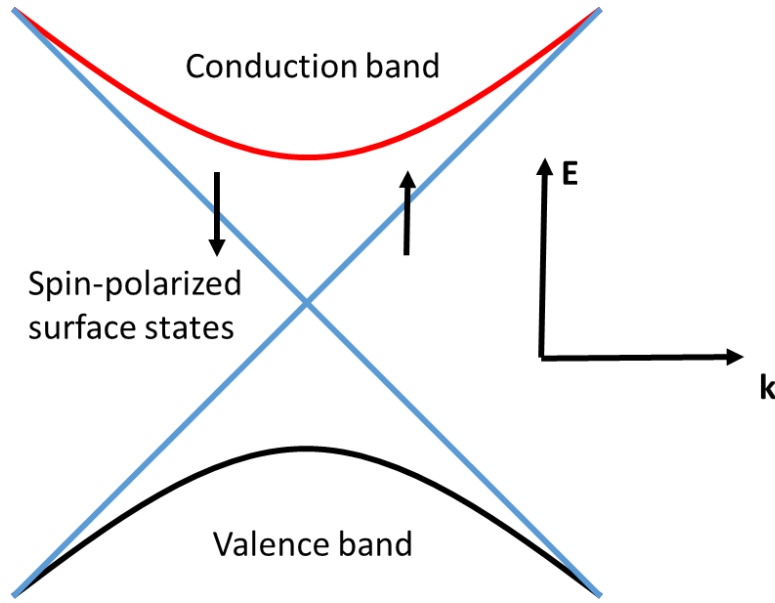


Figure 1.7 Schematic of the band structure of 3D topological insulator

Surface states of the topological insulators have unique properties including spin-momentum locking and are protected from backscattering which is of a great potential in the field of spintronics. The helicity dependent photocurrent is observed in the topological insulator Bi_2Se_3 [25], where light excites particular branch of surface states based on the helicity of light

and hence the helicity dependent photocurrent as spin and momentum are locked. These surface states are Dirac like, similar to graphene and can lead to exotic plasmonic phenomena.

$\text{Bi}_2\text{Te}_2\text{Se}$ is an emerging topological insulator with prominent surface state properties and better insulation of the bulk, as the Fermi level is situated near the middle of the band gap [26], [27]. In this work, we investigate the optical properties of $\text{Bi}_2\text{Te}_2\text{Se}$ and find that the bulk is plasmonic in UV-VIS wavelengths. We study the distinct propagating surface plasmons arising from its bulk and surface state, and are presented in Chapter 3.

1.4 Heat Assisted Magnetic recording

Heat assisted magnetic recording (HAMR) is one of the next generation technologies in data storage that can increase the areal density to beyond 1 Tb/in^2 [28]. There is always a need for increased storage capacity due to the increased amount of digital data. To meet this demand, the hard drive industry is pushing for higher areal density (bits per square inch) of hard drives [28]–[31]. With the current recording technology of perpendicular magnetic recording, areal density of 500Gb/in^2 is possible [32], [33]. Further scaling down the grain volume of storage medium is not feasible due to the superparamagnetic limit ($K_u V/k_b T > 70$; where K_u is the magnetic anisotropy, V is the volume of the grain, k_b is the Boltzmann constant, and T is the temperature) of the medium i.e., the magnetic state becomes thermally unstable [31]. It is possible to further decrease the grain volume and keep it thermally stable with the use of large magnetic anisotropy materials including FePt [29]. However, the coercivity of these large anisotropy materials is greater than the magnetic field that can be generated with the current hard drive head technology. HAMR is one of the possible technologies to address this issue. The schematic of HAMR write process is shown in Figure 1.8a, where the recording medium is heated beyond Curie point to reduce its coercivity

during recording, which enables writing with the available amount of magnetic field in the recording head.

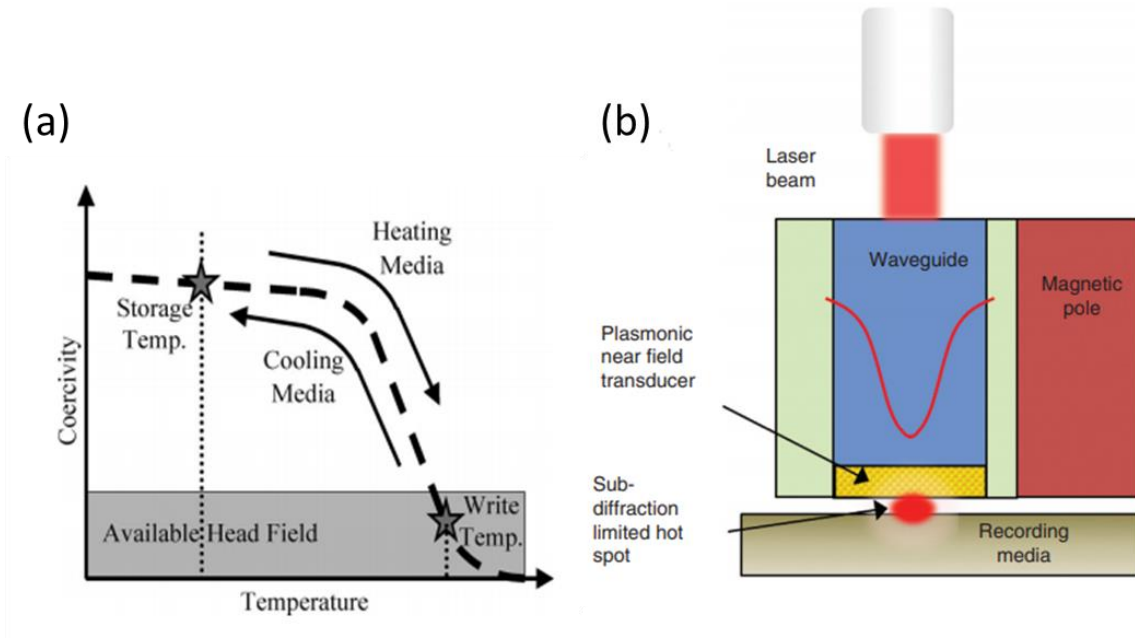


Figure 1.8 (a) Schematic of write process in HAMR. Adopted from [34]. b) Schematic of HAMR head. Adopted from [31].

The primary goal of HAMR is to heat the recording medium locally (few 10s of nm) which is much smaller compared to the diffraction limit of the light wavelength (800 nm) used in the HAMR system for heating the recording medium. The general schematic of HAMR head is shown in Figure 1.8b. Near-field transducer (NFT) is a key component of the HAMR system that locally heats the recording medium by concentrating light below the diffraction limit using surface plasmons. As shown in the schematic, light can be coupled to NFT using a waveguide. And the spacing between NFT and the recording medium is less than 5 nm, and the energy is coupled to the recording medium by near-field coupling. In this work, we perform an inverse design of NFT for a desired temperature profile in the recording medium and is presented in Chapter 4.

1.5 Outline of the Report

In this work, we study the surface plasmons and its applications in the emerging two-dimensional materials (black phosphorus and bismuth telluride selenide) and thin films. Chapter 2 discusses the two different plasmonic designs to enhance the photo responsivity of black phosphorus by localized surface plasmons. We use bowtie antenna and bowtie apertures to increase the absorption and polarization selectivity respectively. Plasmonic structures are designed by numerical electromagnetic simulations, and are fabricated to experimentally demonstrate the enhanced photo responsivity of black phosphorus. Chapter 3 discusses the distinct surface plasmons of the bulk and surface state of the topological insulator, $\text{Bi}_2\text{Te}_2\text{Se}$. The propagating surface plasmons are imaged using near-field scanning optical microscopy. The surface state plasmons are studied with a below band gap excitation of $10.6\text{ }\mu\text{m}$ wavelength. The surface state plasmon wavelength is 100 times shorter than the incident wavelength in sharp contrast to the plasmon wavelength of the bulk. Chapter 4 discusses the density-based topology optimization for inverse design of NFT for a desired temperature profile in the recording medium for HAMR. NFT designs for both generating a small heated spot size and a heated spot with desired aspect ratio in recording medium are demonstrated. Also, the effect of the waveguide, write pole and moving recording medium on the heated spot size is studied with the obtained NFT designs. Chapter 5 discusses the summary and future work including, ongoing efforts to explore the design of NFT for HAMR using machine learning.

2. PLASMONIC RESONANCE ENHANCED POLARIZATION SENSITIVE PHOTO DETECTION BY BLACK PHOSPHORUS

In this chapter, we use plasmonic structure to enhance the responsivity of black phosphorus photo detector. Bowtie antenna and bowtie apertures are used to increase the photocurrent and polarization selectivity respectively. Portions of this chapter have been published in [35], Venuthurumilli, P. K.; Ye, P. D.; Xu, X. “Plasmonic Resonance Enhanced Polarization-Sensitive Photodetection by Black Phosphorus in Near Infrared.” *ACS Nano* **2018**, *12*, 4861–4867.

2.1 Introduction

Two dimensional materials are of immense interest due to their extraordinary properties compared to their bulk counterparts. In addition to graphene [36][37] and transition metal dichalcogenides [38][39] such as MoS₂ [40][41], few-layer black phosphorus (BP) is intensively studied recently due to its unique properties including high mobility [21] and a thickness dependent direct band gap, ~ 0.3 eV in bulk and around 2 eV in monolayer [42][43][44][45], whereas MoS₂ has a direct band gap only as a monolayer [46][47]. Well behaved field effect transistors in BP have been demonstrated [48][49]. With these extraordinary properties, BP is a promising candidate for electronic and optoelectronic applications including scaled high-performance transistors [50], solar cells [51], and photodetectors [52][53].

Phosphorus has several allotropes and most common allotropes are white and red phosphorus which are widely used in explosives. BP can be obtained from white/red phosphorus at high pressure and temperature [54]. Low pressure synthesis of BP can be obtained using mineralizer as reaction promotor [55]. High quality BP can be obtained commercially from chemical manufactures including Sigma Aldrich and Smart elements.

BP has a puckered layer structure (Figure 2.1), resulting in anisotropic in-plane properties along its two principal armchair and zigzag directions. It has anisotropic thermal and electrical conductivity [21][56] and optical properties where the linearly polarized light in armchair direction has a greater absorption compared to that along the zigzag direction [57][58][59]. Inversion symmetry and mirror reflection symmetry of crystal structure in the zigzag direction forbid transitions of photons polarized in the zigzag direction with bandgap energy, and significantly reduce absorption of photons with higher energies [57].

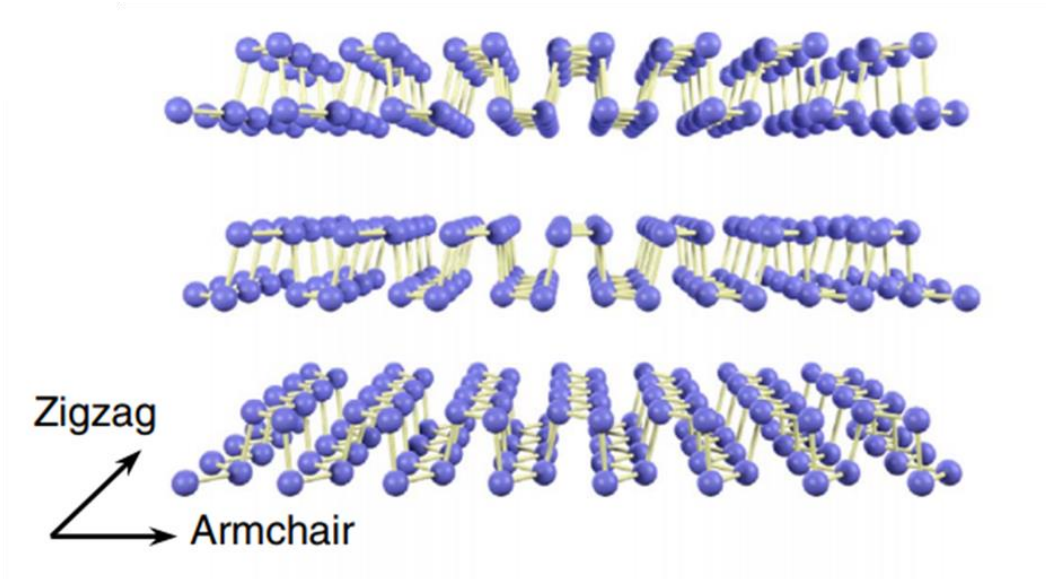


Figure 2.1 Lattice structure of BP. Adopted from [56]

The unique thickness dependent direct bandgap makes BP especially promising for photodetection, ~ 0.3 eV in bulk and around 2 eV in monolayer [60]. The comparison of the band gap of black phosphorus with other two dimensional and conventional semiconductors is shown in Figure 2.2. In this work we investigate methods to enhance photo response in black phosphorous photodetector at near IR wavelength which can find use in various applications including telecommunication, remote sensing. Conventional IR detectors require either expensive

fabrication process such as molecular beam epitaxy, low temperature operation, or both. Moreover, integration of these conventional narrow band gap semiconductors with traditional electronic materials such as silicon is difficult due to lattice mismatch [61]. In contrast, layered structure of black phosphorus is suitable for monolithic integration with silicon and even with flexible substrates [62].

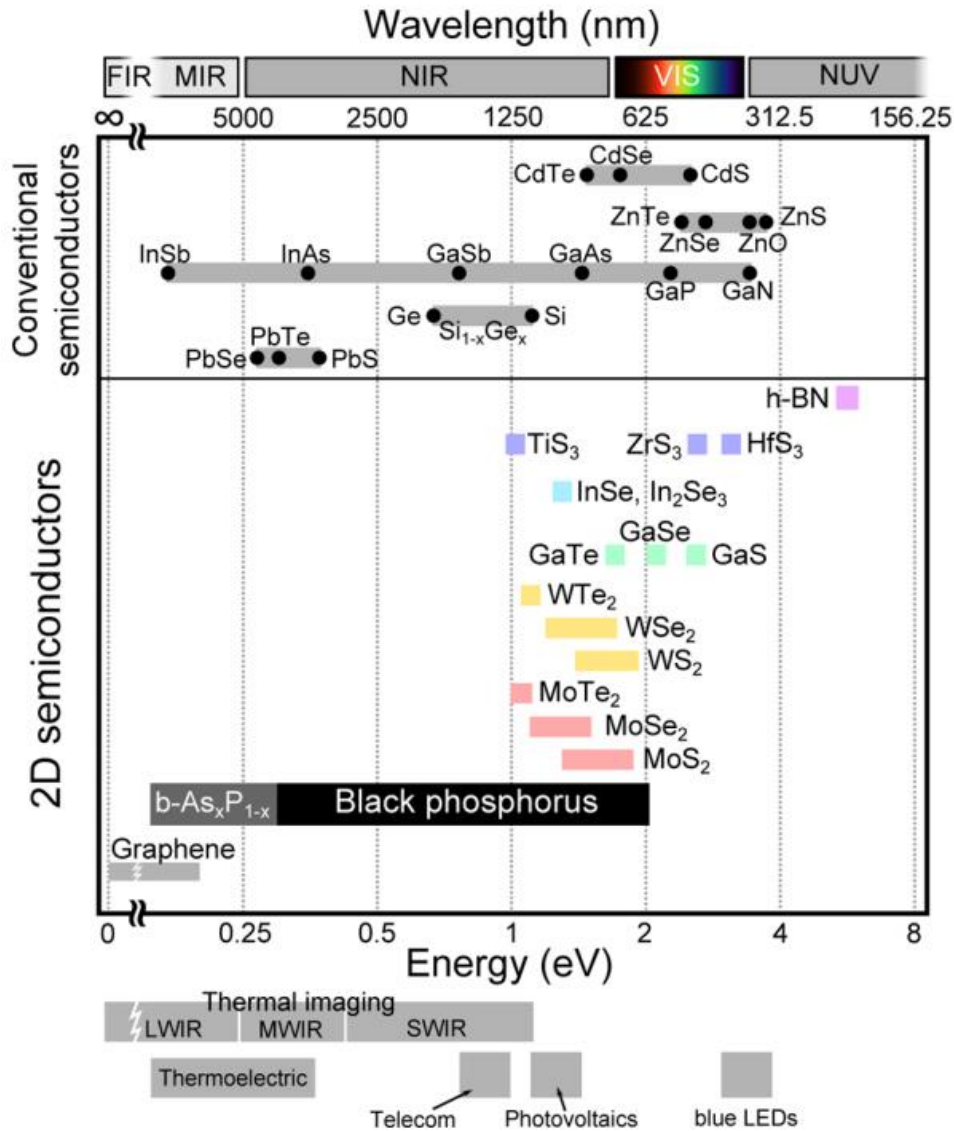


Figure 2.2 Comparison of bandgap of black phosphorus with other two dimensional and conventional semiconductors. Adopted from [60]

BP photodetectors have been reported [49][52][53][63][64][57]. However, the performance of most of these photodetectors is limited because of low light absorption in thin films. Several methods of enhancing absorption have been studied in thin films including multiple passing of light, trapping the light using Bragg reflectors, using photonic crystals and plasmonic structures [65]–[69]. Plasmonic structure enhanced photo responsivity in visible wavelengths has been demonstrated in graphene [70][71] and MoS₂ [72]. Here, we demonstrate enhanced photosensitivity and polarization selectivity in BP using plasmonic structures (localized surface plasmons) at the near IR wavelength of 1550 nm. The same methods can be used for longer wavelengths up to the band gap of BP, $\sim 4 \mu\text{m}$ [20]. We report two designs of plasmonic structures to enhance photosensitivity and polarization sensitive photodetection. We use bowtie antennas to enhance absorption and hence the photocurrent. Computational design shows that the enhanced absorption is due to field enhancement by bowtie plasmonic structures. In the other design, we use bowtie apertures (or bowtie aperture antennas) to enhance the inherent polarization selectivity of BP. The transmission of light through bowtie apertures is also polarization dependent [73], and hence can further enhance the polarization selectivity of BP. Here we experimentally demonstrate a bowtie aperture enhanced BP detector with a photocurrent ratio (armchair to zigzag) of 8.7, which is useful in IR polarimetry imaging [74].

2.2 Design of plasmonic structures

In this work, we design plasmonic structures made of gold for BP photodetector. Plasmonic structures are modelled using the finite element electromagnetic solver, ANSYS EM 17.1 with periodic boundary conditions. As discussed in Chapter1, the resonance of the localized surface plasmons depends on the optical constants. The frequency dependent optical constants for gold are taken from Johnson and Christy [75]. For BP, experimentally obtained in-plane optical constants

at 1550 nm of similar thickness were used for the armchair and zigzag directions for all wavelengths. Out of plane dielectric constants are considered as the average of armchair and zigzag directions.

Optical properties of the BP flakes at 1550 nm wavelength are determined by exfoliating flakes onto the glass substrate and by measuring reflectance (R) and transmittance (T) of the flakes. Reflectance of each sample is measured using a reference of silver coated mirror with a known reflectivity. Absorptivity (A) is calculated as $A = 1 - R - T$. Reflectance, transmittance and absorptivity of a 64 nm BP flake and a 145 nm BP flake along armchair and zigzag directions (characterized by the Raman spectroscopy, as shown later) are shown in Figure 2.3. We observe the anisotropic in-plane absorption with higher absorption along the armchair direction. The optical constants are then obtained from Fresnel equations using reflectance, transmittance and thickness of the film (characterized by the Atomic Force Microscopy) for both armchair and zigzag directions. The optical constants are, $n_{\text{armchair}} = 3.27$, $k_{\text{armchair}} = 0.33$ ($\epsilon_1 = 10.58$, $\epsilon_2 = 2.16$) and $n_{\text{zigzag}} = 3.22$, $k_{\text{zigzag}} = 0.13$ ($\epsilon_1 = 10.35$, $\epsilon_2 = 0.84$) for the 64 nm BP flake, and $n_{\text{armchair}} = 3.62$, $k_{\text{armchair}} = 0.33$ ($\epsilon_1 = 13$, $\epsilon_2 = 2.39$) and $n_{\text{zigzag}} = 4.14$, $k_{\text{zigzag}} = 0.03$ ($\epsilon_1 = 17.14$, $\epsilon_2 = 0.25$) for the 145 nm flake. The higher k value along armchair direction is because of higher absorption. Out-of-plane dielectric constants are considered the average of those of armchair and zigzag directions. In the design of bowtie antennas, the thickness of the flake is 135 nm and the optical constants obtained at 145 nm are used. In the design of bowtie aperture, the flake is 95 nm thick and the optical constants obtained at 64 nm are used.

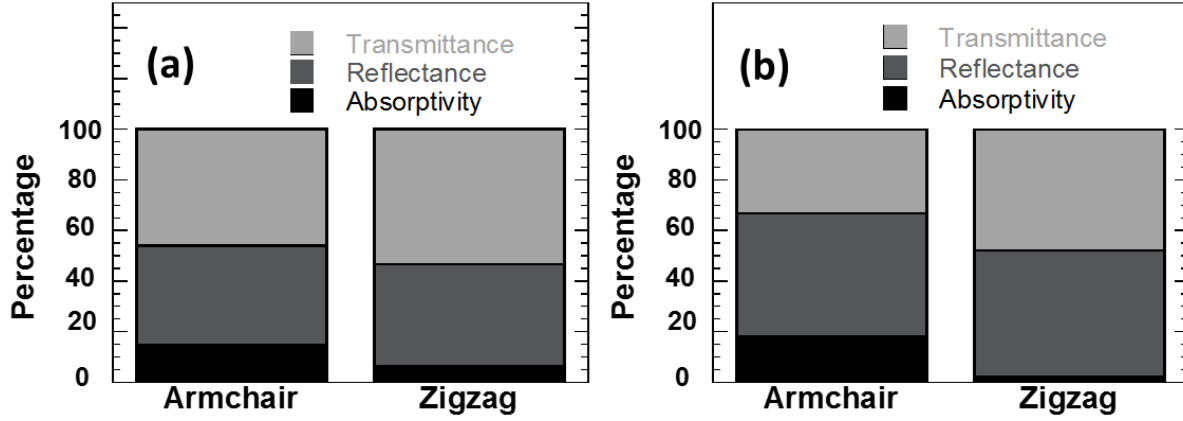


Figure 2.3 Optical property of BP: Optical transmittance T, reflectance R, and absorptivity A, of (a) 64 nm thick BP, (b) 145 nm thick BP, at 1550 nm wavelength along armchair and zigzag directions.

Bowtie antenna structures were optimized at the wavelength of 1550 nm for absorption along the armchair direction, along which inherent absorption of BP is higher. A schematic of the model is shown in Figure 2.4a. Substrate used in the simulations is SiO₂ (50 nm) on Si, and thickness of gold of plasmonic structures is 75 nm as in experiments. Light is illuminated from the air side (Figure 2.4a), the bowtie structures are aligned along the armchair direction (the x direction in Figure 2.4a) of BP, and the enhanced absorption of BP by bowtie structures along the armchair direction is shown in Figure 2.4b. The decreasing absorption in BP vs. wavelength for the case of without bowtie is because of thin film interference. The simulated electric field distributions with the fabricated bowtie structure dimensions (length = 524 nm, width = 563 nm, gap = 107 nm, period x = 758 nm and y = 790 nm) are shown in Figure 2.4c. From the field distributions in the XY plane at the exit of bowtie antenna and in the cross-section of the XZ plane, we see the enhancement of electric field in BP at the tip of bowtie antennas for illumination along armchair direction. This field enhancement in BP caused by bowtie structures led to the increase in absorption.

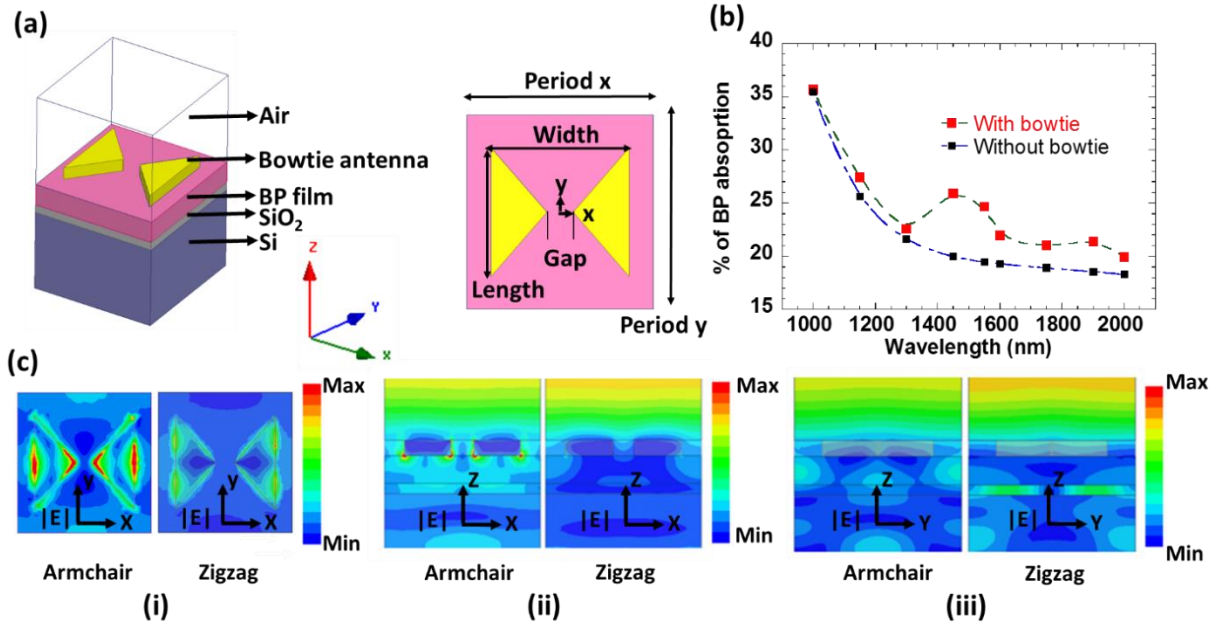


Figure 2.4 Simulated response of a BP device with bowtie antenna array. **(a)** Schematic of a unit cell of the simulation model. **(b)** Calculated absorption in BP, with and without bowtie structures when illuminated along the armchair direction. **(c)** Electric field distributions (i) top view of the XY plane at the exit of bowtie antenna, (ii) cross-sectional view of the XZ plane, and (iii) cross-sectional view of the YZ plane, for illuminations along the armchair and zigzag directions at 1550 nm wavelength.

The absorption in BP at 1550 nm wavelength with armchair polarization by varying the different dimensions of bowtie antenna is shown in Figure 2.5. Figure 2.5a and Figure 2.5b show the absorption by varying the length and period y respectively. Other dimensions are unchanged to the values mentioned earlier. It is found that by increasing the length the absorption increases and there is a resonance for period y of the bowtie antennas. Hence the resonance depends on the coupling with neighboring bowtie antennas.

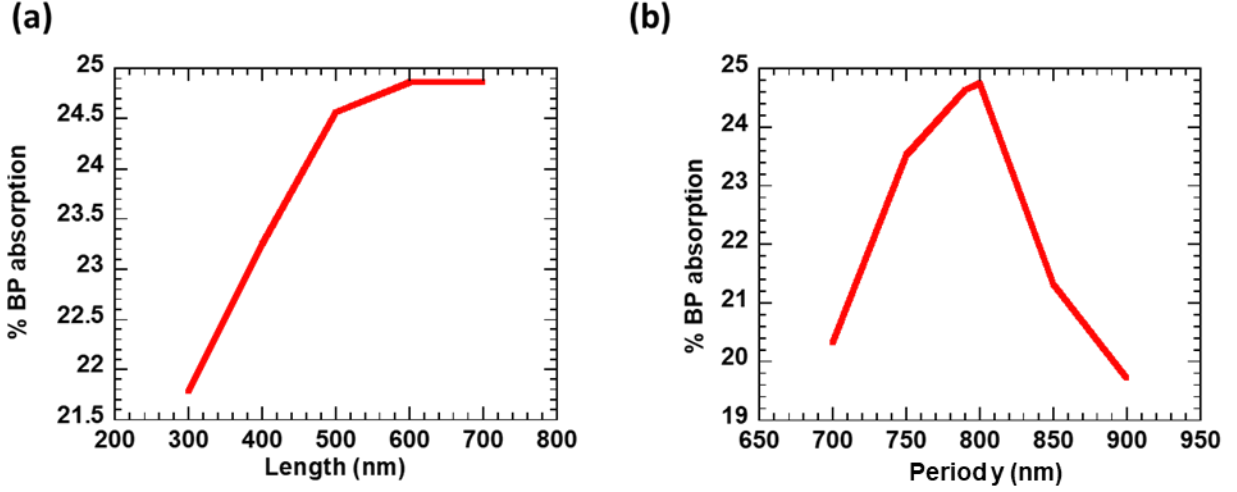


Figure 2.5 Absorption in BP by varying the different dimensions of bowtie antenna. (a) Length (b) Period y.

In the second design, we use an array of bowtie apertures to enhance the polarization selectivity of BP photo detection. A schematic of the simulation model is shown in Figure 2.6a. The plasmonic structures were designed such that the absorption ratio of armchair to zigzag is higher at wavelength of 1550 nm. The fabricated device geometry is used in the results shown in Figure 2.6, with length = 247 nm, width = 122 nm, gap = 35nm, period x = 349 nm, and period y = 259 nm. The gaps of bowtie aperture structures are aligned along the armchair direction (the y-direction in Figure 2.6a) of BP. Light is illuminated from the air side, and absorption vs. wavelength is shown in Figure 2.6b for polarizations along armchair and zigzag directions. At the resonance wavelengths (including 1550 nm), large absorption along the armchair direction results in higher polarization selectivity. From Figure 2.6b, we see that the absorption ratio of armchair to zigzag is expected to be high at the designed wavelength of 1550 nm. The electric field distributions across different planes, the XY plane at the exit of bowtie aperture and the cross-sectional YZ and XZ planes, for illuminations along the armchair and zigzag directions at

wavelength of 1550 nm are shown in Figure 2.6c. From the field distributions, we clearly see the enhancement of electric field only for the armchair polarization by bowtie apertures. High transmission only in the armchair direction leads to the high polarization ratio of absorption.

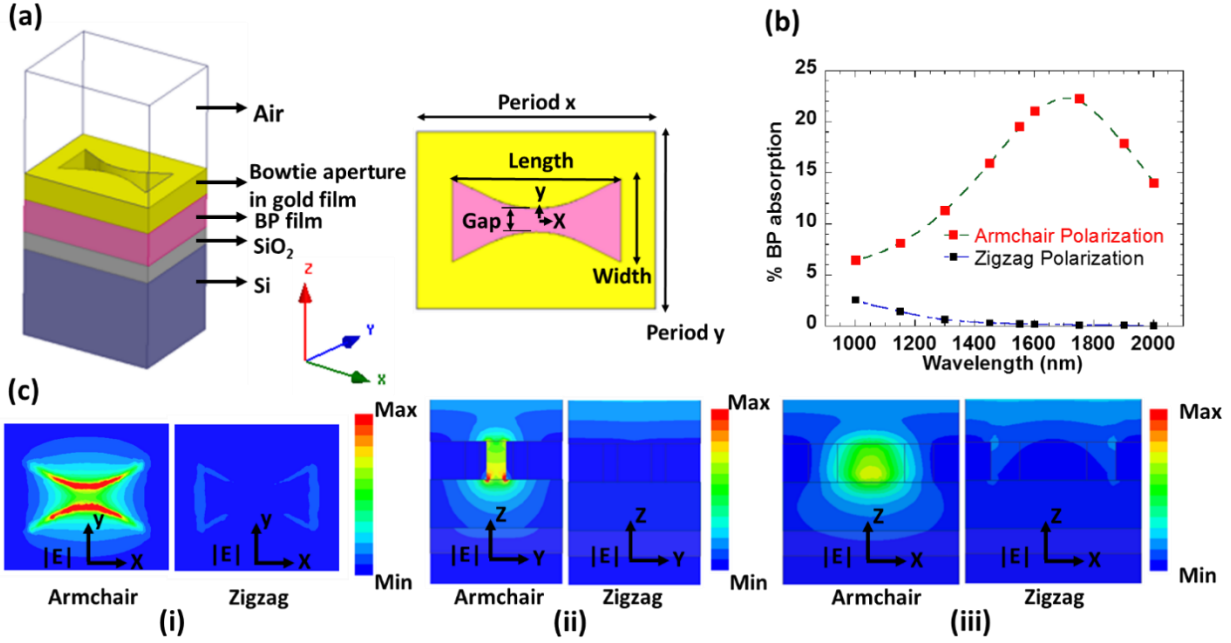


Figure 2.6 Simulated response of a BP device with array of bowtie apertures. (a) Schematic of a unit cell of the simulation model. (b) Calculated absorption in BP with the fabricated dimensions for two different polarizations, armchair (along the y-direction of figure 6a) and zigzag (along the x-direction of figure 6a). (c) Electric field distributions (i) top view of the XY plane at the exit of bowtie aperture, (ii) cross-sectional view of the YZ plane, and (iii) cross-sectional view of the XZ plane, for illuminations along the armchair and zigzag directions.

Bowtie apertures do not increase absorption for the armchair direction as compared to without bowtie apertures. Computations shows absorption in the armchair direction is 19% with bowtie apertures as compared to 21% without bowtie apertures. On other hand, the absorption in the zigzag direction has decreased from 10% to less than 1% with bowtie apertures.

The resonant wavelength of bowtie apertures can be controlled by the dimensions of the bowtie aperture. To illustrate this, absorption in BP vs. wavelength for different dimensions of bowtie aperture for armchair polarization is shown in Figure 2.7. Figure 2.7a and Figure 2.7b show the

absorption by varying the length and width of the bowtie aperture respectively. Other parameters are unchanged with dimensions' gap = 35nm, period x = 349nm and period y = 259 nm. We observe that the resonant wavelength increases with length of the bowtie aperture [76] and decreases with the width, which can be used to match the peak wavelength with the desired wavelength of device operation.

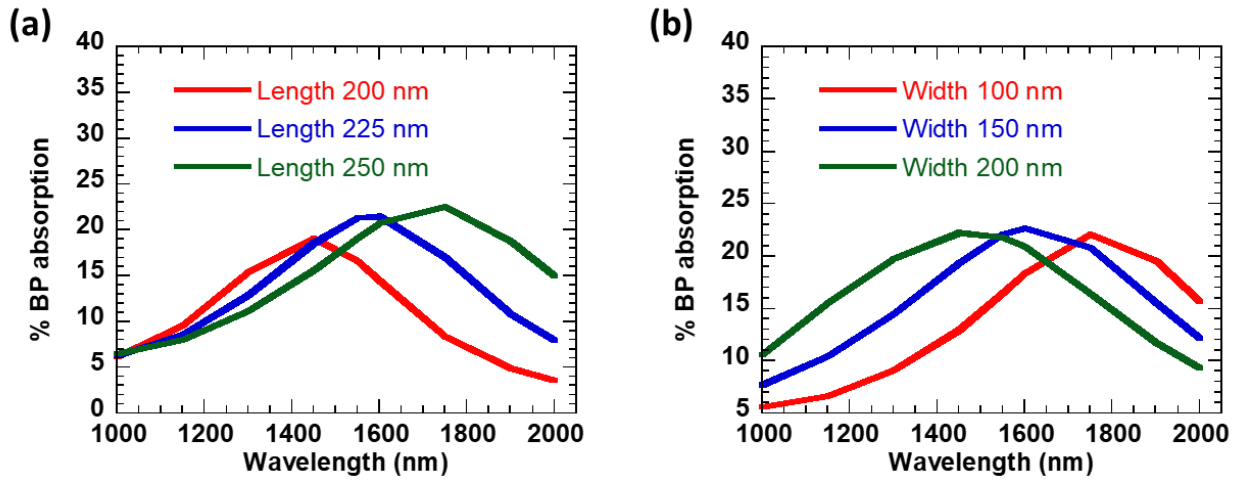


Figure 2.7 Percentage of absorption in BP vs. wavelength by varying the different dimensions of bowtie aperture. (a) length (b) width.

The resonant wavelength of plasmonic structures is sensitive to optical constants of BP. The absorption in BP vs. wavelength for the bowtie aperture design, for armchair polarization with two different optical constants of BP is shown in Figure 2.8a. The same geometry of bowtie apertures and 95 nm thick BP (thickness of the flake of the bowtie aperture design) is used. The in-plane optical constants experimentally obtained at 64 nm and 145 nm are used in the Figure 2.8a. As discussed earlier, the out-of-plane dielectric constants are taken as the average of the dielectric constant of the armchair and zigzag directions. The sensitivity of the out-of-plane dielectric constants (ϵ_1 and ϵ_2 are the real and imaginary part of dielectric constants) is shown in

Figure 2.8b for the bowtie aperture design with armchair polarization illumination. The variation of out-of-plane optical properties in the figure S8b are within the range of experimental in-plane properties of 64 nm and 145 nm flakes (for the 64 nm flake, $\epsilon_1 = 10.58$, $\epsilon_2 = 2.16$ for the armchair direction and $\epsilon_1 = 10.35$ and $\epsilon_2 = 0.84$ for the zigzag direction; for the 145 nm flake, $\epsilon_1 = 13$, $\epsilon_2 = 2.39$ for the armchair direction and $\epsilon_1 = 17.14$ and $\epsilon_2 = 0.25$ for the zigzag direction). We can see that the resonance wavelength is sensitive to the optical constants. The out-of-plane dielectric constant, $\epsilon_1 = 10.46$ and $\epsilon_2/\epsilon_1 = 0.143$ used in the simulations is also shown.

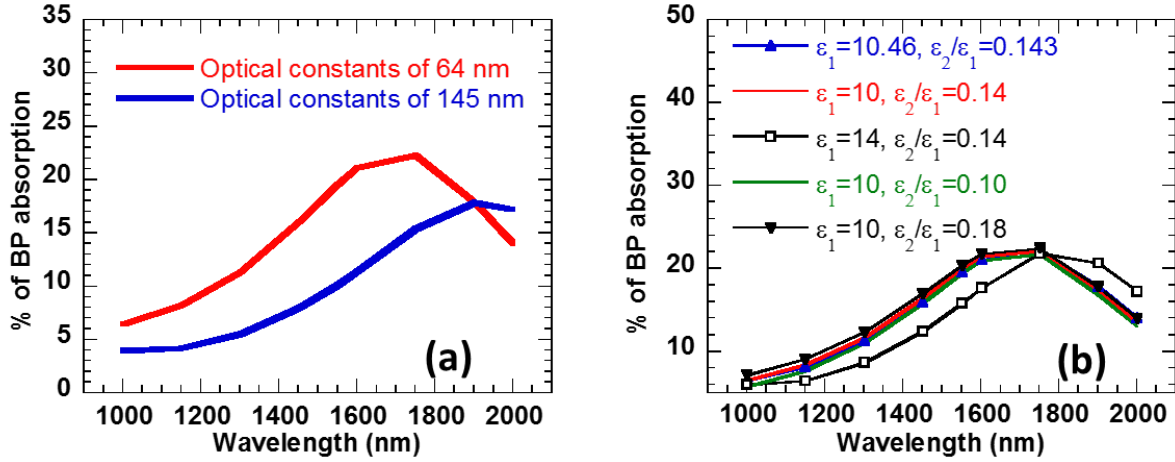


Figure 2.8 Calculated absorption in BP for the bowtie aperture design with armchair polarization, (a) Different in plane optical constants at 64nm and 145 nm. (b) Sensitivity of BP absorption vs. dielectric constant for the armchair polarization.

2.3 Fabrication of Plasmonic Devices

BP flakes are exfoliated from bulk using scotch tape onto SiO₂/Si substrate. The thickness of the oxide layer is 50 nm. BP flakes which are large and uniform are chosen from inspection under optical microscope. The thickness of the flakes is characterized using atomic force microscopy and the crystal direction of BP is determined by polarized Raman spectroscopy [56] using a HORIBA LabRAM HR800 Raman spectrometer.

The optimized plasmonic structures and metal contacts are fabricated onto the flakes on SiO₂/Si substrate using standard electron beam lithography, metallization, and liftoff processes. After the exfoliation, e-beam resist Poly methyl methacrylate, (PMMA A4 950) is spin coated onto the substrate at 2500 RPM for 60 seconds. Then the resist is baked at 180 °C for 90 seconds. The e-beam lithography is performed using Vistec VB6 system. After performing the dose test, dose of 1500 $\mu\text{C}/\text{cm}^2$ is used for Si substrate. Current of 1nA is used for the plasmonic structures and the current of 21 nA is used for writing the metal pads (contacts). After the lithography, sample is developed using Methyl isobutyl ketone/ Isopropyl alcohol, (MIBK/IPA 1:3) for 60 seconds and then in IPA for 20 seconds. After developing, Ti/Au (5/75nm) metal films are prepared using e-beam evaporation for both the plasmonic structures and metal contacts. After the metal deposition, liftoff is performed using acetone. Acetone gun/IPA is used for proper lift off of the bowtie apertures. Acetone gun gives more pressure for easy liftoff. Liftoff of bowtie structures without acetone gun is shown in Figure 2.9.

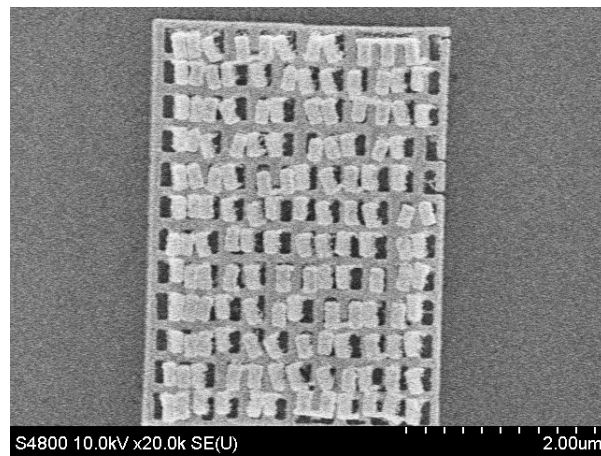


Figure 2.9 Liftoff of bowtie apertures on Silicon substrate (without acetone gun)

Liftoff using acetone gun without ultrasonic and with ultrasonic for 2 seconds (after using acetone gun) is shown Figure 2.10

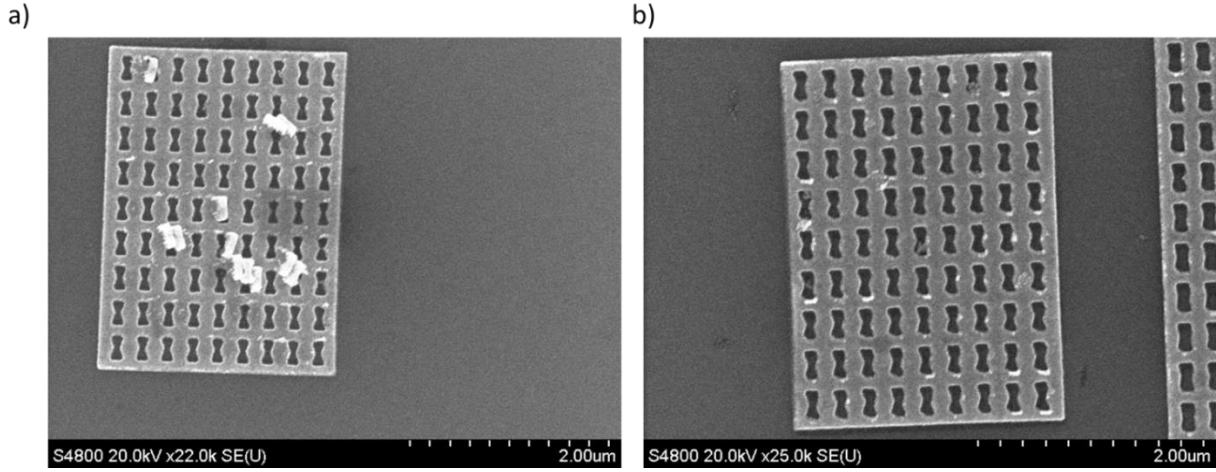


Figure 2.10 Lift off using acetone gun **(a)** Without ultrasonic **(b)** With ultrasonic for 2 seconds.

The optical image of fabricated bowtie antenna photodetector is shown in Figure 2.11. It has two devices on the same flake, (i) without plasmonic structures and (ii) with bowtie antenna plasmonic structures. Scanning Electron Microscopy (SEM) image of the bowtie structures of device (ii) in Figure 2.11a is shown in Figure 2.11b. The flake is 135 nm thick as characterized by Atomic Force Microscopy (AFM) and is shown in Figure 2.11c. Polarized Raman spectroscopy is used to determine the lattice orientation of BP. Figure 2.11d shows the Raman spectrum when the polarization is along the x-direction (Figure 2.11a), indicating that the x-direction is the armchair direction [56]. The device channel lengths are designed along the armchair direction for better photo carrier collection. This is because of shorter carrier transit time due to higher mobility along the armchair direction than that along the zigzag direction [53]. Bowtie structures are aligned by fabricating along the armchair direction as shown in Figure 2.11b to enhance armchair absorption by the localized surface plasmons.

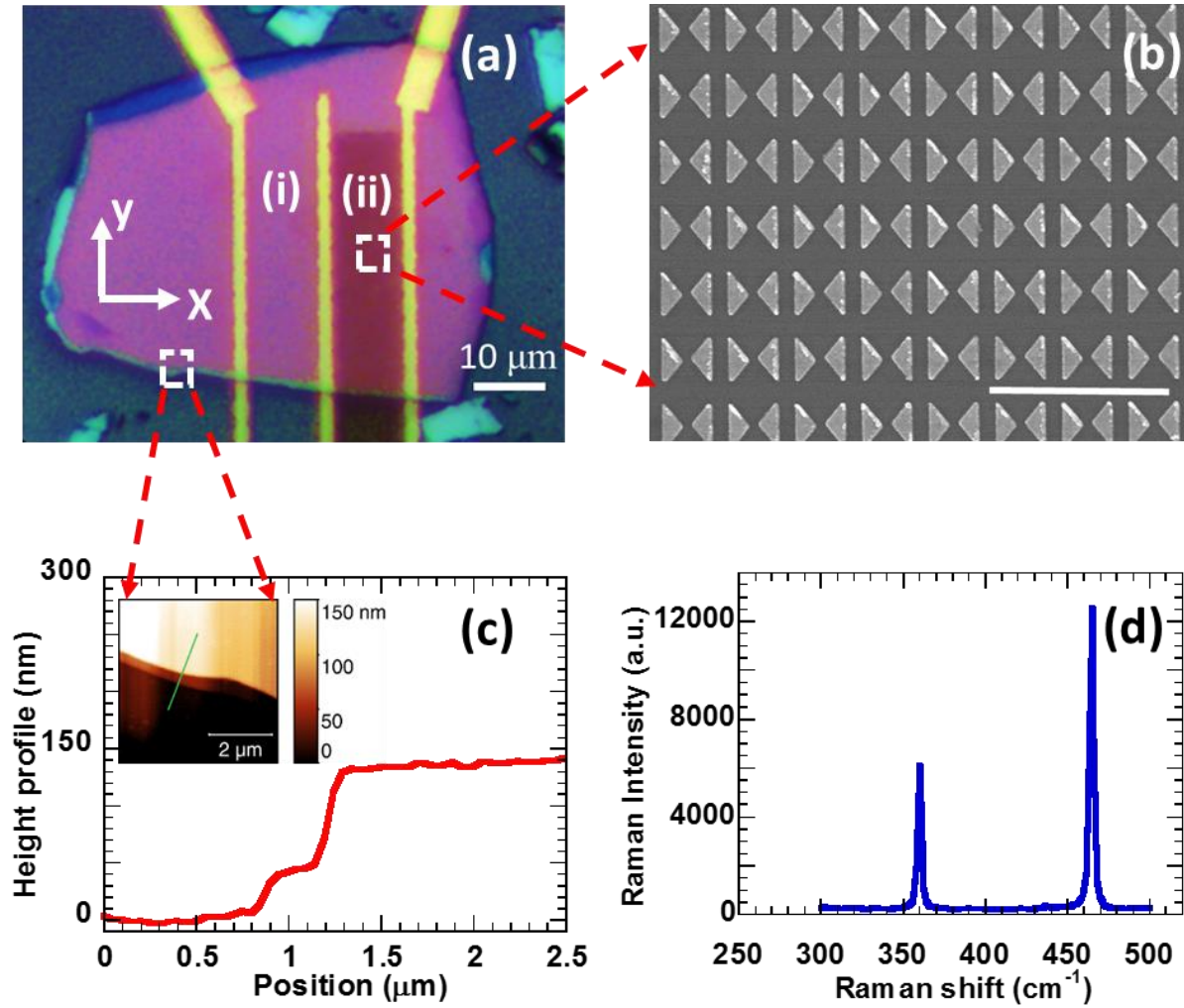


Figure 2.11 Bowtie antenna BP photodetector. **(a)** Optical image of two BP devices on one flake, (i) without plasmonic nanostructures and (ii) with array of bowtie antennas. **(b)** Scanning Electron Microscopy (SEM) image of array of bowtie antenna structures. Scale bar is 2 μm. **(c)** AFM height profile across the boundary of the BP flake (green line in the inset). Inset shows the AFM topography image of the BP flake. **(d)** Polarized Raman spectra for identifying the armchair direction in BP (the x – direction in Figure 2.11a).

The optical image of fabricated bowtie antenna photodetector is shown in Figure 2.12. In our design, the bowtie aperture gaps are aligned along the armchair direction to take advantage of the higher absorption along the armchair direction and hence the higher polarization ratio. Figure 2.12a shows an optical image of the device with the array of bowtie apertures and Figure 2.12b shows an SEM image of bowtie apertures. The armchair direction in this device is along the y

direction of Figure 2.12a, as determined by the polarized Raman spectroscopy. The flake is 95 nm thick as characterized by AFM and is shown in Figure 2.12c. The device channel length is again designed along the armchair direction because of higher mobility along the armchair direction, as was done for the previous design.

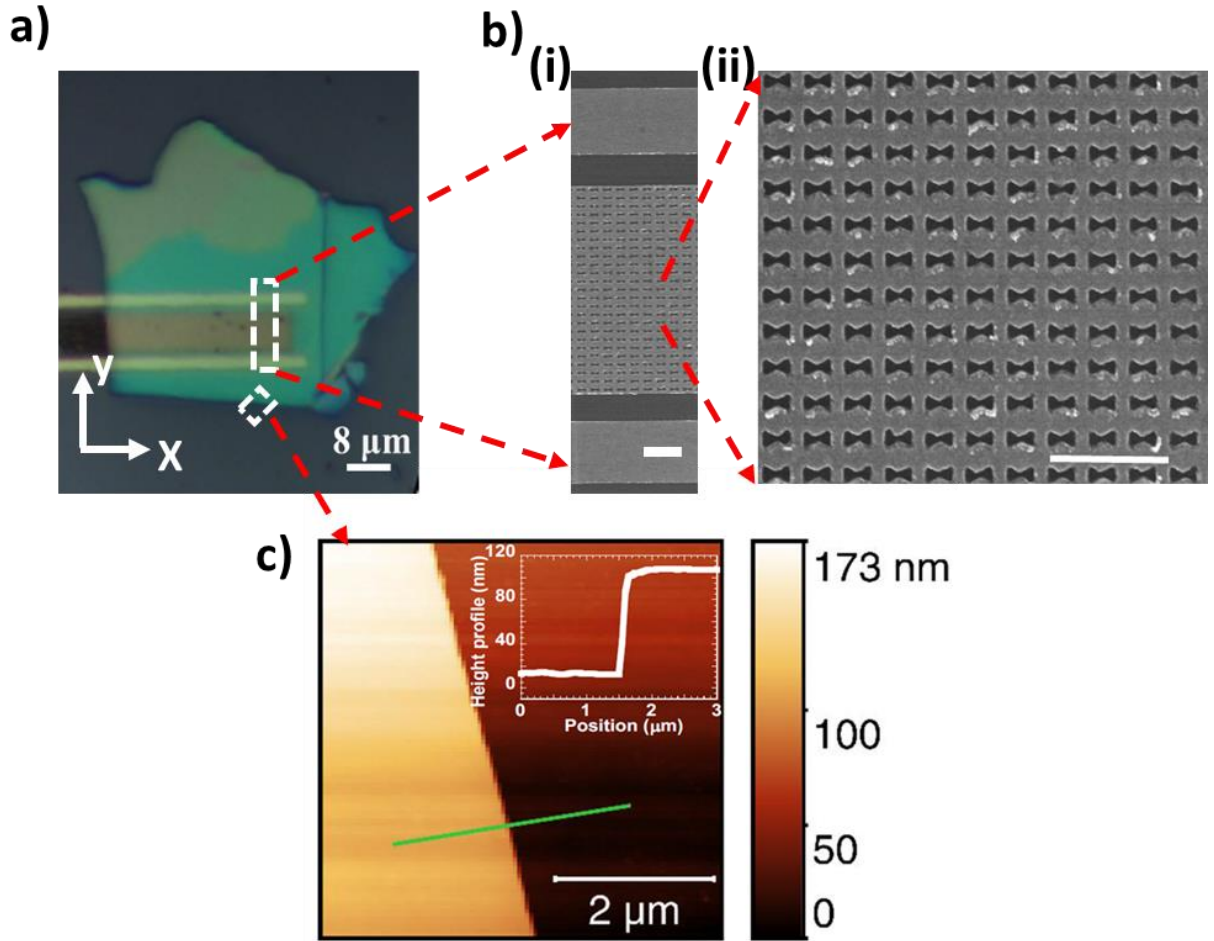


Figure 2.12 Bowtie aperture BP photodetector. **(a)** Optical image of the BP photodetector with the array of bowtie apertures. **(b)** (i) SEM image of array of bowtie apertures and contacts on the BP flake. Scale bar is 1 μm . (ii) Zoomed in image of the array of bowtie apertures. Scale bar is 1 μm . **(c)** AFM topography image of the BP flake. Inset shows the AFM height profile of the green line.

2.4 Experimental Results

The photo response of the devices is measured using a Keithley 2612 system and with a continuous wave laser of 1550 nm wavelength. The polarization of the laser is controlled by using a linear polarizer and half-wave plate. The laser is focused onto the sample using a 50x objective. Scanning photocurrent measurements are performed using a piezo stage (scanning the objective). The schematic of the bowtie antenna and bowtie aperture devices is shown in Figure 2.13. The two metal contacts, Source (S) and Drain (D) of the devices are connected to the Keithley using micro manipulators. One should ground properly while making the electrical contact to avoid burning of the devices due to static charge. By wearing the grounding wire strap, electrical connection to the contacts has to be done at zero bias voltage.

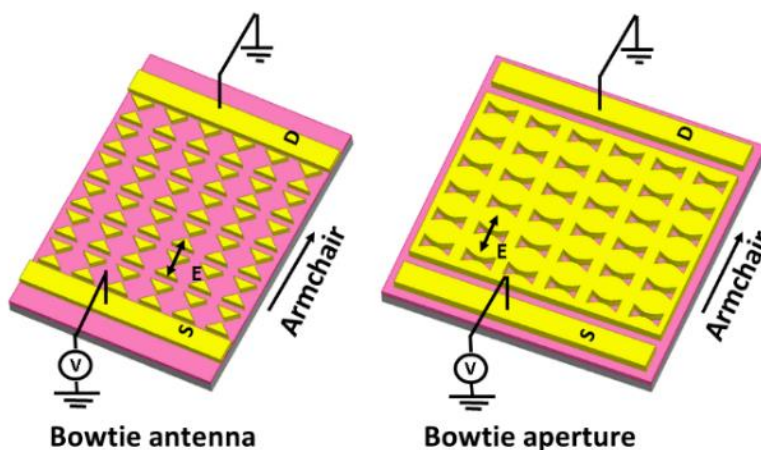


Figure 2.13 Schematic of the bowtie antenna and bowtie aperture photodetector

All optical and electrical measurements are performed in ambient atmosphere. The samples are stored in vacuum in between measurements to avoid BP degradation. The experimental set up is shown in Figure 2.14, showing the objective, objective scanner, laser input, sample and the micromanipulators.

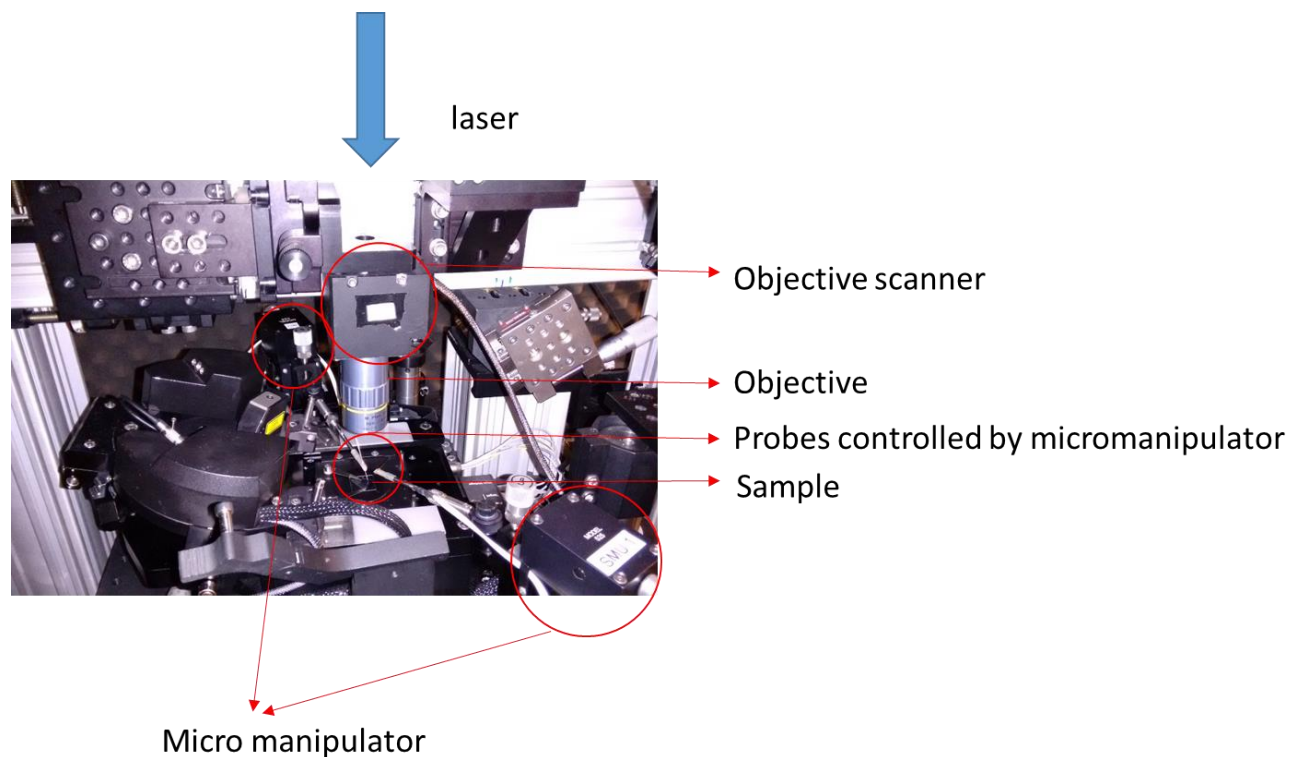


Figure 2.14 Experimental setup of photo detection

The experimental results of the bowtie antenna photodetector are presented first. The dark current (without incident light) I-V curves of both devices, with and without bowtie antennas of Figure 2.11 are shown in Figure 2.15 . The R^2 value for the linear fit of devices, with and without bowtie antennas is 98.9 and 97.8 respectively. Therefore, these devices are non-rectifying and small non-linearity could be due to the Schottky barrier.

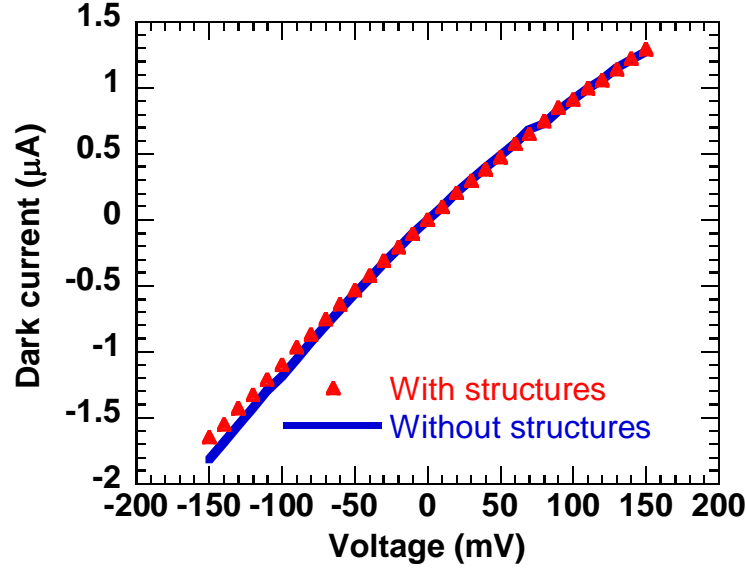


Figure 2.15 Dark current of the device with bowtie antennas and without bowtie antennas

To study photoresponse of the devices, scanning photocurrent measurements are first conducted on the devices with zero bias. The photocurrent map at zero bias and 470 μW incident power (at 1550 nm wavelength) of device with bowtie antennas is shown in Figure 2.16a. The laser spot size is about 4.7 μm . We see two current lobes of different sign at the two contacts. This is due to the photothermoelectric effect [77] and band bending at the contacts, which were observed in MoS_2 [78] and other BP devices [52]. Recent studies on graphene [79], carbon nanotubes [80][81], and MoS_2 [78] show that photothermoelectric effect may play an important role in photoresponse. To study the effect of the plasmonic structures alone, all the subsequent photocurrent measurements are performed at the zero current point of zero bias, which is located near the center of the devices, and results are shown in Figure 2.16(b-d). Under laser illumination, photocurrent (current under illumination minus dark current) vs. bias at a laser power of 1.05mW is shown in Figure 2.16b, for both devices and for polarizations along armchair and zigzag directions. We can see clearly that the photocurrent in the device with bowtie structures is much

larger than that in the device without structures because of enhanced absorption by plasmonic structures. Also, the photocurrent when illuminated along the armchair direction is larger than that along the zigzag direction due to higher absorption in BP and higher transmission through bowtie antennas. The photocurrent increases with bias because of extraction of more electron-hole pairs before they are recombined. The photocurrent vs. laser power at 150 mV bias is shown in Figure 2.16c for both devices and illumination polarizations. The photocurrent increases with laser power because of generation of more electron hole pairs. The photoresponsivity, defined as photocurrent divided by power of laser, at 150 mV bias is shown in Figure 2.16d. The photoresponsivity decreases with increasing laser power, which is a common behavior of photodetectors due to saturation of the electron-hole pair generation at high laser power and the increased surface recombination[82].

The experimental results on photocurrent are generally in agreement with simulation results of light absorption in BP. The absorption in both the polarizations is increased because of field enhancement by plasmonic structures. From the simulations, absorption in the armchair direction is increased from 19% in the device without structures to 25% in the device with structures (a 32% increase), while the absorption in the zigzag direction is increased from 2% in the device without structures to 4% in a device with structures (a 100% increase). We see from Figure 2.16b that the measured photocurrent increases with plasmonic structures for both polarizations, and the photocurrent when illuminated along the armchair direction is higher than that along the zigzag polarization. With a laser power of 1.05 mW and 150 mV bias, the photocurrent enhancement is about 31% along the armchair direction and 50% along the zigzag direction. At a lower laser power of 130 μ W (and the same 150 mV bias), the photocurrent enhancement is about 70% along the armchair direction and 37% along the zigzag direction. We

cannot draw a quantitative comparison between the simulated electric field distributions and the experimental photocurrent measurements. The photocurrent depends on extraction of electron hole pairs and is affected by electron hole recombination, while the simulations only show the absorbed electric field.

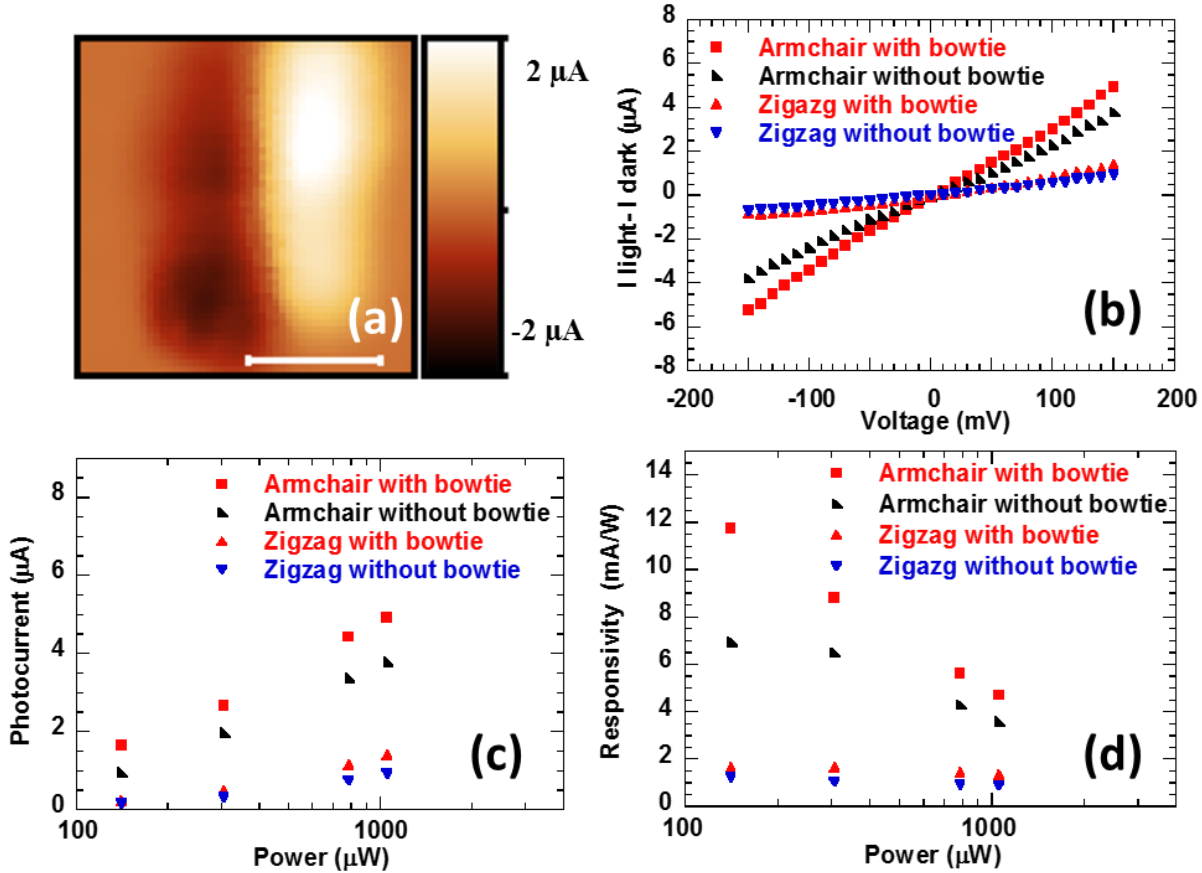


Figure 2.16 Response of bowtie antenna BP photodetector at 1550 nm wavelength (a) Photocurrent map of device with plasmonic structures at zero bias, with 470 μW incident laser power. Scale bar is 20 μm . (b) Illumination current minus dark current ($I_{\text{light}} - I_{\text{dark}}$) vs. bias voltage at 1.05mW of laser power for both devices, with and without bowtie antennas, and both polarizations along armchair and zigzag directions. (c) Photocurrent vs. laser power at 150 mV bias. (d) Photoresponsivity vs. laser power at 150 mV bias.

Scanning photocurrent maps of devices, with and without bowtie antennas are shown in Figure 2.17 a-e, with 470 μW incident power at 1550nm wavelength. Figure 2.17a shows the photocurrent map at zero bias with zigzag polarization for device with bowtie antennas. Figure

2.17b, c show the photocurrent map at 100 mV bias with zigzag polarization for devices with and without bowtie antennas, respectively and Figure 2.17d, e show the map at 100 mV bias with armchair polarization for devices with and without bowtie antennas, respectively. The maximum photocurrent occurs near the electrodes. From the photocurrent maps, we observe that the maximum photocurrent at 100 mV with bowtie antennas is larger than the device without bowtie antennas for both illumination polarizations. The maximum photocurrent for the device with plasmonic structures is ~ 2.2 times the photocurrent at the center of the device (zero current point at zero bias) for armchair polarization. The photocurrent map with 633 nm wavelength (spot size is about $2\ \mu\text{m}$) at zero bias and $200\ \mu\text{W}$ incident power for the device with bowtie antennas, with armchair polarization is shown in Figure 2.17f. We clearly can see that the two lobes are near the contacts with the smaller laser spot size.

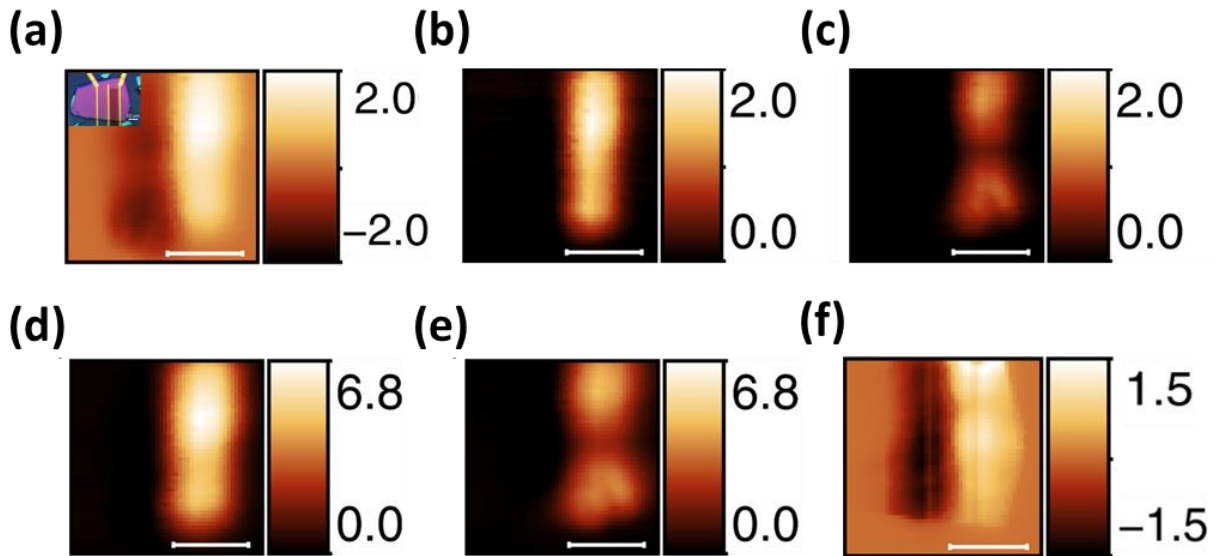


Figure 2.17 Scanning photocurrent measurements **(a-e)** Photocurrent maps with $470\ \mu\text{W}$ incident power at 1550 nm wavelength. **(a)** With bowtie antennas at zero bias, zigzag polarization. **(b)** With bowtie antennas at 100 mV bias, zigzag polarization. **(c)** Without bowtie antennas at 100 mV bias, zigzag polarization. **(d)** With bowtie antennas at 100 mV bias, armchair polarization. **(e)** Without bowtie antennas at 100 mV bias, armchair polarization. **(f)** Photocurrent map with $200\ \mu\text{W}$ incident power at 633 nm wavelength in the device with bowtie antennas, at zero bias and with armchair polarization. All Scale bars: $20\ \mu\text{m}$ and color bars in μA .

The maximum photo responsivity for the armchair polarization with plasmonic structures is 14.2 mA/W at a laser power of 470 μ W and 100 mV bias, and has an increase of 43% and 61% for armchair and zigzag polarizations respectively compared with those without plasmonic structures. As a comparison, the responsivity at wavelength of 1550 nm by previous studies are 0.3 mA/W (at the same bias of 100 mV) [57] and 3 mA/W (at our incident power for measurements performed up to 200 mV bias) [52]. Therefore, the responsivity of our plasmonic enhanced BP photodetector is more than four times greater than the previously reported values. In addition to enhanced absorption in BP by plasmonic structures, there is a built-in field at the interface of BP and Ti/Au structures caused by the work function difference, which separates the photoinduced carriers generated in BP. The electrons will be swept from the surface of BP into the metal, while there is a small barrier for holes as seen from the band diagram[49]. This can lead to longer recombination time and can cause more photocurrent, as was observed in graphene[83][84]. Also, very limited photocurrent was reported by hot electrons from gold plasmonic structures injected into silicon over the Schottky barrier[85]. In our experiments, we are unable to distinguish the contribution between the hot electrons from metal and photo-induced carriers in BP as our incident energy is greater than the band gap of BP. However, we expect the hot electron contribution to be weak as there is no barrier for electrons to return to the gold by the built-in field at the interface. We performed the transient current measurements by mechanically modulating the incident light (using a chopper). The transient response of our devices, with and without bowtie antennas, and for polarizations along armchair and zigzag directions are measured using a low noise current preamplifier SR 570. The data at two different modulating frequencies of 400 and 800 Hz, for the device with bowtie structures at 100 mV bias, with light polarization along the armchair direction

is shown in Figure 2.18. We observe that the rise time decreases with modulating frequency and hence the measurement was limited by the speed of the mechanical chopper. From our measurements, the response time of the devices, with and without bowtie structures for light polarization along armchair and zigzag directions are all less than 90 μs . The reported intrinsic response time of the black phosphorus photodetector can be as fast as ~ 75 ps along both armchair and zigzag directions [86]. Since we expect the hot electron contribution to be weak, the response time of devices with and without plasmonic structures would be similar as observed in graphene [83].

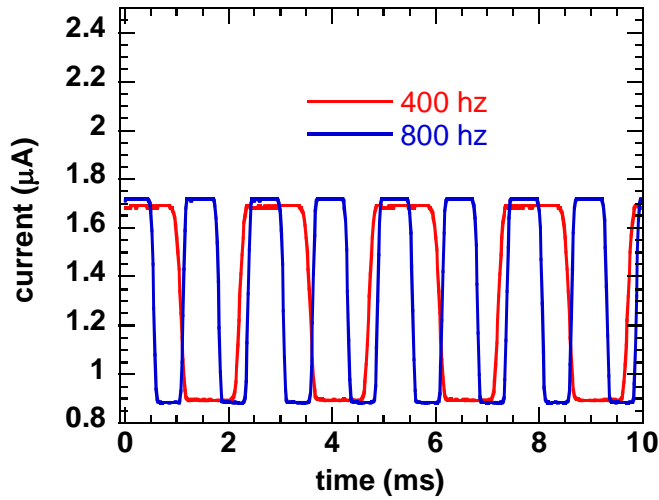


Figure 2.18 Transient current measurement of device with bowtie structures at 100mV bias, for armchair polarization at different modulating frequencies.

In the second design, we use an array of bowtie apertures to enhance the polarization selectivity of BP photo detection. Just to compare, the first design of bowtie antennas is intended to enhance the photocurrent; however, the polarization ratio (defined as the ratio of photocurrent in the armchair direction to that in zigzag direction) is not increased much. The polarization ratio vs power of devices with and without bowtie antennas at 150 mV bias is shown in Figure 2.19.

The polarization ratio decreased at high powers and increased at low power with bowtie antennas, hence there is no trend of polarization ratio for the first design.

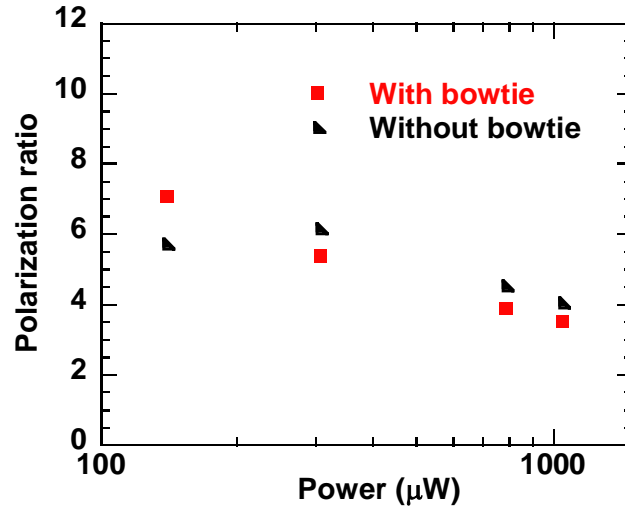


Figure 2.19 Polarization ratio vs. power for both devices, with and without bowtie antennas at 150 mV bias.

The transmission of light through bowtie apertures depends on the incident polarization, and the transmission along the direction of the gap of bowtie aperture is higher [73]. Hence, the second design of bowtie apertures enhances the absorption ratio by suppressing transmission for polarization along the zigzag direction as there is no BP exposed to light other than that through the apertures. In our design, the bowtie aperture gaps are aligned along the armchair direction to take advantage of the higher absorption along the armchair direction. All photocurrent measurements of the bowtie aperture photodetector are conducted at the zero current point at 0 V bias and the results are shown in Figure 2.20. I-V curves of dark current (without incident light) and with laser power of 580 μW along armchair and zigzag polarizations are shown in Figure 2.20a. Photocurrent and photoresponsivity vs. laser power at 150 mV bias are shown in Figure 2.20b and Figure 2.20c, respectively, for both polarizations. Same as the previous design, the

photocurrent increases with laser power, and photoresponsivity decreases with laser power due to the reasons discussed previously. The polarization ratio is shown in Figure 2.20d, as a function of laser power at 150 mV bias for devices with and without bowtie apertures. We see that the polarization ratio in the device with bowtie apertures increased from 4 to 5.8 (at a laser power of 1.05 mW) compared to that without bowtie apertures.

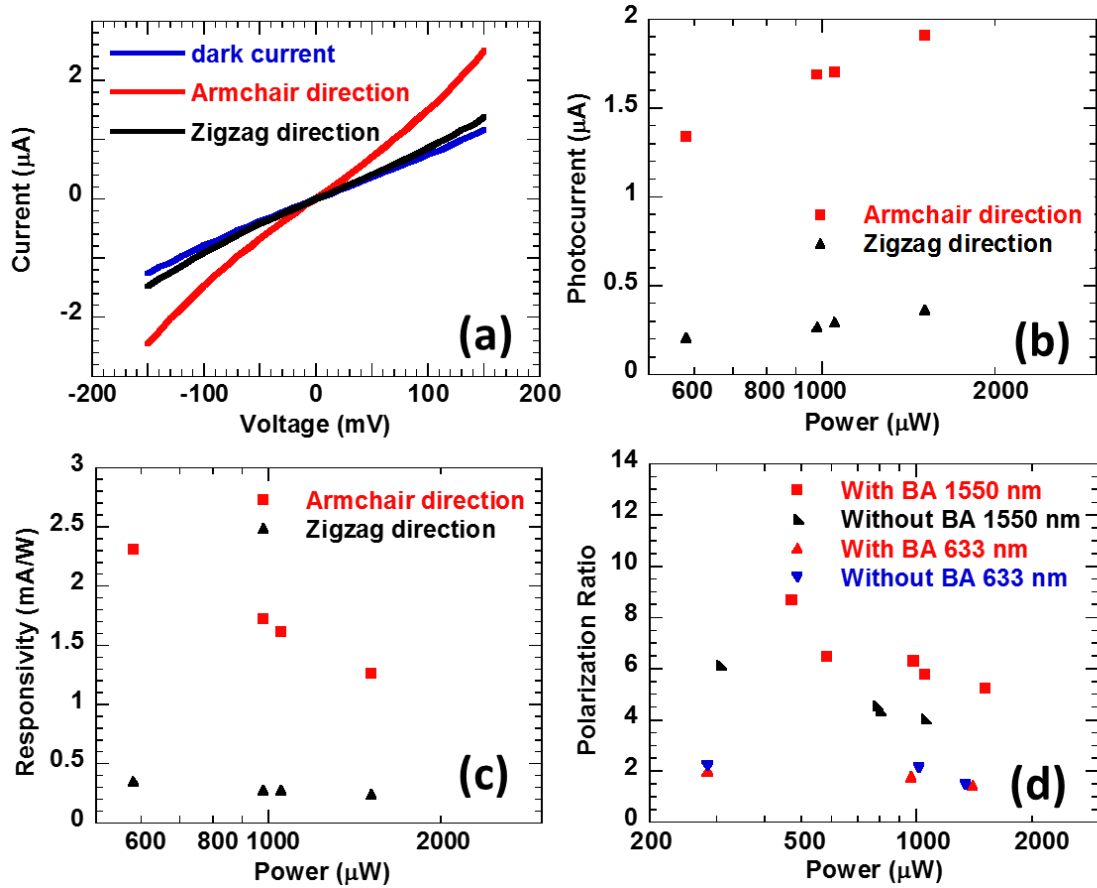


Figure 2.20 Response of the bowtie aperture photodetector. **(a)** Dark current and illumination current at 580 μW vs. voltage for different polarizations at 1550 nm. **(b)** Photocurrent vs. power at 150 mV bias for different polarizations at 1550 nm. **(c)** Responsivity vs. power at 150 mV bias for different polarizations at 1550 nm. **(d)** Comparing polarization ratio vs. laser power at 150 mV bias, with and without bowtie apertures (BA) and at wavelengths of 1550 nm and 633 nm.

The polarization ratio decreases with laser power for both with and without bowtie apertures. The possible reason for the decrease in polarization ratio with increase in laser power is

the saturation of increased photocurrent extraction in the armchair direction as the photo absorption increases. Also shown in Figure 2.20d is the measurement using 633 nm wavelength. It is seen that the polarization ratio at 633 nm does not change much, as the response of the bowtie aperture strongly depends on the wavelength due to its plasmonic resonance. At a lower laser power of 470 μW , a higher polarization ratio of 8.7 is obtained in the bowtie aperture BP photodetector at the design wavelength of 1550 nm. I-V curves of dark current (without incident light) and with laser power of 470 μW along armchair and zigzag polarizations are shown in Figure 2.21. The current for polarization along the zigzag direction is only slightly larger than the dark current.

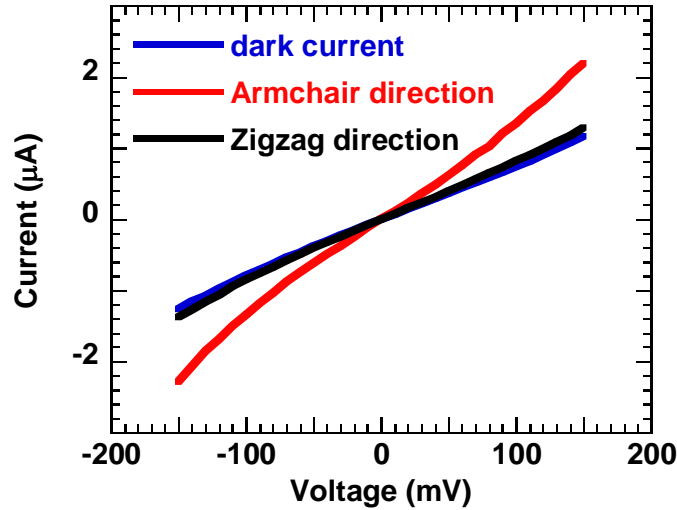


Figure 2.21 Dark current and illumination current at 470 μW vs. voltage for different polarizations of a bowtie aperture photodetector.

It was reported that patterned Au nano structures can locally influence the graphene Fermi energy [87][88]. We do not expect Au patterns to strongly influence the transport properties in our devices of bulk BP. In our first device, although, 20 % of BP is covered by metal, the dark currents of both devices (with and without bowties) are similar as shown in Figure 2.15. For the second design, resistivity of the device with bowtie apertures is estimated to be 4.71 ohm-cm, while the

resistivity of the device without plasmonic structures shown in Figure 2.11 is 5.28 ohm-cm. The 10% variation in resistivity could be because of device to device variation as well as a minor surface effect by gold.

The enhancement of absorption ratio at the designed wavelength of 1550 nm from simulation is larger than that obtained experimental enhancement of polarization ratio. The deviation can be due to factors including, high sensitivity of resonance with dielectric constants (as shown in Figure 2.8) and imperfections of the fabricated geometry of plasmonic structures (*e.g.*, variations in the sizes of fabricated bowtie apertures). In addition, we cannot draw a direct quantitative comparison between the simulated field distributions and the experimental photocurrent measurements due to the reasons discussed previously. As is seen in Figure 2.21, at a lower laser power of 470 μW , the measured photocurrent along the zigzag direction is only slightly larger than the dark current. This indicates that bowtie apertures do suppress transmission effectively at low laser powers. Hence, it is anticipated that higher polarization selectivity can be realized when the incident power is low, such as in imaging.

2.5 Summary

In summary, we demonstrated enhanced photosensitivity and polarization selectivity of black phosphorus photodetectors using resonant plasmonic structures. In the first design using bowtie antennas, we obtained an enhancement of 70% in the photo response in comparison to a device without plasmonic structures. The responsivity of the bowtie antenna BP photodetector, even at lower bias, is more than four times greater than previously reported values. Simulation shows that absorption is increased due to the field enhancement by the plasmonic structures. In the second design using bowtie apertures, photocurrent can be effectively suppressed for zigzag polarization, particularly when the incident power is low such as in imaging. An armchair to zigzag

polarization ratio of 8.7 has been demonstrated. Enhanced photosensitivity and polarization selectivity at near infrared wavelengths will be useful in various applications including telecommunication, remote sensing, and infrared polarimetry imaging.

3. NEAR-FIELD IMAGING OF SURFACE PLASMONS FROM THE BULK AND SURFACE STATE OF THE TOPOLOGICAL INSULATOR BISMUTH TELLURIDE SELENIDE

In this chapter, the distinct surface plasmons of the bulk and surface state of the topological insulator, $\text{Bi}_2\text{Te}_2\text{Se}$ are discussed. The propagating surface plasmons are imaged using near-field scanning optical microscopy. The surface state plasmon wavelength is found to be 100 times shorter than the incident wavelength in sharp contrast to the plasmon wavelength of the bulk. Portions of this chapter have been published in [89], Venuthurumilli, P. K.; Wen, X.; Iyer, V.; Chen, Y. P.; Xu, X. “Near-Field Imaging of Surface Plasmons from the Bulk and Surface State of Topological Insulator $\text{Bi}_2\text{Te}_2\text{Se}$.” *ACS Photonics* **2019**, 6, 2492–2498.

3.1 Introduction

Plasmons can localize the electromagnetic energy to nanoscale, well below the wavelength of light in free space. Plasmonics has emerged as a promising area in various fields such as waveguides [90], [91], biological sensing [92]–[94], photovoltaics [95] and photodetection [35], [70]. However, materials that can support surface plasmons are limited, most notably noble metals such as gold and silver. However, noble metals which are commonly used in plasmonic devices are not CMOS compatible, limiting the scaling of these devices. Hence there is a search for plasmonic materials beyond noble metals. The materials that are currently being investigated include highly doped semiconductors, transparent conducting oxides, metallic alloys [96] and more recently graphene [97], [98] and topological insulators [99].

Topological insulator is a family of materials with insulating bulk but has conducting electronic surface states (SS). These SS are Dirac-like and protected from backscattering [100], [101] which can lead to exotic plasmonic phenomena. Recent works on the studies of topological

insulators include plasmonic resonance of Bi_2Se_3 gratings at THz frequencies [102] and $\text{Bi}_{1.5}\text{Sb}_{0.5}\text{Te}_{1.8}\text{Se}_{1.2}$ (BSTS) nanostructures at ultraviolet and visible frequencies [99]. In addition to these spectroscopic studies of nanostructures, real space imaging of localized plasmons was carried out using TEM-EELS on Bi_2Te_3 nanoplates [103] and near-field scanning optical microscopy (NSOM) on BSTS flakes [104] and Bi_2Te_3 flakes [105]. Among the topological insulators, $\text{Bi}_2\text{Te}_2\text{Se}$ (BTS) has been shown to have prominent SS properties and better insulation of the bulk, as its Fermi level is situated near the middle of the band gap [26], [27]. In this work, we study the distinct surface plasmons arising from the bulk and SS of BTS.

BTS has a rhombohedral lattice with hexagonally close packed of five atoms (quintuple layer) along the c-axis [106]. The basic quintuple-layer unit is Te-Bi-Se-Bi-Te. The lattice structure of BTS is shown in Figure 3.1. The schematic of the band structure of BTS is shown in Figure 3.2, we can see the bulk valence band (BVB) and the bulk conduction band (BCB) and the Dirac surface states. The Dirac point is closer to the valence band. Also shown is the Fermi level, situated near the middle of the band gap.

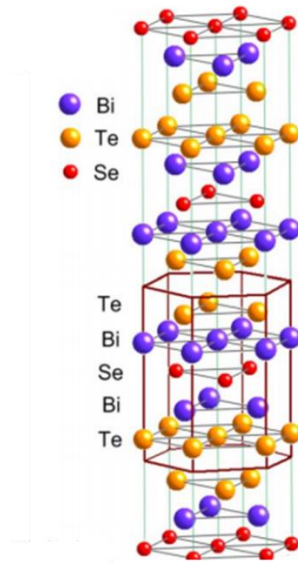


Figure 3.1 Lattice structure of BTS. Adopted from [26]

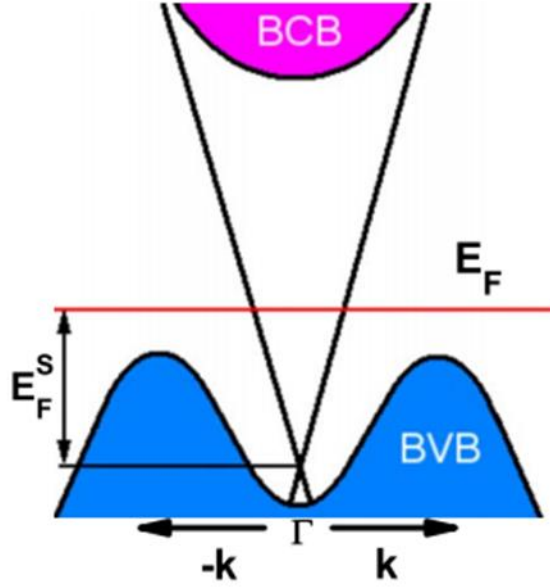


Figure 3.2 Schematic of the band structure of BTS. Adopted from [26].

BTS crystals used in this work are synthesized by the Bridgman technique and the topological nature of crystal is verified by ARPES measurement (details are in [107]). We launch and detect propagating surface plasmons from a nanoscale slit in BTS using NSOM, and observe distinct patterns of the surface plasmons at two different incident wavelengths of 633 nm and 10.6 μm . We attribute this to the surface plasmons from the bulk and the SS of BTS respectively. From the measured optical properties, we conclude that the bulk BTS is plasmonic at the 633 nm wavelength, and the plasmon wavelength is on the order of the incident wavelength as expected for bulk materials [4]. However, at the infrared wavelength of 10.6 μm , the extracted plasmon wavelength is very short - more than 100 times smaller than the incident wavelength. This is due to the two dimensional nature of SS, similar to that observed in graphene [97], [98]. The strong optical confinement of the surface state plasmons can be exploited for various applications including integrated optical circuits and subwavelength optical devices [108].

3.2 Optical Measurements and Modelling of Optical constants

BTS flakes are prepared by tape exfoliation from the bulk and are characterized by Raman spectroscopy. The Raman spectrum of BTS flake exfoliated onto a SiO₂/Si substrate is shown in Figure 3.3. It shows three typical phonon modes of BTS [109].

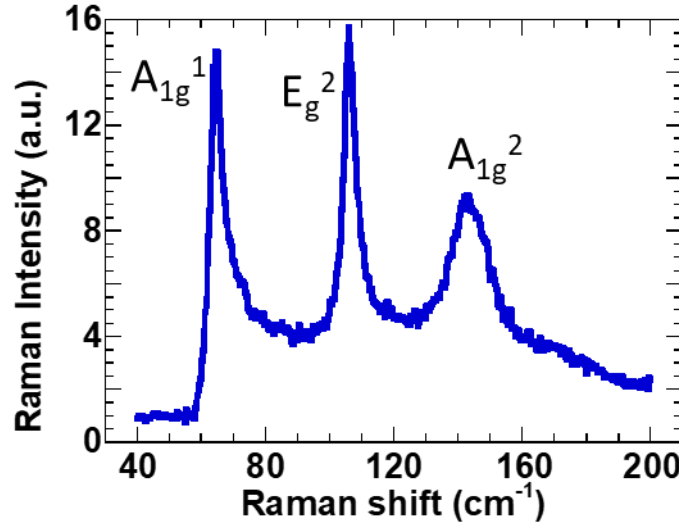


Figure 3.3 Raman characterization of BTS flakes on SiO₂/Si substrate.

We first investigated the optical properties of BTS flakes by reflection and transmission measurements. For the wavelengths from 480 nm to 1600 nm, optical measurements are performed using a home-built system with BTS exfoliated on calcium fluoride (CaF₂) substrate. Vasudevan Iyer built the system and helped in the optical measurements. The light source is a quartz tungsten halogen lamp and spectrometers (UV-VIS Ocean Optics and Princeton instruments Acton SP2300) are used to obtain the spectral information. For wavelengths from 2.5 μ m to 11 μ m, an undoped Si substrate is used and measurements are performed using commercial Fourier-transform infrared spectroscopy (Thermo Nicolet Nexus 670 FTIR) as CaF₂ is opaque beyond \sim 9 μ m. Experimentally obtained reflection and transmission of a 15 nm flake on CaF₂ substrate from wavelengths 480 nm to 1600 nm are shown in Figure 3.4a and Figure 3.4b. Reflection and transmission of a 55 nm flake

on Si substrate from wavelengths 2.5 μm to 11 μm are shown in Figure 3.4c and Figure 3.4d. A thicker (and larger) film is used for IR measurements since the spot size of the IR beam is larger, which requires a larger flake. Also shown in Figure 3.4 are the optical measurements by the fitted dielectric constants (explained later).

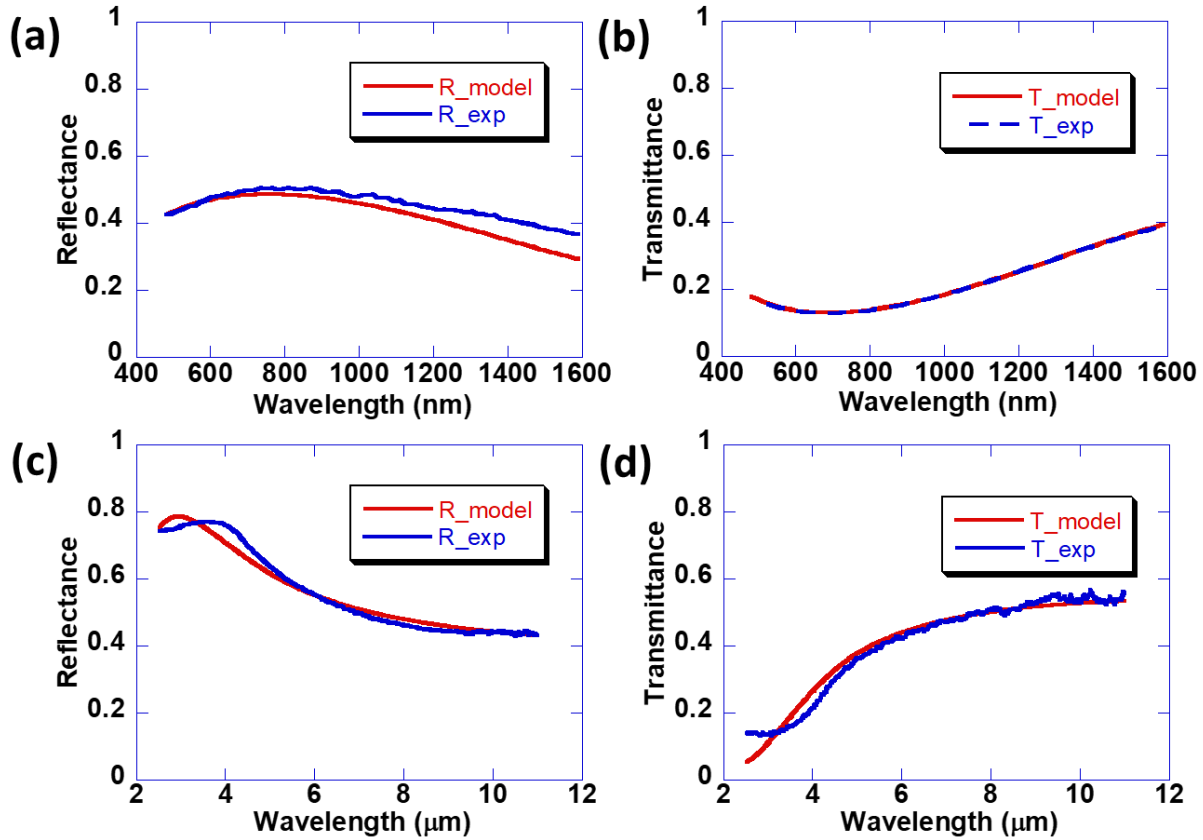


Figure 3.4 Optical measurements of BTS flake. (a), (b) Reflectance and transmittance of 15 nm BTS flake on CaF_2 substrate and (c), (d) Reflectance and transmittance of 55 nm BTS flake on undoped Si substrate. R_{exp} and T_{exp} are the experimental reflectance and transmittance respectively. R_{model} and T_{model} are the reflectance and transmittance from the fitted dielectric constants.

The optical measurements were then used to obtain optical properties of the surface layer and bulk BTS. We modelled BTS as a three-layer material i.e., surface layer, bulk, and surface layer. The surface layer is modelled as a Drude layer and the bulk is modelled using a Tauc-Lorentz

model as in other topological materials [99]. The dielectric constants of surface layer by the Drude model [99], [110] is given as,

$$\epsilon_1 - i\epsilon_2 = \epsilon_\infty - \frac{\omega_p^2}{\omega^2 - i\Gamma\omega} \quad (3.1)$$

where, ϵ_1 and ϵ_2 are the real and imaginary part of the dielectric constant, ϵ_∞ is the high frequency dielectric constant, ω_p is the plasma frequency, and Γ is the damping rate.

The imaginary part of the dielectric constant in the Tauc-Lorentz model (for bulk) with a single oscillators is given as, [99], [111], [112]

$$\epsilon_2(E) = \frac{AE_0C(E - E_g)^2}{(E^2 - E_0^2)^2 + C^2E^2} \frac{\Theta(E - E_g)}{E} \quad (3.2)$$

where, $\theta(x)$ is a step function, equal to 0 for $x < 0$ and equal to 1 for $x > 0$, E_g is the band gap, E_0 is the peak transition energy of the oscillator, A is the amplitude of the oscillator, C is the broadening term. With multiple oscillators (N), the imaginary part of dielectric constant is the summation of individual oscillators[112].

$$\epsilon_2(E) = \sum_{i=1}^N \frac{A_i E_{0i} C_i (E - E_g)^2}{(E^2 - E_{0i}^2)^2 + C_i^2 E^2} \frac{\Theta(E - E_g)}{E} \quad (3.3)$$

where, E_{0i} is the peak transition energy, A_i is the amplitude, and C_i is the broadening term of the i^{th} oscillator.

The real part (ϵ_1) of the dielectric constant is then obtained by the Kramers Kronig integration [111], [113].

$$\epsilon_1(E) = \epsilon_\infty + \frac{2}{\pi} P \int_{E_g}^{\infty} \frac{\xi \epsilon_2(\xi)}{\xi^2 - E^2} d\xi \quad (3.4)$$

Where P stands for the Cauchy principal part of the integration and ϵ_∞ is the high frequency dielectric constant.

The slight absorption below the band gap (Figure 3.6) cannot be modelled by just a single layer (bulk) and shows the significance of surface layers. A three-layer model is needed in our analysis due to optically thin films, not a two-layer model as in other optically thick topological materials [99]. The top and bottom surface layer are modelled with the same dielectric constants. MATLAB code for Fresnel equations in a multilayer structure is used to obtain the optical constants.

In modelling the Tauc-Lorentz and Drude models, the following parameters are used: band gap (E_g) = 0.24 eV from the transmission and absorption measurements, ϵ_∞ (Drude) = 1, and Γ = 0.086 eV and thickness of the Drude layer = 1.28 nm from ref [114]. Two Tauc-Lorentz oscillators (fitted at 1.69 eV and 0.49 eV) are used. The fitted parameters of the Drude and Tauc-Lorentz model are summarized in Table 3-1.

Table 3-1 Parameters of Tauc-Lorentz & Drude model fitted to the optical measurements.

E_{01} (Tauc-Lorentz, eV)	1.69
C_1 (Tauc-Lorentz, eV)	1.85
A_1 (Tauc-Lorentz)	98
E_{02} (Tauc-Lorentz, eV)	0.49
C_2 (Tauc-Lorentz, eV)	0.16
A_2 (Tauc-Lorentz)	41.1
ϵ_∞ (Tauc-Lorentz)	5
ω_p (Drude, eV)	1.39

The dielectric constants of bulk BTS and surface layer obtained by the three-layer model are shown in Figure 3.5a. We used the same optical properties for both 15 nm and 55 nm, and the reflectance and transmittance from the fitted dielectric constants are shown in Figure 3.4. The dielectric constants of bulk BTS till 1.6 μm is plotted in Figure 3.5b. Negative permittivity is observed below 650 nm. This bulk plasmonic response is attributed to the interband absorption dispersion and is not from the bulk free carriers as reported for BSTS [99]. From the dielectric

constants shown in Figure 3.5a, we see that there are two peaks in ϵ_2 of bulk, at ~ 800 nm and ~ 2.5 μm . These two peaks are in reasonable agreement with DFT calculations where the first peak in the visible region is attributed to the interband transition near the Γ point in the momentum space and the other peak is due to the transition around the (0.33, -0.5, -0.5) point[114].

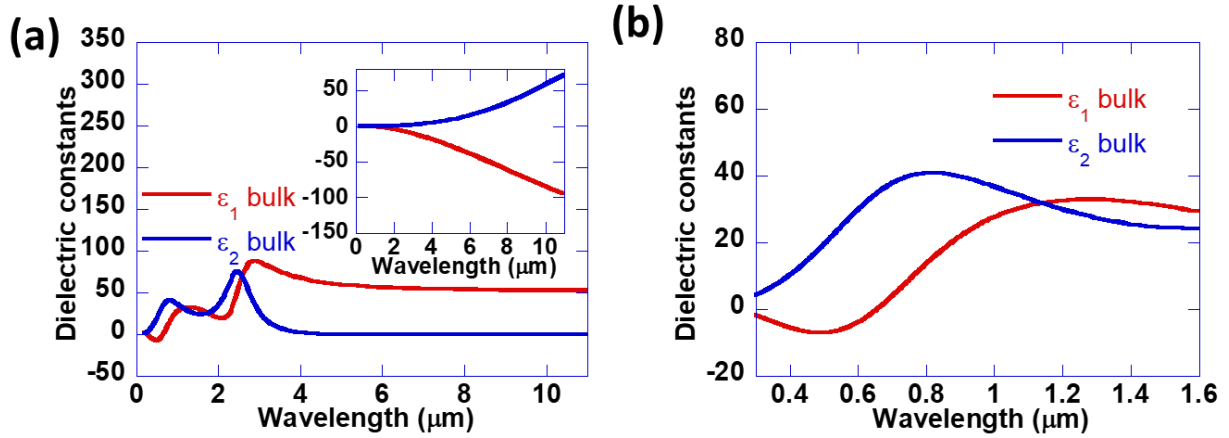


Figure 3.5 Dielectric constants of BTS. (a) Bulk BTS. The inset shows the dielectric constants of the surface layer and (b) enlarged view of the bulk BTS properties in the visible and near IR region.

The absorbance ($1 - \text{reflectance} - \text{transmittance}$) of a 55 nm flake obtained from FTIR is shown in Figure 3.6. The absorption (A_{model}) from the fitted optical constants is also shown in the figure. We can clearly see the band edge of BTS at ~ 5 μm and also the slight absorption at energies below the band gap of BTS, which is due to SS.

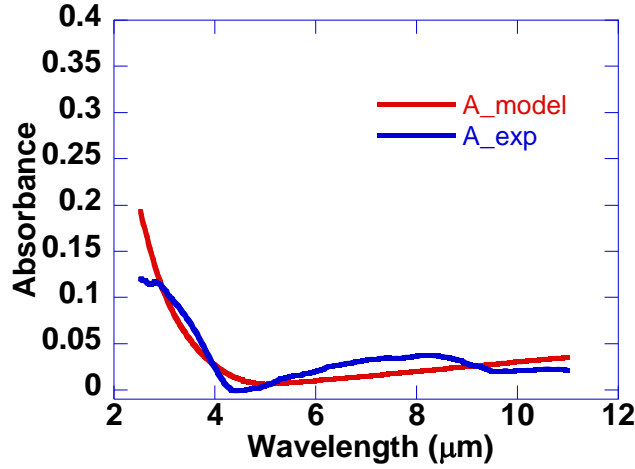


Figure 3.6 Absorption measured using FTIR on a 55nm BTS flake on Si substrate. A_exp is the experimental absorption and A_model is from the model.

3.3 Imaging of the Surface Plasmons from the Bulk

To verify the plasmonic behavior of bulk BTS, we use scattering NSOM to image the surface plasmons launched by a nanoscale slit in BTS flake. BTS flakes are exfoliated onto a SiO₂/Si substrate and slits are fabricated using focused ion beam milling. The thickness of oxide is 270 nm. Near-field measurements are performed by Dr. Xiaolei Wen at University of Science and Technology of China.

Near-field measurements are carried out using a commercial scattering-type NSOM system (Neaspec GmbH) equipped with a visible laser of 633 nm wavelength and an infrared laser of 10.6 μm. The NSOM system is based on an AFM system of tapping mode: a sharp AFM tip (typically with a curvature radius about 20 nm) was approached to the surface of the sample and vibrated vertically with a 50-nm amplitude at a frequency around 260 kHz. TM polarized light of 633 nm was focused and incident via a parabolic mirror onto both the tip and sample at an angle of 47° to the surface normal. The tip-scattered light was then recorded by a pseudo-heterodyne interferometer. In order to suppress background scattering, the detected signal was demodulated at higher harmonic frequencies. Both Si and Pt tips are used for 633 nm measurements.

The in-plane component of incident light is perpendicular to the slit as shown in Figure 3.7a(i). The near-field amplitude from NSOM measurements for two BTS flakes, 77 nm thick (slit width 240 nm) and 15 nm thick (slit width 230 nm) is shown in Figure 3.7a and Figure 3.7b respectively. (i) in each figure shows AFM topography and (ii) shows the near-field amplitude. The near-field amplitude at the slit on another 63 nm thick flake is shown in Figure 3.8. The line profile of the near-field amplitude across the blue line in Figure 3.7a,b(ii) is shown in Figure 3.7a,b(iii). These measurements are performed using a silicon tip.

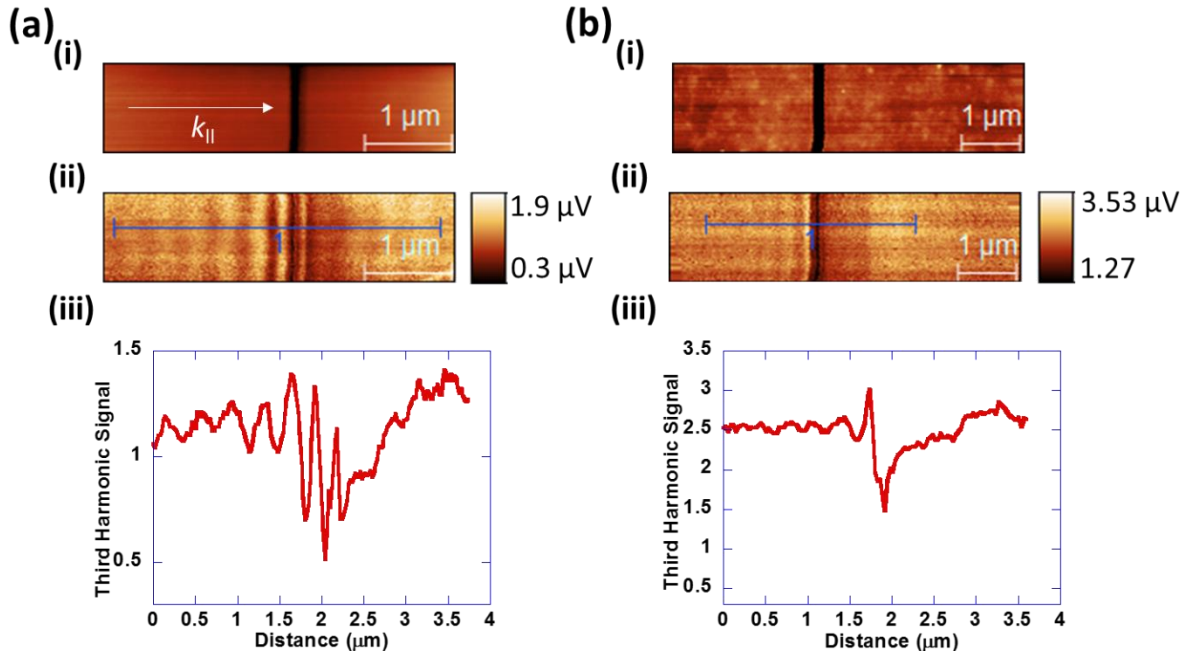


Figure 3.7 Near-field amplitude image at 633 nm obtained using scattering NSOM. (i) AFM topography, (ii) NSOM amplitude, and (iii) amplitude profile of the blue line in figure ii, for different BTS flakes. (a) 77 nm thick and (b) 15 nm thick.

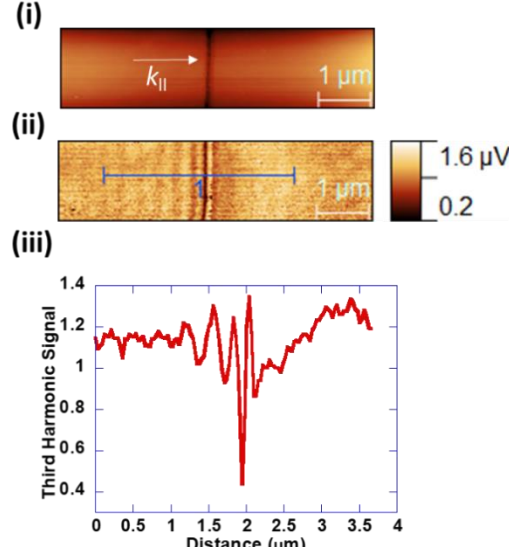


Figure 3.8 Near-field amplitude image at 633 nm on 63 nm thick flake. (i) AFM topography, (ii) NSOM amplitude, and (iii) amplitude profile of the blue line in figure ii.

We observe the interference fringes parallel to the slit on the left side of the slit (side from which light is incident). These interference fringes are a result of interference between the surface plasmons from bulk BTS ($\text{Real}(\epsilon) < 0$, Figure 3.5), launched at the slit, and the in-plane component of the incident light [115], [116]. The TM polarized light can launch surface plasmon polaritons on both sides of a slit, which propagate away from the slit [115]. These surface plasmons interfere with the incident field, forming fringes on both sides of the slit [115], [116]. Due to the different propagation directions of the surface plasmons with respect to the incident field, the interference fringe periods are different on the two sides of the slit and can be described as [115], [116],

$$\Lambda^- = \lambda_0 \lambda_{SP} / (\lambda_0 + \lambda_{SP} \cdot \sin(\theta) \cos(\varphi)) \quad (3.5)$$

$$\Lambda^+ = \lambda_0 \lambda_{SP} / (\lambda_0 - \lambda_{SP} \cdot \sin(\theta) \cos(\varphi)) \quad (3.6)$$

Where, Λ^- is the fringe period on the incident light side, Λ^+ is the fringe period on the other side, λ_0 is the wavelength of the incident light, λ_{SP} is the wavelength of the surface plasmons, θ is the angle of incidence with respect to the surface normal (oblique angle of 47° in our experiments),

and φ is the complementary angle between the in-plane component of incident light and the slit (angle of 0° as in the case of experiments in Figure 3.7 and Figure 3.8). The λ_{SP} at the interface of dielectric (ϵ_1) and metal (ϵ_2) is given as[4]

$$\lambda_{SP} = \frac{\lambda_0}{\text{Real}\left(\sqrt{\frac{\epsilon_1 \epsilon_2}{\epsilon_1 + \epsilon_2}}\right)} \quad (3.7)$$

Considering air, $\epsilon_1 = 1$ and bulk BTS, $\epsilon_2 = -1.55 + i33.06$ (from Figure 3.5) at the incident wavelength of 633 nm, the periods Λ^- and Λ^+ estimated from equations (3.5) and (3.6) are 365 nm and 2.35 μm respectively. From Figure 3.7 and Figure 3.8, we observe the interference fringes to the left side of the slit but no fringe to the right of the slit due to the finite scan window. (A large scan is shown later in Figure 3.9b). The experimental fringe spacing to the left of the slit of 15 nm, 63 nm and 77 nm thick flakes are 315 nm, 364 nm, and 301 nm, which are in close agreement to the estimated fringe spacing. Hence the observed interference fringes can indeed be attributed to the interference of surface plasmons from the bulk BTS and the incident beam.

To further illustrate the formation of fringes, numerical calculations are performed using the finite element electromagnetic solver, ANSYS EM 17.1 with radiation boundary conditions. The geometry consists of air, BTS, and SiO₂/Si substrate. BTS is modelled as three-layer material, with optical properties of bulk and surface layer from the fitted optical constants. Light is illuminated from air side with an oblique incident angle of 47° and TM polarization. A Gaussian beam with radius of 2 μm is focused at the center of the slit. The simulation model consists of a 77 nm BTS film on top of a SiO₂/Si substrate with a 240 nm wide slit as in the experiment. The results of the electric field at 2 nm above the BTS surface is shown in Figure 3.9 a(ii). As NSOM is more sensitive to the vertical component of the electric field[117], the simulation result of the electric field component E_z , on a line along the x-axis (see Figure 3.9a (i)) is shown in Figure

3.9a(iii). We clearly see the fringes on the left side of the slit and the intensity variation on the right. The simulated fringe spacing to the left of the slit is 359 nm. However, the fringe spacing of 2.35 μm on the right side of the slit cannot be observed precisely due to the limited size of the Gaussian beam (radius = 2 μm). The experimental results of a large area scan is shown in the Figure 3.9b. The experimental fringe spacing to the left of the slit is 360 nm, and is over 2 μm on the right side, in agreement with numerical calculations.

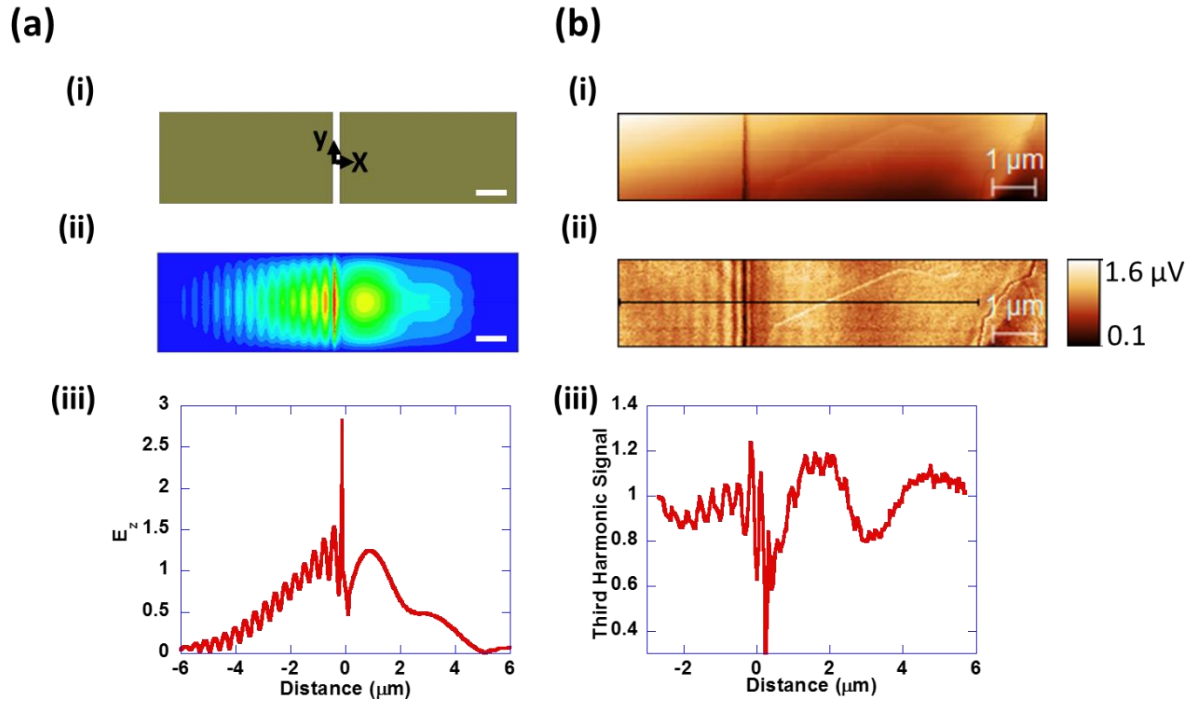


Figure 3.9 Comparison of the numerical and experimental results at 633 nm. (a) Numerical calculation of a Gaussian beam of radius 2 μm radiating on the nanoslit. Scale bar is 1 μm . (i) Geometry of the simulation showing the slit. (ii) Electric field distribution on a plane, 2 nm above surface. (iii) Line profile of E_z at the center of the plane (along the x-axis) 2 nm above the surface. (b) Near-field amplitude image at 633 nm using scattering-type NSOM (i) AFM topography (ii) s-NSOM amplitude (iii) Amplitude profile of the black line in Fig. b(ii).

From the analytical model, the fringe period on the left side of the slit, Λ^- , increases with ϕ . To further illustrate the interference fringes, we did near-field experiments with different orientations of nanoslit (ϕ) with respect to the in-plane component of the incident light and the

results are shown in Figure 3.10. These measurements are performed with Pt tip. We observe that the fringes are still parallel to the nanoslit. The line profiles of the near-field amplitude on the incident side of the slit (perpendicular to the slit) at different ϕ angles of 5° , 50° , 70° for a 77 nm thick BTS flake (slit width 240 nm) are shown in the Figure 3.10. The fringe spacings with different ϕ angles of 5° , 50° , 70° are 383 nm, 396 nm, 485 nm respectively and the fringe spacings calculated using equation (3.5) are 366 nm, 430 nm, and 506 nm respectively. The observed fringe spacings increase with ϕ and are in a reasonable agreement with the analytical model.

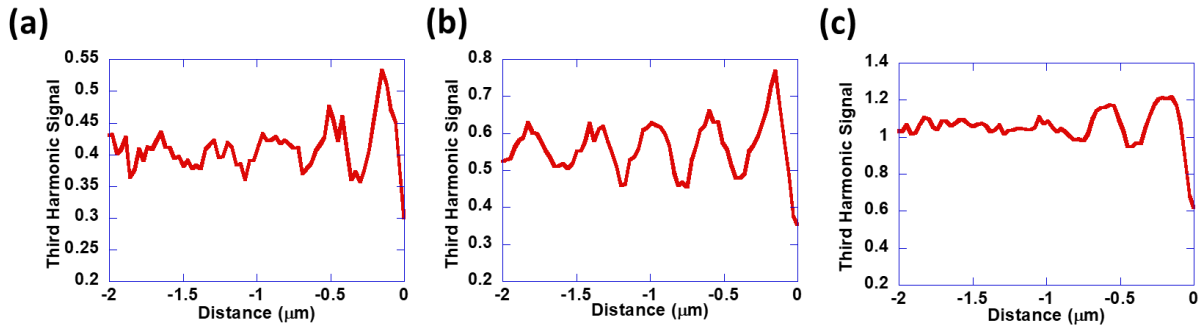


Figure 3.10 Line profile of the near-field amplitude on incident light side of the slit at 633 nm, using scattering-type NSOM for different slit orientation with in-plane component of incident light for 77 nm thick flake. Orientation (ϕ) of (a) 5° (b) 50° (c) 70° .

It is known that AFM tip can also launch surface plasmons [118]. Interference patterns were observed in graphene at infrared wavelength and interpreted as the interference of surface plasmons launched by the AFM tip and its reflection at the boundary [97], [98]. In our experiments, different fringe spacing on either side of the slit and the variation of fringe spacing at different slit orientations cannot be explained by surface plasmons launched by the tip. For tip launched plasmons, the fringe spacing would be the same on either side, and the spacing is invariant with the slit orientation. Hence, in our case the observed fringes are formed by the interference of surface plasmons launched at the slit and the incident field, with minimal effect from the tip.

3.4 Imaging of the Surface Plasmons from the Surface State

To study the plasmons of the surface state, the sample is illuminated with a below (bulk) band gap energy, 10.6 μm laser, at an oblique angle with TM polarization. Pt tip is used for the infrared measurements to increase the signal. The band gap of the bulk BTS from our measurements and literature [119] is ~ 0.24 eV. With a below band gap excitation energy of 0.116 eV (10.6 μm wavelength), there will be no contribution from the bulk. The in-plane component of the incident light is perpendicular to the slit as shown in Figure 3.11a(i). The near-field amplitudes from NSOM measurements for two BTS flakes 15 nm and 77 nm thick are shown in Figure 3.11a and Figure 3.11b respectively. The line profile of the near-field amplitude is shown in Figure 3.11(iii). The near-field amplitude at the slit on another 63 nm thick flake is shown in Figure 3.12. We observe a fringe spacing of ~ 49 nm on the left side of the slit and ~ 55 nm on the right side of the slit for the 15 nm thick flake, and ~ 36 nm on the left side of the slit and ~ 50 nm on the right side of the slit for the 63 nm thick flake, and ~ 51 nm on the right side of the slit for the 77 nm thick flake. (The fringe spacing on the left side of the slit for 77 nm flake cannot be determined precisely.) Hence, all of the observed fringe spacing is ~ 50 nm, much smaller than the incident wavelength $\sim (\lambda/200)$.

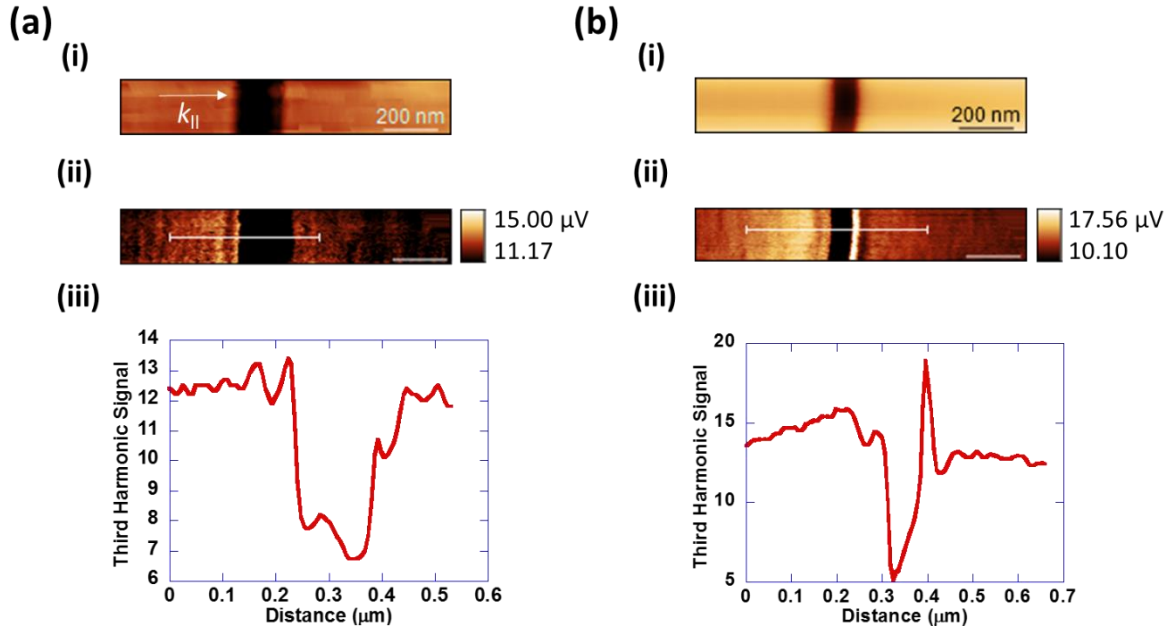


Figure 3.11 Near-field amplitude image at 10.6 μm using scattering-type NSOM. (i) AFM topography, (ii) s-NSOM amplitude, and (iii) Amplitude profile of the white line in figure ii, for different BTS flakes. (a) 15 nm thick and (b) 77 nm thick. All scale bars are 200 nm.

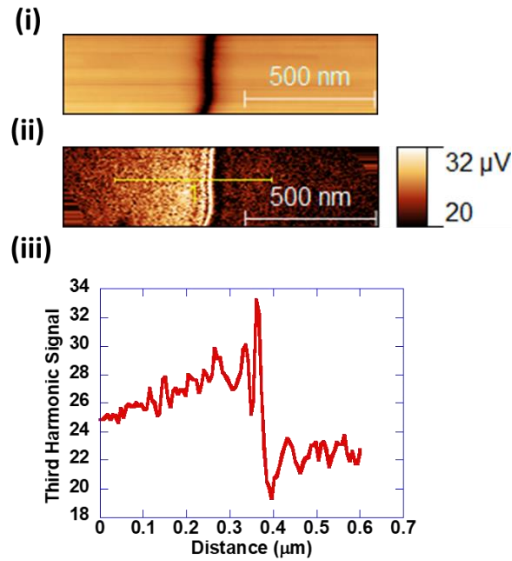


Figure 3.12 Near-field amplitude image at 10.6 μm on 63 nm thick flake. (i) AFM topography, (ii) NSOM amplitude, and (iii) amplitude profile of the yellow line in figure ii.

We note that the near-field signal is weak and to confirm the fringes, line scans at different locations and Fourier transform of the line scan of 15 nm flake and 77 nm flake are performed and are shown in Figure 3.13 and Figure 3.14. Figure 3.13a(i) and Figure 3.13b(i) show the near-field signal for 15 nm and 77 nm flakes respectively. Line scans of the near-field signal (displaced) across different lines shown in Figure 3.13(i) are shown in Figure 3.13(ii). We can see that the discernable fringe spacing across different lines is similar. Also, Fourier transform of the line scan (excluding the slot edge) is shown in Figure 3.14(a) and Figure 3.14(b) for 15 nm and 77 nm respectively. We see the frequency component $\sim 0.018 \text{ nm}^{-1}$, corresponding to a fringe spacing of $\sim 55 \text{ nm}$.

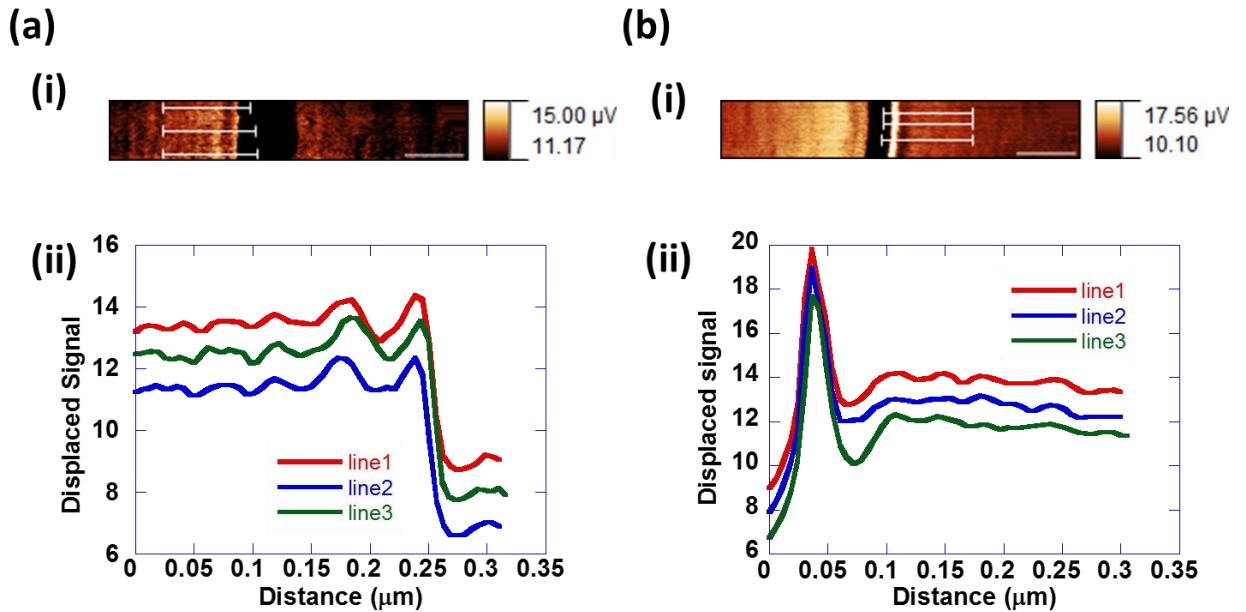


Figure 3.13 Line scans of near-field measurement at 10.6 μm wavelength for (a) 15 nm flake and (b) 77 nm flake. For both the flakes, (i) near-field signal (scale bar = 200 nm) and (ii) Line scan of the (displaced) near-field signal across the white lines shown in (i)

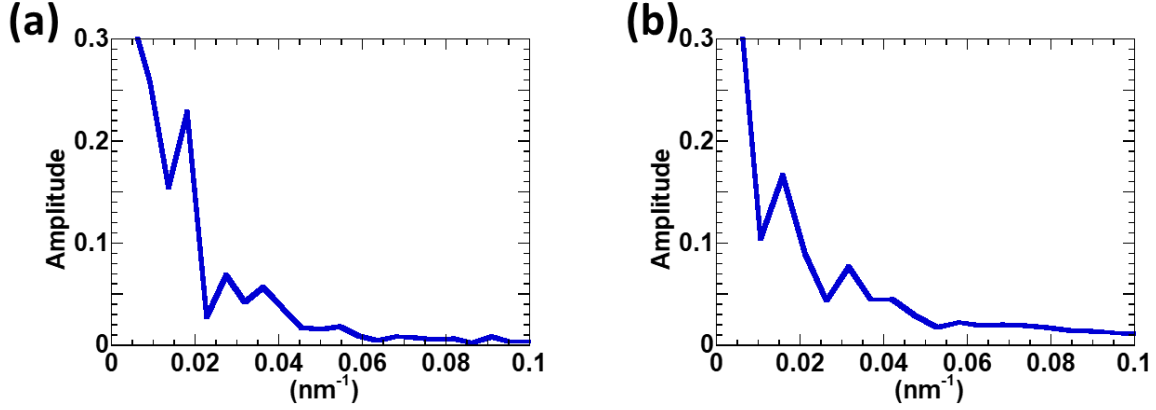


Figure 3.14 Fourier Transform of the line scan of the near-field signal at 10.6 μm wavelength for (a) 15 nm flake and (b) 77 nm flake.

The smaller fringe spacing is attributed to the plasmons from the surface state of topological insulator. Small fringe spacing of plasmons were reported for graphene, ~ 100 nm (with $11.2 \mu\text{m}$ incident wavelength) [97] and ~ 130 nm (with $9.7 \mu\text{m}$ incident wavelength) [98]. These small fringe spacings in graphene were explained with the theory of plasmons in two dimensional metal. The origin of fringes was interpreted as the interference of the plasmons launched by the AFM tip and its reflection from the boundary of the graphene, with a fringe spacing of half the plasmon wavelength. Another study also confirmed tip excited plasmons in graphene with $10.6 \mu\text{m}$ excitation wavelength [120]. One of the features in tip excited plasmon is that the fringe spacing is half of the plasmon wavelength [98], [120]. Here, we also interpret our fringe spacing as the interference between tip launched plasmons and its reflection. Hence, the plasmon wavelength of surface state excited by $10.6 \mu\text{m}$ wavelength is ~ 100 nm (from the fringe spacing of ~ 50 nm), similar to that in graphene.

To illustrate further, the surface plasmons arising from the surface state of the topological insulator is analyzed as Dirac plasmons from 2D electrons [99]. In thin films, surface electrons at the interfaces of topological insulator-vacuum and topological insulator-substrate interact via an

effective Coulomb potential [121]. This interaction produces two plasmon modes, optical and acoustic plasmon modes [102], [121], [122]. The dispersion of the acoustic mode depends on the permittivity of the topological insulator bulk and is strongly Landau-damped (i.e., not observable) [102]. The dispersion of the optical mode depends on the permittivity of the outer dielectric media (air and substrate in our case) [121], [122], is given by the following expression: [102]

$$\nu(k) = \frac{1}{2\pi} \sqrt{k} \left(\frac{e^2}{4\pi\epsilon_o\epsilon(h/2\pi)} v_f \sqrt{2\pi n_d} \right)^{1/2} \quad (3.8)$$

Where ϵ is the averaged dielectric constants of the air and substrate, v_f is the Fermi velocity, n_d is the carrier density, ν is the frequency of the light, e is the electronic charge, and ϵ_o is the permittivity of free space. In our BTS, with a Fermi velocity [107] of 6×10^5 m/s and SS carrier concentration of $n_d \sim 10^{13} \text{ cm}^{-2}$ [109], [123], we obtain an SS plasma wavelength of $\lambda_p = 2\pi/k$ as 74 nm, slightly smaller than the average measured value which can be due to various factors such as variation in the carrier concentration and accuracy in the fringe spacing measurements.

Short wavelength of SS plasmons in mid IR with a ratio ($\frac{\lambda_{IR}}{\lambda_p}$) of 106 (λ_{IR} is the incident wavelength and λ_p is the plasmon wavelength) is observed, much higher than that of the metals. The plasmonic behavior at mid IR wavelengths can open up various applications including thermal radiation control, surface enhanced spectroscopy [124] and broadband plasmonic devices. Plasmonic switching and active control of the SS plasmons by electrical gating as in graphene [97], [98] should also be possible. In addition, spin polarized SS provide exciting opportunities for plasmon-spintronic devices controllable by external EM or magnetic fields [125].

3.5 Summary

The studies above show that BTS exhibit plasmonic behavior across a wide wavelength range. The plasmonic response in mid IR arises from SS and is dominated by bulk in VIS-UV wavelengths. We studied the surface plasmons arising from bulk and SS of BTS. Surface plasmons arising from bulk are studied using the incident wavelength of 633 nm and surface plasmons from SS are studied with a below band gap excitation of 10.6 μm . The plasmon wavelength of the bulk is on the order of incident light wavelength, in sharp contrast to the very short SS plasmon wavelength - more than 100 times smaller than the incident light wavelength. The short SS plasmon wavelength is due to the two dimensional nature of SS, similar to the plasmon behavior in graphene. The strong optical confinement of the surface state plasmons can be exploited for various applications including integrated optical circuits and subwavelength optical devices.

4. INVERSE DESIGN OF NEAR-FIELD TRANSDUCER FOR HEAT-ASSISTED MAGNETIC RECORDING USING TOPOLOGY OPTIMIZATION

In this chapter, density-based topology optimization for inverse design of near-field transducer (NFT) for a desired temperature profile in the recording medium for heat-assisted magnetic recording (HAMR) is discussed. NFT designs for both generating a small heated spot size and a heated spot with desired aspect ratio in recording medium are demonstrated. Also, the effect of waveguide, write pole and moving recording medium is studied with the obtained NFT designs.

4.1 Introduction

The primary goal of HAMR is to heat the recording medium locally (few 10s of nm) which is much smaller compared to the diffraction limit of the light wavelength (800 nm) used in the HAMR system for heating the recording medium. HAMR system uses a metallic nano antenna/aperture also known as NFT, and locally heats by concentrating the light below the diffraction limit using surface plasmons [28]. Several NFT designs have been investigated including triangle antenna, E antenna, lollipop antenna, bowtie apertures and C apertures [28], [29], [126]–[131]. Traditional design approaches use parameter sweep in optimizing the geometry of the design i.e., highly constrained optimization without changing the topology in general.

In this work, we use topology optimization for inverse design of NFT for a desired temperature profile in the recording medium. With topology optimization, unexpected NFT topology may be produced which possibly gives an optimized solution that may not be obtained with intuition using a traditional parameter sweep of the design. Topology optimization has been used in various applications including improving coupling efficiency of nano-photonic grating

coupler, localizing and enhancing electromagnetic energy using Ag antenna-strip, designing waveguide for HAMR, designing the magnet for a desired magnetic field, maximizing bandgap in photonic crystals, designing nanostructures for extraordinary optical transmission, and surface plasmonic cloaking [132]–[137]. In this work, we first perform an inverse thermal calculation to obtain a required volumetric heat generation (electric field) in the recording medium for achieving a desired temperature profile. We use FePt as a recording medium and the curie point of FePt at 750 K [138]. We consider a targeted temperature rise of 450 K for 1 ns of heating in a desired heated region. We then perform an inverse electromagnetic field calculation for NFT design using topology optimization to generate a required electric field in the recording medium. This optimization is carried out by minimizing an objective function which is the difference between the electric field generated by the NFT and the targeted electric field in the recording medium, using a discrete adjoint method with Finite-Difference Time-Domain (FDTD) as a solver. Zhou Zeng has developed the method and details have been given in a previous work in which reconstructing the electric field of a plasmonic bowtie aperture has been demonstrated [139]. We use this inverse design procedure to find NFTs for producing different targeted rectangular heated spot size in the recording medium. We also attempt to find the smallest heated spot in the recording medium. The heated spot size at 20 K and 50 K below the maximum temperature rise of 450 K, and the required laser power for each design are compared. The effect of waveguide, write pole and moving recording medium on the heated spot size is studied with the obtained NFT designs.

4.2 Inverse thermal and electromagnetic design

We considered a simplified HAMR system, and the geometry of the simulation model is shown in Figure 4.1. Figure 4.1a shows the side view of the simulation model. It consists of air, the NFT, and the recording medium. The NFT is made of gold with a thickness of 60 nm and a

recording medium is a 10 nm-thick FePt film. A 4 nm thick air gap is considered between the NFT and FePt recording medium.

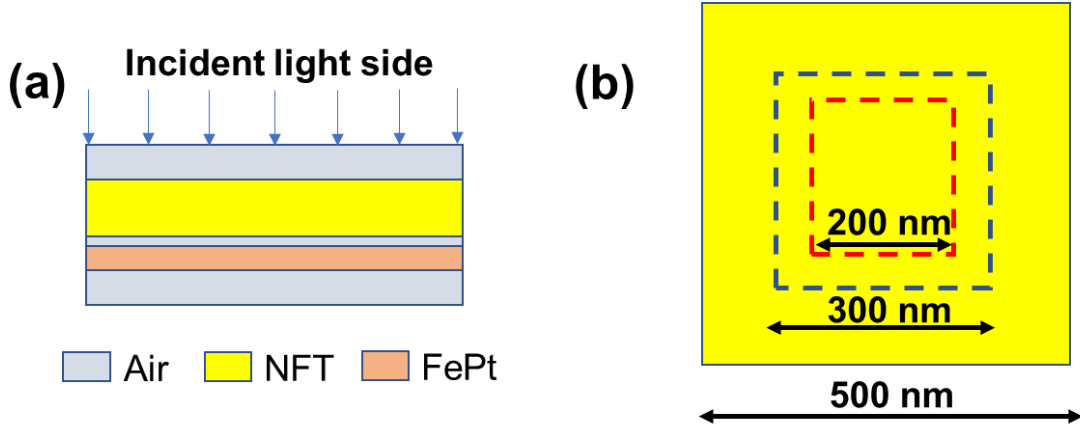


Figure 4.1 Schematic of HAMR system considered in electromagnetic field simulation (a) Side view; Stack from incident light side: air, 60 nm-thick NFT (gold), 4 nm-thick air, 10 nm-thick FePt, air. (b) Top view showing the simulation domain of 500 nm x 500 nm, the design region of NFT 200 nm x 200 nm, and the field reconstructing region of 300 nm x 300 nm at the mid plane in the FePt medium which is also shown by the dotted line in (a).

We perform the inverse thermal design by considering a two-dimensional FePt recording film, i.e., the temperature in the FePt is uniform in the thickness direction. The thermal properties of FePt are obtained from [140]. For an infinite two-dimensional space, the temperature rise can be obtained by the convolution product of the volumetric heat generation q and the Green's function G [141] :

$$\Delta T(r, t) = \frac{\alpha}{k} \int_0^t \int_{R^2} G(r - r', \tau) q(r') d^2 r' d\tau \quad (4.1)$$

where r is the coordinate vector and $G(r, \tau)$ is given by:

$$G(r, \tau) = \frac{1}{4\pi\alpha\tau} e^{-\frac{|r|^2}{4\alpha\tau}} \quad (4.2)$$

Here, we assumed that there is no heat loss from this two-dimensional surface, i.e., no effective heat transfer coefficient. Zhou Zeng has developed the inverse thermal code with the

convolution product of the volumetric heat generation and the Green's function. We intend to find a required volumetric heat source q that generates a uniform temperature profile within a given rectangular region in the recording medium after the medium is heated for 1 ns. The temperature rise in this region is 450 K. The volumetric heat generation to produce this temperature profile is obtained from the following optimization/minimization calculation:

$$\begin{aligned} \min_q \quad & 0.5 \iint_{r \in A} (\Delta T(r, t_o) - 450)^2 d^2r \\ \text{subject to:} \quad & \Delta T(r, t) = \frac{\alpha}{k} \int_0^t \int_{R^2} G(r - r', \tau) q(r') d^2r' d\tau \\ & \text{and } q_l \leq q \leq q_u \end{aligned} \tag{4.3}$$

where q_l, q_u are the lower bound and the upper bound of the volumetric heat source. In our calculation, we use a nominal absorption $q_o = 2.77 \times 10^{18} \text{ W} / \text{m}^3$ (a diode laser of 3 mW power, 300 nm beam waist, and 800 nm wavelength that is completely absorbed by the medium), and assign values to the lower bound and upper bound by $q_l = 0.008q_o$ and $q_u = 10q_o$. The lower bound is set to a very low value that does not have influence on the calculation results. The upper bound is found by trial and error as the maximum q found is about $3.62 q_o$ hence this upper bound is sufficient. We use the L-BFGS-B (limited memory Broyden-Fletcher-Goldfarb-Shanno with bound constraints) algorithm to solve the problem as a local gradient-based optimization [142]. Inverse thermal calculations are performed on a domain of 300 nm x 300 nm, with a 2 nm grid size. A direct solution for the above optimization problem can produce very sharp peaks (with half width half maximum of $\sim 1 \text{ nm}$) for the volumetric heat source q . We found that the electromagnetic optimization produces structures that does not have sharp peaks. Therefore, we can also impose a Gaussian filter function $w = e^{-\frac{|r|^2}{2a^2}}$ on the volumetric heat generation, $q_f = q * w$ to reduce the sharpness of the peaks and reduce computation time, where q_f is the filtered

absorption and $*$ denotes convolution. We used a Gaussian filter of radius $a = 2$ nm. As a result, the final optimization is given by:

$$\begin{aligned} \min_q \quad & 0.5 \iint_{r \in A} (\Delta T(r, t_o) - 450)^2 d^2 r \\ \text{subject to:} \quad & \Delta T(r, t) = \frac{\alpha}{k} \int_0^t \int_{R^2} G(r - r', \tau) q_f(r') d^2 r' d\tau \\ & q_l \leq q \leq q_u \text{ and } q_f = q * w \end{aligned} \quad (4.4)$$

For inverse electromagnetic design, a plane wave of wavelength 800 nm is incident from air onto NFT as shown in Figure 4.1a. The optical properties of air, gold and FePt are taken from [140]. The volumetric heat source due to absorption of electromagnetic energy is related to the electric field as:

$$q''' = \frac{1}{2} \epsilon_o \omega \text{Im}(\epsilon) |E|^2 \quad (4.5)$$

where ϵ_o is the free-space permittivity, ω is the frequency of the light, ϵ is the complex permittivity, and $|E|$ is the magnitude of the electric field. We perform inverse electromagnetic design to obtain an NFT which generates a volumetric heat source (the electric field according to equation (4.5)) in the recording medium that is obtained from the inverse thermal calculation. The top view of the simulation domain is shown in Figure 4.1b with a size of 500 nm x 500 nm, and the field reconstruction area is of 300 nm x 300 nm at the mid plane of the FePt recording medium as shown by the dotted line in Figure 4.1a. The design region of NFT is limited to an area of 200 nm x 200 nm i.e., the region where the density (ρ) can vary between 1 and 0, where 1 represents gold and 0 represents air (aperture). The polarization of the light is in the x-direction (the horizontal direction in Figure 4.1b).

We used the same method as in our previous work of inverse design for reconstructing the electric field of a plasmonic bowtie aperture based on topology optimization [139]. The objective

function of the optimization is to minimize the difference between the electric field E and the desired electric field E_0 on the field reconstruction surface S . We used a density topology optimization with non-linear material interpolation. As a result, we solve the following optimization problem:

$$\min_{\rho} F(E) = \int_S (|E| - |E_0|)^2 dS \quad (4.6)$$

In our calculation, density-based topology optimization based on a discrete adjoint method with FDTD is used in inverse electromagnetic design to guarantee the exactness of gradient calculation. The optimization algorithm starts with density 1 in the design region and is solved iteratively to minimize the objective function. The final design has the density of either 1 or 0 but not the intermediate values. Details of the inverse calculations are given in [139].

Once the inverse designs are completed, we use ANSYS Workbench with the NFT design obtained in topology optimization to compute the electric field, which is then used to calculate the temperature rise of the recording medium after 1 ns of heating using equation (4.1). For doing this, design data of NFT is converted to STL file using MATLAB. The STL file is converted to STEP file using ANSYS Spaceclaim and the STEP file is imported into ANSYS Workbench to perform electromagnetic field calculations.

4.3 Inverse design for generating a heat spot of 30 nm x 60 nm in recording medium

We first perform inverse thermal calculation for generating a rectangular heated spot of 30 nm x 60 nm in the recording medium, i.e., a temperature rise of 450 K in that region after 1 ns of heating. The use of a size of 30 nm x 60 nm or an aspect ratio of 1:2 is due to the elongated geometry of a storage unit in a hard disc drive. The inverse thermal calculation results are shown

in Figure 4.2. Figure 4.2a shows the obtained volumetric heat generation profile for generating the heated spot of 30 nm x 60 nm. From Figure 4.2a we observe that the volumetric heat generation profile has four hot spots at four corners and also has heat generation along the edges to produce a desired temperature rise. The inset in Figure 4.2a shows the isometric view of the normalized volumetric heat generation. Using this volumetric heat generation profile, the corresponding temperature rise in the recording medium is calculated using equation (4.1) and is shown in Figure 4.2b. The line profiles along x and y axes of the temperature rise are shown in Figure 4.2c and Figure 4.2d respectively. From Figure 4.2b, Figure 4.2c, Figure 4.2d, we can see the temperature rise of 450 K in the rectangular region of 30 nm x 60 nm. However, it should be noted that there are finite temperature gradients around the heated region, compared to the steep rise (infinitely large temperature gradient) of the temperature to 450 K in the desired temperature profile. The heat diffusion within the 1 ns heating time causes such a temperature gradient, which is not possible to be avoided.

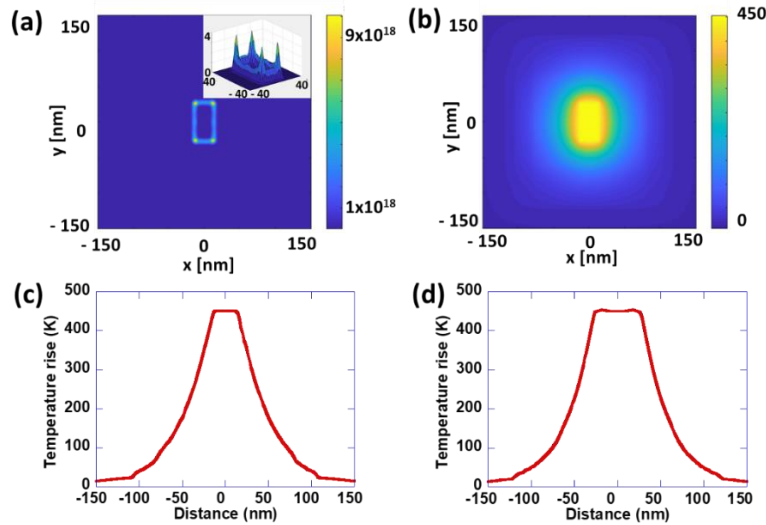


Figure 4.2 Inverse thermal calculation for generating a 30 nm x 60 nm heat spot (a) Obtained volumetric heat generation (W/m³). The inset shows the isometric view of the normalized volumetric heat generation (b) Temperature rise (K) in the recording medium with the volumetric heat generation in Figure 4.2a (c) Temperature rise along the x – axis in Figure 4.2b (d) Temperature rise along y – axis in Figure 4.2b.

With the obtained volumetric heat generation in Figure 4.2a, we calculate the required electric field at mid plane of FePt using equation (4.5). The topology optimization of NFT design is then performed to achieve of this required electric field. The final NFT design from topology optimization as well as the density evolution during the optimization process are shown in Figure 4.3, where density 1 represents gold and 0 represents air (aperture). The blue region in the final NFT design indicates the aperture in the NFT.

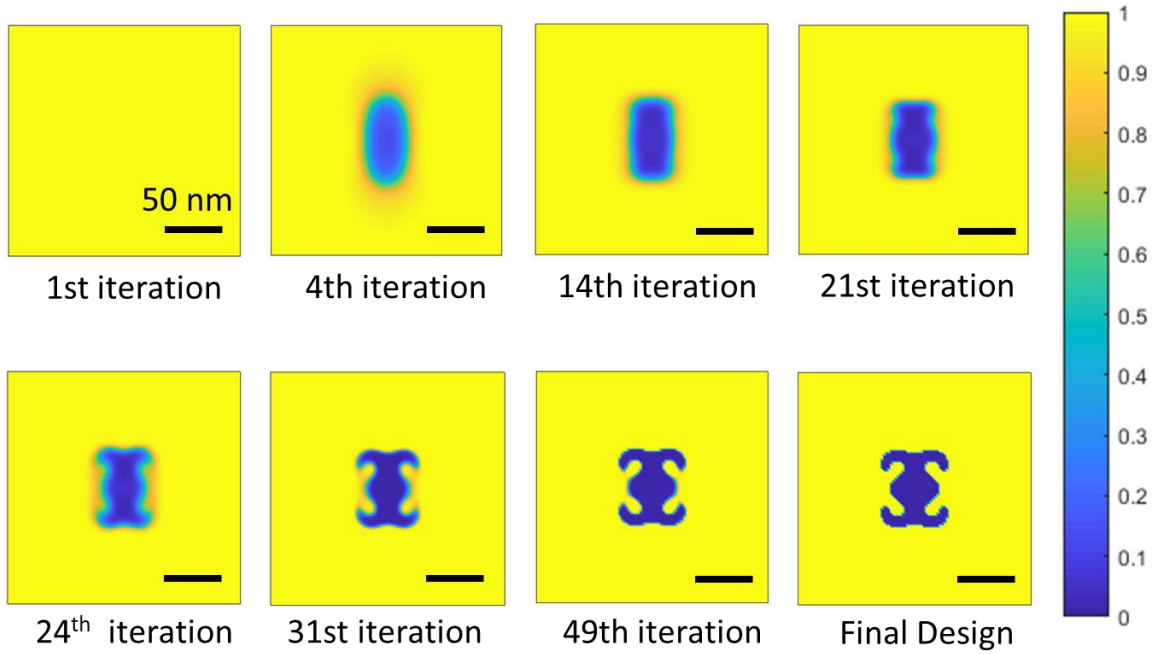


Figure 4.3 Density evolution of NFT and the final NFT design for generating a targeted heated spot of 30 nm x 60 nm in the recording medium. Density 1 represents gold and 0 represents air (aperture). All scale bars are 50 nm.

The obtained NFT is then used to compute the electric field distribution using ANSYS and temperature distribution using equation (4.1) and the results are shown in Figure 4.4. The volumetric heat source in the recording medium produced by the NFT is shown in Figure 4.4a. It is noticed that the NFT does not produce the exact targeted electric field distribution, and the difference with the targeted volumetric heat generation can be seen by comparing with Figure 4.2a.

In other words, the desired volumetric heat generation or electric field with four sharp corners shown in Figure 4.2a cannot be obtained exactly, rather, the designed NFT produces an electric field that minimizes the objective function in equation (4.6). The calculated temperature rise, with the maximum temperature scaled to 450 K, is shown in Figure 4.4b, and the line profiles along x and y axes of the temperature rise are shown in Figure 4.4c and Figure 4.4d respectively. It is seen that heated spot size is about $\sim 29 \text{ nm} \times 39 \text{ nm}$ at 50 K below the maximum temperature. This heated spot size is close to the desired heated spot size along the x-axis, but is reduced along the y-axis compared with the desired size. The reduction of the size along one direction and the resulting change in the aspect ratio will be further analyzed later.

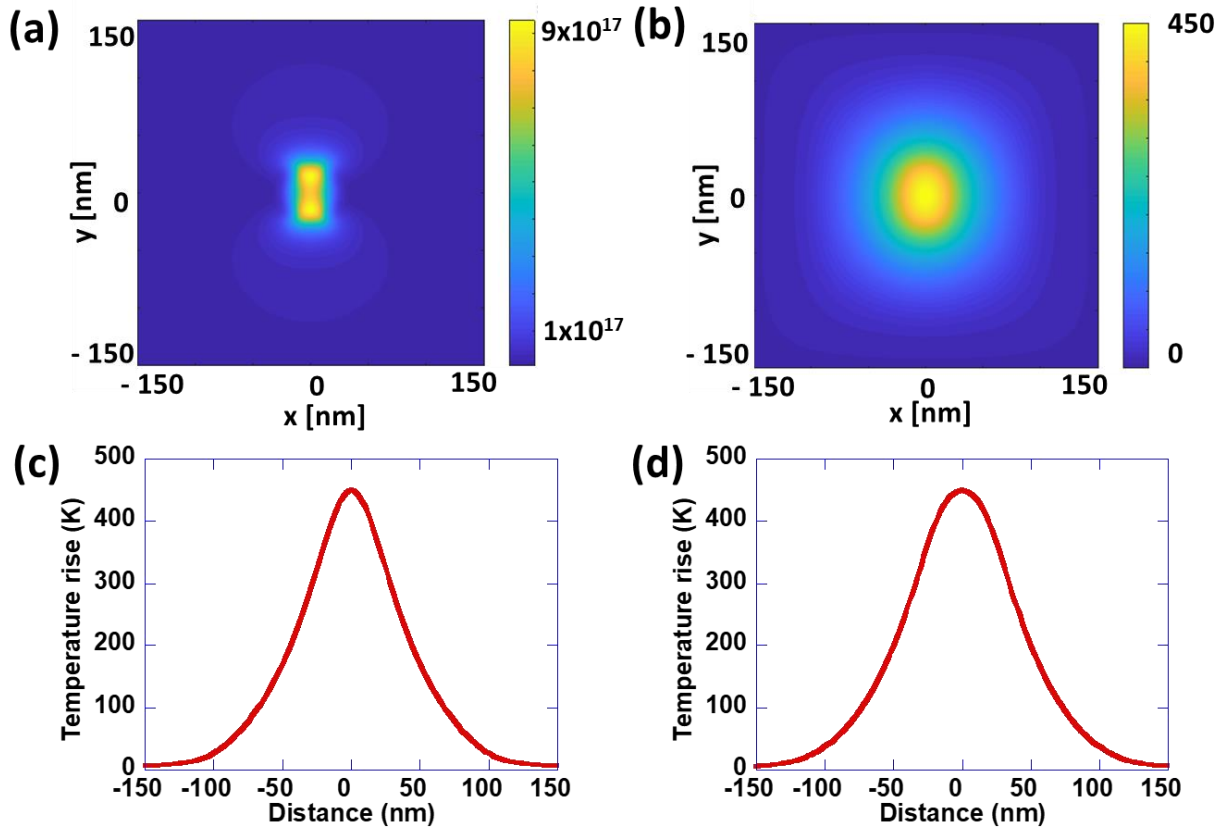


Figure 4.4 Thermal calculations with the obtained NFT design for the targeted heated spot of $30 \text{ nm} \times 60 \text{ nm}$ (a) Volumetric heat generation (W/m^3) in the recording medium with the obtained NFT design. (b) Scaled temperature rise (K) of recording medium with the obtained NFT design. (c) Temperature rise along the x – axis in Figure 4.4b. (d) Temperature rise along y – axis in Figure 4.4b.

4.4 Generating smallest heated spot in the recording medium

In order to find the smallest heated spot in the recording medium, we performed topology optimization of NFTs to achieve rectangular heated spot size of 30 nm x 60 nm, 25 nm x 50 nm, 20 nm x 40 nm, 15 nm x 30 nm, 10 nm x 20 nm, and 8 nm x 16 nm. The obtained NFT designs and the corresponding scaled temperature rises in the recording medium are shown in Figure 4.5. The heated spot sizes at 20 K and 50 K below the maximum temperature rise of 450 K and the required laser power for each design are summarized in Table 4-1. The gradients along both the axes at a temperature rise of 430 K and 400 K are also shown in Table 4-1. We find that the minimum spot size is about ~ 14 nm x 17 nm at 20 K below the maximum temperature, and is about 23 nm x 29 nm at 50 K below the maximum temperature despite the targeted sizes of 15 nm x 30 nm, 10 nm x 20 nm, and 8 nm x 16 nm. This indicates the minimum spot size that can be achieved. On the other hand, the achieved aspect ratio at minimum spot size is less than 2.

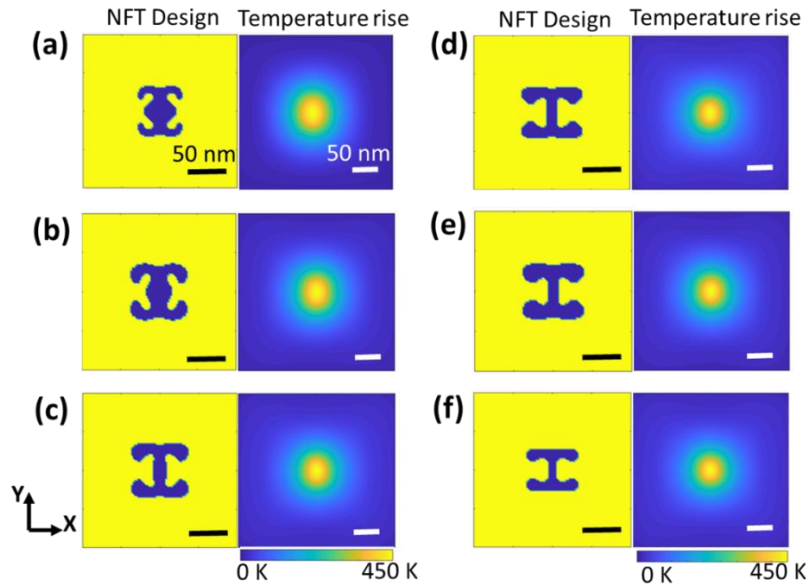


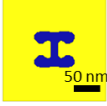




Figure 4.5 Generating smaller heated spot in the recording medium, with different targeted heated spot size of (a) 30 nm x 60 nm, (b) 25 nm x 50 nm, (c) 20 nm x 40 nm, (d) 15 nm x 30 nm, (e) 10 nm x 20 nm, and (f) 8 nm x 16 nm. The obtained designs of NFTs are shown on the left and the scaled temperature rises in the recording medium are shown on the right for each case. All scale bars are 50 nm.

Table 4-1 Heated spot size and gradients along both the axes at 430 K and 400 K, with different rectangular targeted heated spot size, and the corresponding power required for peak temperature rise of 450 K

Target Heat spot size (nm x nm)	Area (nm \times nm)		Gradient (K/nm)				Power (mW)
			X - axis	Y - axis	X - axis	Y - axis	
	At 430 K	At 400 K	At 430 K	At 400 K	At 430 K	At 400 K	
30 x 60	17.4 x 24.7	28.6 x 38.2	4.5	3.6	6.4	5.4	3.2
25 x 50	16.5 x 22.6	27.0 x 35.4	5.0	3.5	6.5	5.5	6.6
20 x 40	14.5 x 19.4	24.2 x 31.4	5.1	3.7	7.6	5.8	8.8
15 x 30	14.0 x 18.4	23.5 x 29.8	5.2	4.1	7.0	6.3	10.2
10 x 20	14.0 x 17.7	23.6 x 29.0	5.1	4.3	6.9	6.5	7.4
8 x 16	13.7 x 17.0	23.0 x 27.6	5.5	4.8	7.1	6.5	9.3

An obvious observation is that the geometries of NFT obtained by the topology optimization are intricate. We study the effect of the curvatures of the NFT geometry obtained with a targeted heated spot size of 10 nm x 20 nm, by performing direct calculations by modifying/removing (some of) the curvatures in NFT. Table 4-2 shows the modified NFTs and the resulting size of the heated spot at 430 K and 400 K. We observe that the heated spot size is smallest from the inverse designed NFT.

Table 4-2 The effect of curvature in NFT. All scale bars are 50 nm.

Case	Area (nm \times nm)	
	At 430 K	At 400 K
	14.0 \times 17.7	23.6 \times 29.0
	15.0 \times 18.7	25.1 \times 30.4
	15.3 \times 18.8	25.5 \times 30.3
	15.7 \times 19.3	26.3 \times 31.1
	15.7 \times 19.3	26.3 \times 31.2

4.5 Generating heated spot with higher aspect ratio

As discussed earlier when the targeted heated spot size is small, the obtained heated spot has an aspect ratio less than 2. Here we investigate if we can achieve an aspect ratio ~ 2 by increasing the targeted aspect ratio. We performed topology optimization for targeted heated spot size of 10 nm \times 30 nm, 10 nm \times 40 nm, 10 nm \times 60 nm, 10 nm \times 80 nm, and 10 nm \times 100 nm. The obtained NFT designs and the corresponding temperature rises in the recording medium are shown in Figure 4.6. We can see that the aspect ratio of obtained heated spot size increases with the increase of the targeted aspect ratio. The heated spot sizes at 20 K and 50 K below the maximum temperature rise of 450 K and the required laser power for each design are shown in Table 4-3. The gradients along both the axes at a temperature rise of 430 K and 400 K are also shown in Table

4-3. It is seen that with the targeted heat spot size of 10 nm x 80 nm and 10 nm x 100 nm, an aspect ratio ~ 2 can be obtained in the recording medium.

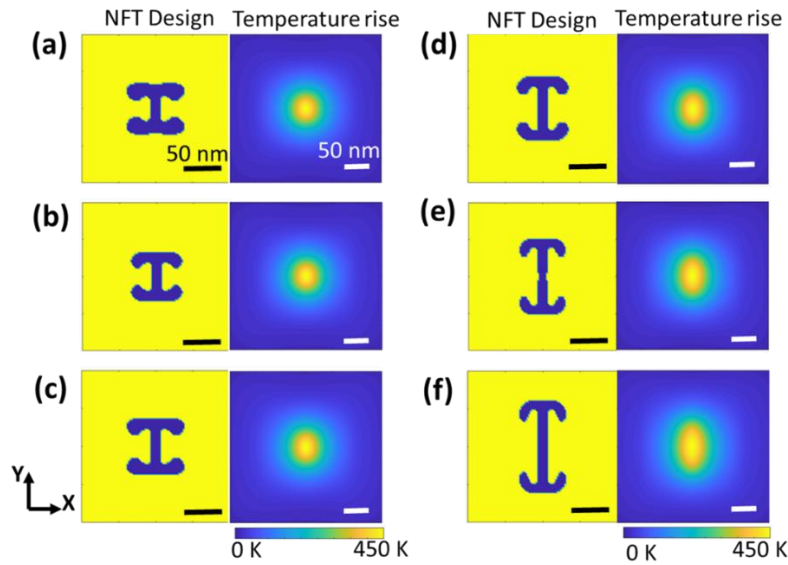


Figure 4.6 Generating high aspect ratio heated spot in the recording medium, with different targeted heated spot size of (a) 10 nm x 20 nm, (b) 10 nm x 30 nm, (c) 10 nm x 40 nm, (d) 10 nm x 60 nm, (e) 10 nm x 80 nm, and (f) 10 nm x 100 nm. The obtained designs of NFT are shown on the left and the scaled temperature rise in the recording medium are shown on the right for each case. All scale bars are 50 nm.

Table 4-3 Heated spot size and gradients along both the axes at 430 K and 400 K, with different targeted heated spot size for generating high aspect ratio heated spot in the recording medium, and the corresponding power required for peak temperature rise of 450 K.

Target heat spot size (nm x nm)	Area (nmxnm)		Gradient (K/nm)				Power (mW)
			X -axis	Y - axis	X - axis	Y - axis	
	At 430 K	At 400 K	At 430 K		At 400 K		
10 x 20	14.0 x 17.7	23.6 x 29.0	5.1	4.3	6.9	6.5	7.4
10 x 30	14.1 x 18.4	23.5 x 29.8	5.6	4.1	7.0	6.3	8.0
10 x 40	14.4 x 20.3	24.1 x 32.6	5.0	4.2	7.3	6.1	8.7
10 x 60	14.6 x 22.5	24.4 x 36.2	5.0	3.4	7.2	5.5	8.2
10 x 80	14.9 x 26.8	25.0 x 42.9	4.7	2.8	6.9	4.5	7.8
10 x 100	15.9 x 34.9	26.2 x 54.4	4.3	2.3	6.6	3.8	8.4

Next, we improve our HAMR model by considering waveguide, writepole and moving recording medium. And study the effect on the spot size in the recording with the obtained NFT designs using a simplified model.

4.6 Effect of waveguide in HAMR model

Waveguide is used to couple the light to NFT and we study the effect of waveguide on the spot size in the recording medium. We consider a dielectric waveguide made of Ta_2O_5 with SiO_2 cladding as in [28]. Schematic of the waveguide is shown in Figure 4.7a. Rectangular waveguide of 300 nm x 600 nm is studied [28] with a length of 1600 nm. The waveguide is separated from NFT with 36 nm thick SiO_2 . A Gaussian beam of diameter 800 nm is considered with an incident power of 1 mW. Light polarization is considered along the short axis of the waveguide [28]. Simulation domain is 2400 nm x 2700 nm. The outer dimension of the NFT is 500 nm x 500 nm. The optical properties of Ta_2O_5 are taken from [134]. Here the effect of waveguide with obtained NFT design for a targeted heat spot of 10 nm x 80 nm (Figure 4.6e) is studied. Electromagnetic field calculations are performed using ANSYS and temperature rise in the recording medium is calculated by equation (4.1), using the electric field at midplane of FePt. Electric field distribution at the exit plane of the waveguide and at the exit of the waveguide is shown in Figure 4.7b (i) and (ii) respectively.

The scaled temperature rise in the recording medium is shown in Figure 4.8. Waveguide with dimensions 600 nm x 600 nm is also studied with obtained NFT design for a targeted heat spot of 10 nm x 80 nm. Electric field distribution at the exit plane of waveguide and temperature rise in the recording medium are shown in Figure 4.9a and Figure 4.9b respectively for 600 nm x 600 nm waveguide. We observe that the waveguide supports different mode where the maximum

electric field is not at the center. Temperature hot spot area and gradient along both axes at 430 K, and the power required to generate the hot spot with the waveguides is shown in Table 4-4. Table 4-4 also compares with the previous simplified model (Figure 4.1), of without a waveguide. We observe that the spot size and gradients are not affected with waveguide. The power required with 600 nm x 600 nm waveguide is ~ three time more than with the 300 nm x 600 nm waveguide. This is due to better coupling of light to the NFT as seen by the electric field distribution. Table 4-5 compares the hot spot size and gradients at 400 K.

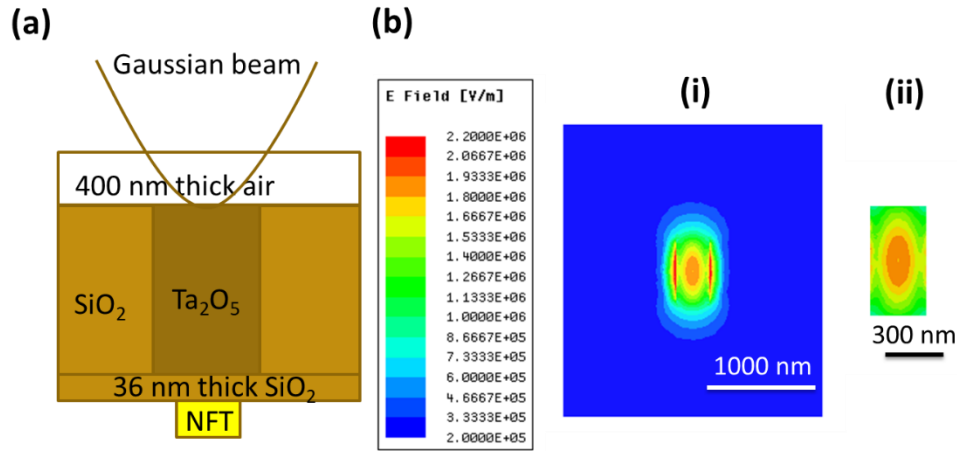


Figure 4.7 Adding 600 nm x 300 nm Ta₂O₅ waveguide to the obtained design for a targeted heat spot of 10 nm x 80 nm (a) Schematic (b) Electric field distribution (i) at the exit plane of waveguide (ii) at the exit of the waveguide.

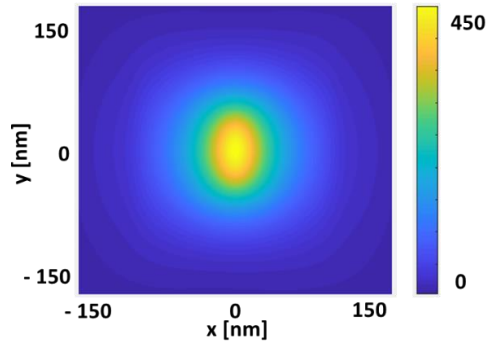


Figure 4.8 Temperature rise (K) in the recording medium with 600 nm x 300 nm Ta₂O₅ waveguide

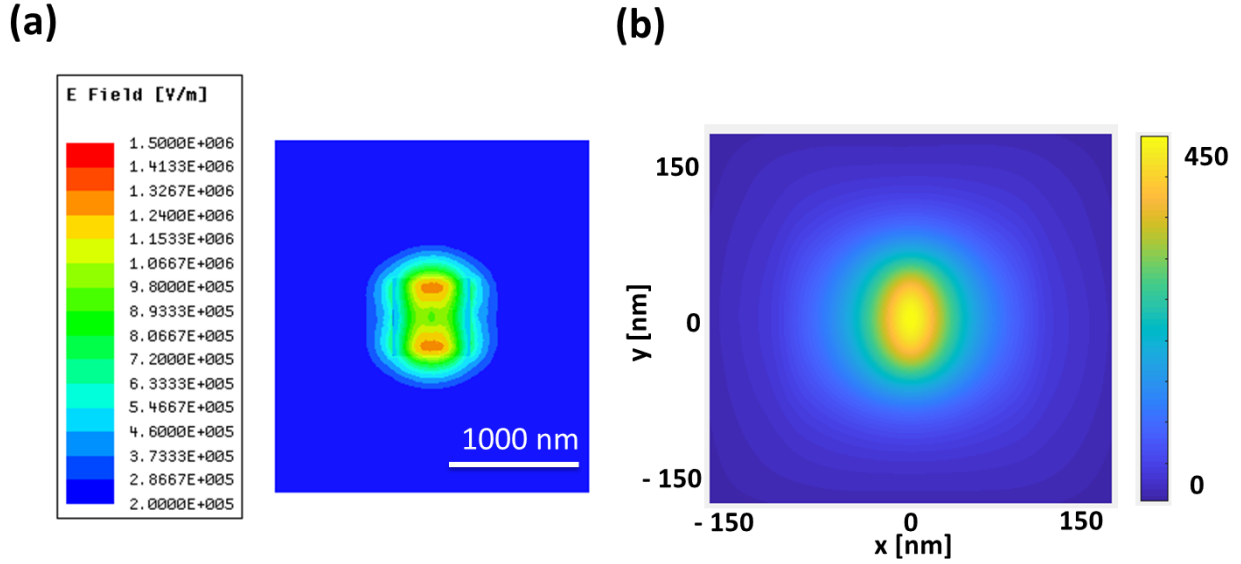


Figure 4.9 Adding 600 nm x 600 nm Ta₂O₅ waveguide to the obtained design for a targeted heat spot of 10 nm x 80 nm (a) Electric field distribution at the exit plane of waveguide (ii) Temperature rise (K) in the recording medium.

Table 4-4 Temperature hot spot area and gradient along both axes at 430 K, and the power required to generate the hot spot with and without a waveguide.

Case	xsize (nm)	ysize (nm)	x-slope (K/nm)	y-slope (K/nm)	Power (mW)
Without waveguide, plane beam input	14.9	26.8	4.7	2.8	7.8
300 nm x 600 nm waveguide, Gaussian beam input	14.9	26.7	4.8	2.8	3.7
600 nm x 600 nm waveguide, Gaussian beam input	14.8	27.9	4.8	2.7	12.4

Table 4-5 Temperature hot spot area and gradient along both axes at 400 K, with and without a waveguide.

Case	xsize (nm)	ysize (nm)	x-slope (K/nm)	y-slope (K/nm)
Without waveguide, plane beam input	25.0	42.9	6.9	4.5
300 nm x 600 nm waveguide, Gaussian beam input	24.7	42.8	7.0	4.4
600 nm x 600 nm waveguide, Gaussian beam input	24.9	44.0	7.0	4.7

Hence adding the waveguide, did not affect the spot size and gradient at a temperature rise of 430 K and 400 K.

4.7 Effect of write pole in HAMR model

Write pole is used in HAMR to provide the magnetic field. We consider a CoFe write pole [28]. Here the effect of write pole with the obtained NFT design for a targeted heat spot of 10 nm x 80 nm (Figure 4.6e) is studied. Electromagnetic field calculations are performed using ANSYS and temperature rise in the recording medium is calculated by equation (4.1), using the electric field at midplane of FePt. The optical properties of write pole are taken from [134]. The write pole is considered to be 680 nm wide and pole gap is ~ 30 nm (lateral distance between the hotspot in the recording medium and write pole) [28]. We used 300 nm x 600 nm Ta₂O₅ waveguide with SiO₂ cladding as before. Schematic of HAMR model with write pole is shown in Figure 4.10a. NFT is shown in yellow and write pole is shown in red. The top view of write pole and NFT is

shown in Figure 4.10b. Write pole is till $x = -30$ nm, to have the gap of ~ 30 nm to the hot spot. Hence some part of NFT is removed as compared to Figure 4.6e. These calculations are to study the effect of the spot size in the recording medium due to write pole. We considered CoFe as a non-magnetic material in the simulations.

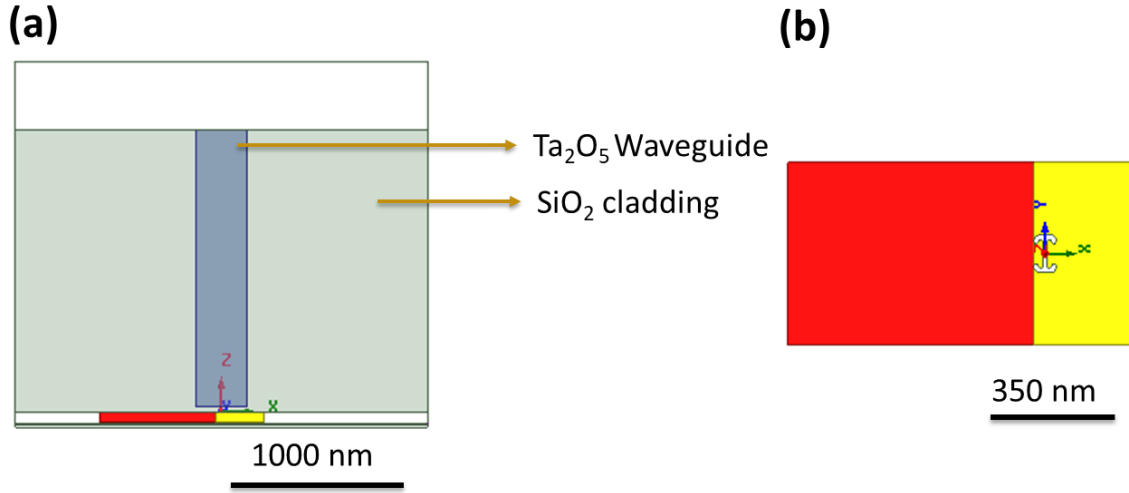


Figure 4.10 Adding the write pole to the obtained design for a targeted heat spot of 10 nm x 80 nm (a) Schematic (b) Top view showing CoFe write pole (red) and NFT (yellow).

The electric field distribution at the center plane of FePt recording medium with write pole is shown in Figure 4.11a. The zoomed in view of the electric field distribution is shown in Figure 4.11b. We observe a slight asymmetry in the electric field distribution by adding the write pole. The scaled temperature rise in the recording medium without and with write pole is shown in Figure 4.12. Temperature hot spot area and gradient along both axes at 430 K and 400 K, and the power required to generate the hot spot with and without the write pole is shown in Table 4-6. Table 4-6 also compares effect of the write pole with obtained NFT designs for a targeted heat spot of 10 nm x 20 nm and 10 nm x 100 nm. We observe that spot size has increased slightly with write pole. Hence adding the write pole, did not significantly affect the spot size and gradients at a temperature rise of 430 K and 400 K.

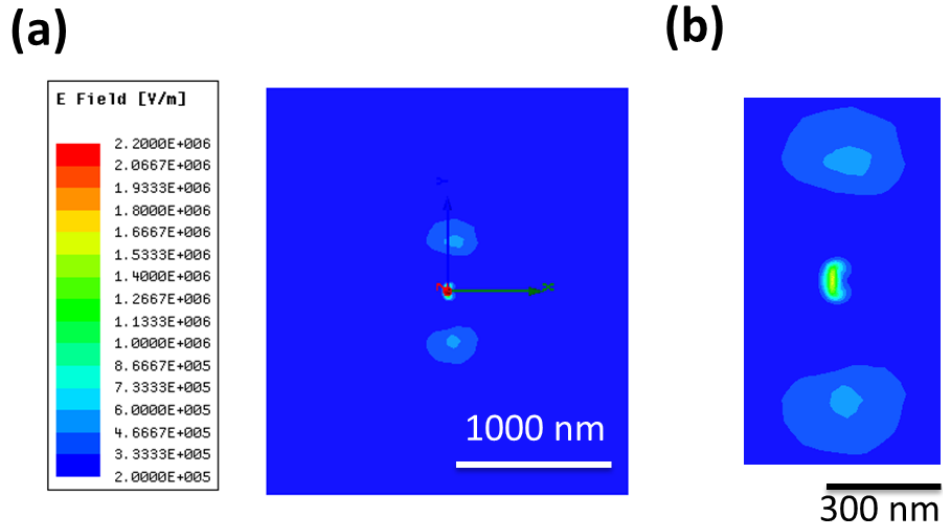


Figure 4.11 Adding CoFe write pole to the obtained design with a targeted heat spot of 10 nm x 80 nm (a) Electric field distribution at the center plane of FePt. (b) Zoomed in view of electric field shown in Figure 4.11a

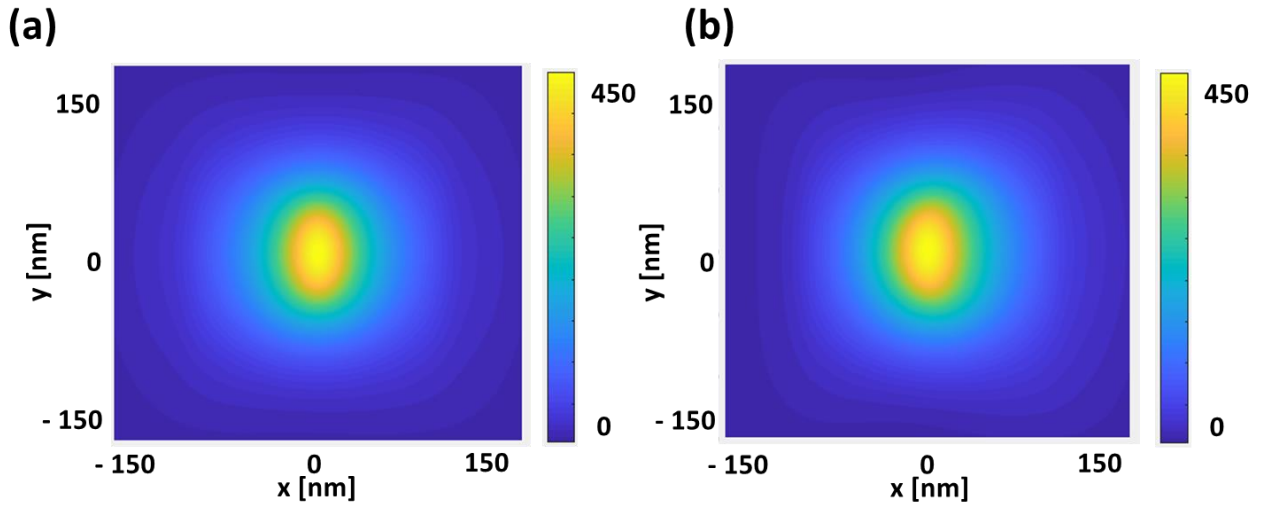


Figure 4.12 Temperature rise (K) in the recording medium (a) Without write pole (b) With write pole

Table 4-6 Temperature hot spot area and gradient along both axes at 430 K and 400 K, and the power required to generate the hot spot with and without the write pole

Without writepole 430 K	xsize (nm)	ysize (nm)	x-slope (K/nm)	y-slope (K/nm)	Power (mW)	Without writepole 400 K	xsize (nm)	ysize (nm)	x-slope (K/nm)	y-slope (K/nm)
10 x 20 nm	13.6	17.5	5.3	4.5	3.6	10 x 20 nm	23.1	28.6	7.0	6.7
10 x 80 nm	14.8	26.7	4.8	2.8	3.7	10 x 80 nm	24.7	42.8	7.0	4.4
10 x 100 nm	15.5	34.0	4.4	2.3	4.1	10 x 100 nm	25.9	53.8	6.6	3.8

With writepole 430 K	xsize (nm)	ysize (nm)	x-slope (K/nm)	y-slope (K/nm)	Power (mW)	With writepole 400 K	xsize (nm)	ysize (nm)	x-slope (K/nm)	y-slope (K/nm)
10 x 20 nm	15.2	20.0	5.1	3.6	3.3	10 x 20 nm	25.6	32.2	6.4	6.0
10 x 80 nm	15.5	25.3	4.8	2.8	3.6	10 x 80 nm	26.0	42.2	6.5	4.4
10 x 100 nm	16.4	36	4.9	2.4	4.0	10 x 100 nm	27.2	56.5	6.1	3.7

4.8 Effect of moving recording medium

The recording medium moves with a velocity of 10 m/s. Here we study the effect of the moving medium on the hot spot size of the recording medium. The effect of moving medium with obtained NFT design for a targeted heat spot of 10 nm x 100 nm (Figure 4.6f) is studied. We simplify it as a two-dimensional thermal problem. We consider HAMR head is moving relative to the recording medium and have a spatial time varying volumetric heat generation in the recording medium. Explicit code is written in MATLAB for 2D transient problem with a spatial-time varying volumetric heat generation, with and without effective heat transfer coefficient h . Recording medium of 300 nm x 300 nm with a discretization of 2 nm ($dx = dy = 2$ nm) is considered. To have the stability criteria for explicit method, $dt = 0.00125$ ns is considered, which gives $F_0 = 0.146 <$

0.25. The governing equation is given in equation (4.7), where \dot{q} is varying with space and time (for moving medium). We first studied with a simplified model of without h (effective heat transfer coefficient) for heat loss.

$$\frac{\delta^2 T}{\delta x^2} + \frac{\delta^2 T}{\delta y^2} + \frac{\dot{q}}{k} = \frac{1}{\alpha} \frac{\partial T}{\partial t} \quad (4.7)$$

The incident power is such that the maximum temperature rise with stationary medium at 1 ns is ~ 450 K. Temperature of the stationary recording medium at 1 ns and 2 ns is shown in Figure 4.13. The maximum temperature at 2 ns is ~ 971 K due to longer heating of the recording medium.

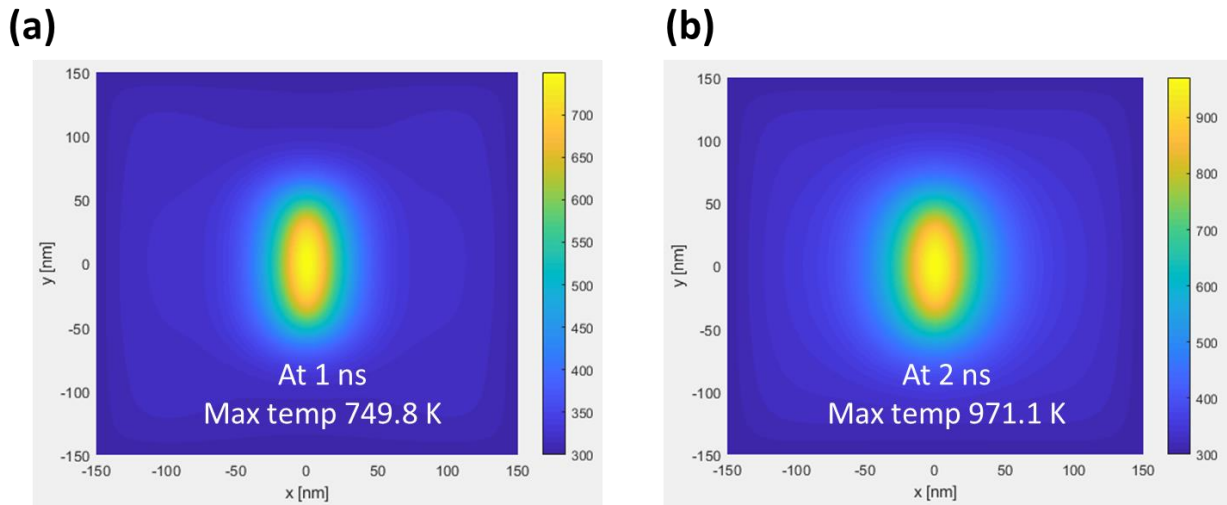


Figure 4.13 Temperature (K) of the stationary recording medium (a) At 1 ns (b) At 2 ns.

The temperature of the recording medium which is moving with a horizontal velocity of 10 m/s is shown in Figure 4.14. We considered the same incident power as of the stationary medium. From the temperature distribution, we observe that the hot spot is moving with time and the temperature distribution is asymmetric. We observe that the maximum temperature with moving medium at the same time is lower as compared to the stationary medium.

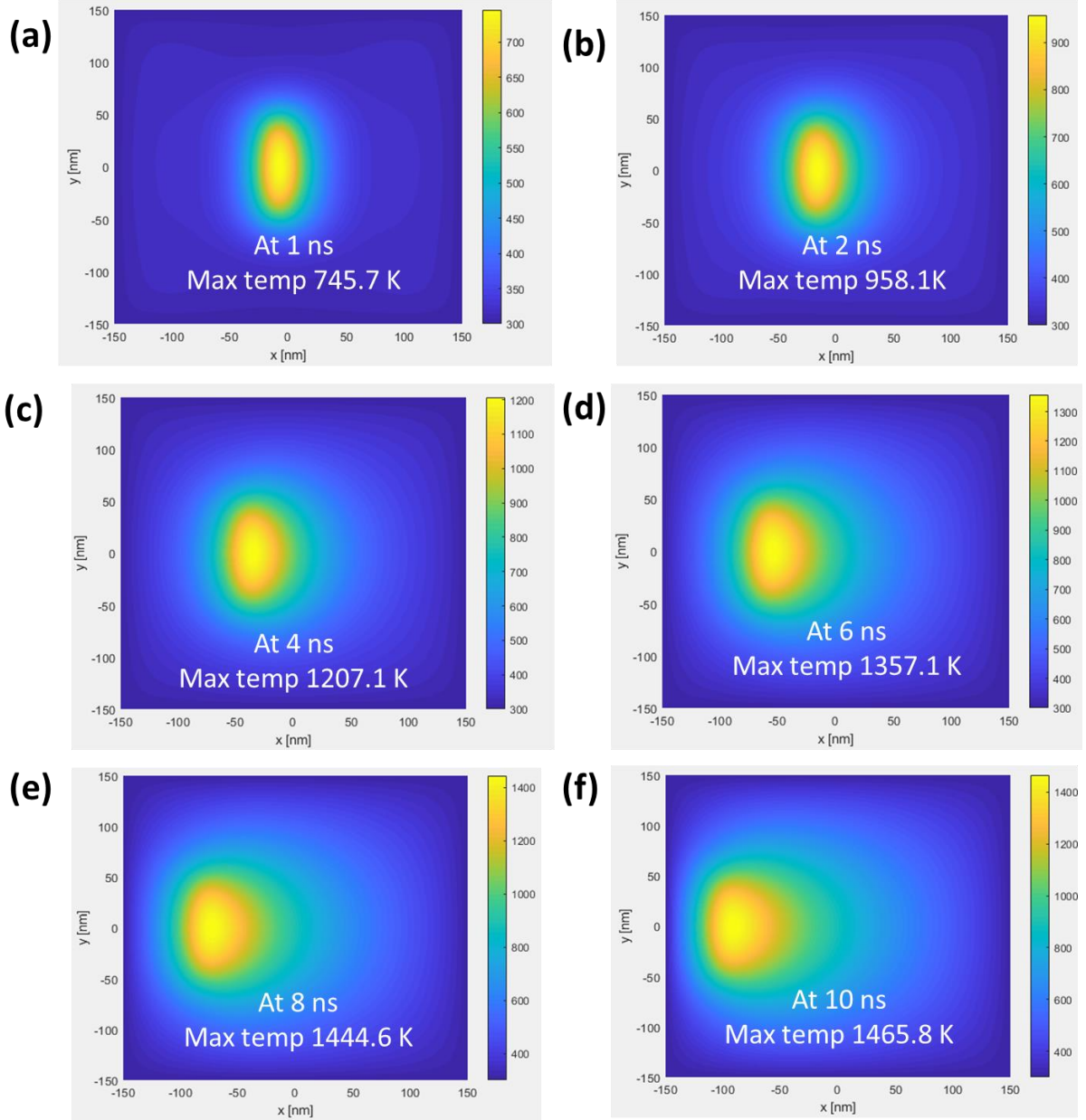


Figure 4.14 Temperature (K) of recording medium moving with a horizontal velocity of 10 m/s (a) At 1 ns (b) At 2 ns (c) 4 ns (d) 6 ns (e) 8 ns (f) 10 ns.

The temperature profile along the horizontal line is plotted at various times and is shown in Figure 4.15a. As expected, maximum temperature location is delayed with respect to the displacement, i.e., at 10 ns, peak temperature is not at -100 nm. As observed from Figure 4.15a, limited simulation domain has an affect on the temperature data at 12 ns. The temperature profiles

are displaced for better comparison and are shown in Figure 4.15b, i.e., temperature profiles at 4 ns, 6 ns and 8 ns are moved by 60 nm, 40 nm, and 20 nm to compare with the temperature profile at 10 ns. The temperature curves in Figure 4.15b is normalized to maximum temperature of 750 K and is shown in Figure 4.15c. Although the gradients are significantly different on either side (leading and trailing edge) at lower temperature of the medium but are similar closer to peak temperature.

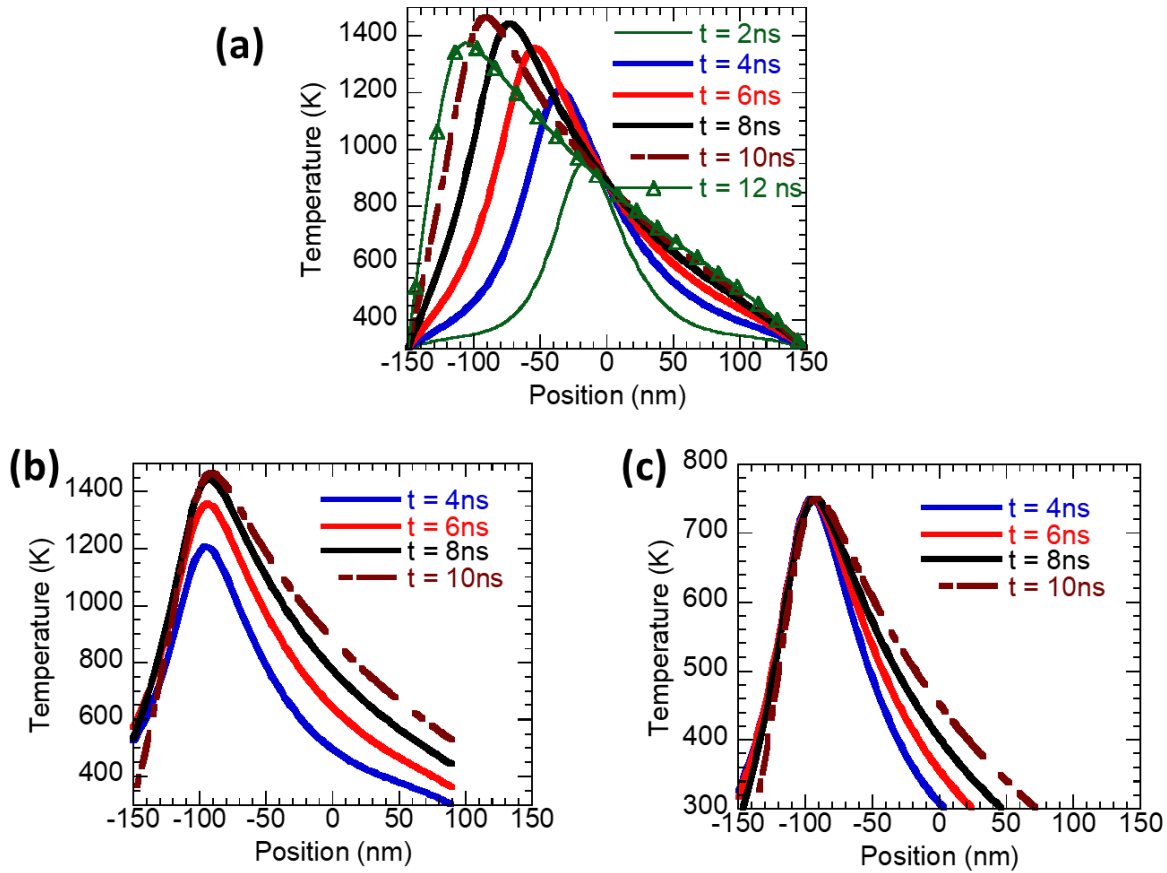


Figure 4.15 Temperature profile of the recording medium (a) Actual temperature (b) Displacing the temperature profiles by the displacement (c) Normalizing the curves in Figure 4.15b.

Next, we consider effective heat transfer coefficient h for the heat loss in the recording medium and the governing equation is shown in equation (4.8), where a is the thickness of FePt film, 10 nm.

$$\frac{\delta^2 T}{\delta x^2} + \frac{\delta^2 T}{\delta y^2} + \frac{\dot{q} - (h/a)(T - T_\infty)}{k} = \frac{1}{\alpha} \frac{\partial T}{\partial t} \quad (4.8)$$

The effective h can be estimated from a semi-infinite model with a constant surface temperature T_s losing heat with a heat transfer coefficient h to an ambient of T_∞ [143]. So, the h value depends on the time t and thermal properties as shown in equation (4.9).

$$h = \frac{k}{\text{sqrt}(\pi \alpha t)} \quad (4.9)$$

In calculating effective h , properties of heat sink used in HAMR is considered [140] and t is estimated from the spot size and velocity of the medium. The effective h is estimated as 2×10^8 W/m²K. The incident power is same as before, such that the maximum temperature rise at 1 ns is ~ 450 K with stationary medium, and without h . Temperature of the stationary recording medium with h , at 1 ns and 2 ns is shown in Figure 4.16. We can compare the temperature of the stationary medium without h in Figure 4.13. The maximum temperature is lower compared to the case of without h as expected. The heat spot size at 430 K temperature rise is 8.5 nm x 40.6 nm compared to without h of 11.4 nm x 38.7 nm. And the gradients at 430 K temperature rise are 10.6 K/nm and 2.5 K/nm along x and y directions respectively. The gradients at 430 K without h are 5.9 K/nm and 2.4 K/nm along x and y directions respectively. So, with h we observe smaller heat spot size and higher gradients along the moving direction (x - direction). The slight discrepancy in values of temperature hot spot size and gradients for without h case mentioned here and in Table 4-3 is due

sto the two different methods used for thermal calculation. One is the explicit method and the other is using the Green's function for previous calculations. (Table 4-3)

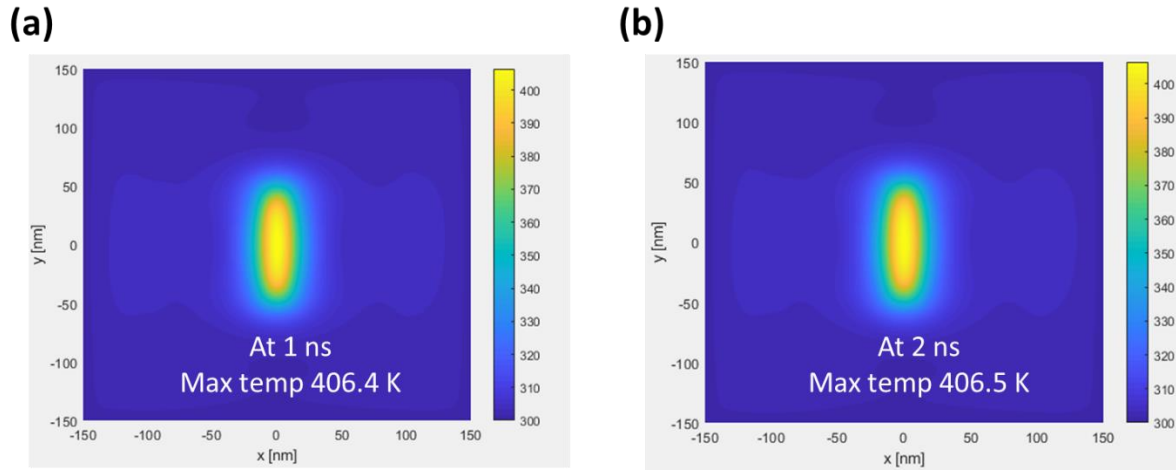


Figure 4.16 Temperature (K) of the stationary recording medium with h (a) At 1 ns (b) At 2 ns.

The temperature of the recording medium which is moving with a horizontal velocity of 10 m/s, with h, is shown in Figure 4.17. We considered the same incident power as of the stationary medium. We observe that the maximum temperature is not increasing with time as compared to moving medium without h in Figure 4.14. This is because of the dissipation of incident energy by effective h. The maximum temperature with moving medium at the same time is almost same as to the stationary medium. In contrast there is a significant difference in the case of without h as shown in Figure 4.13 and Figure 4.14.

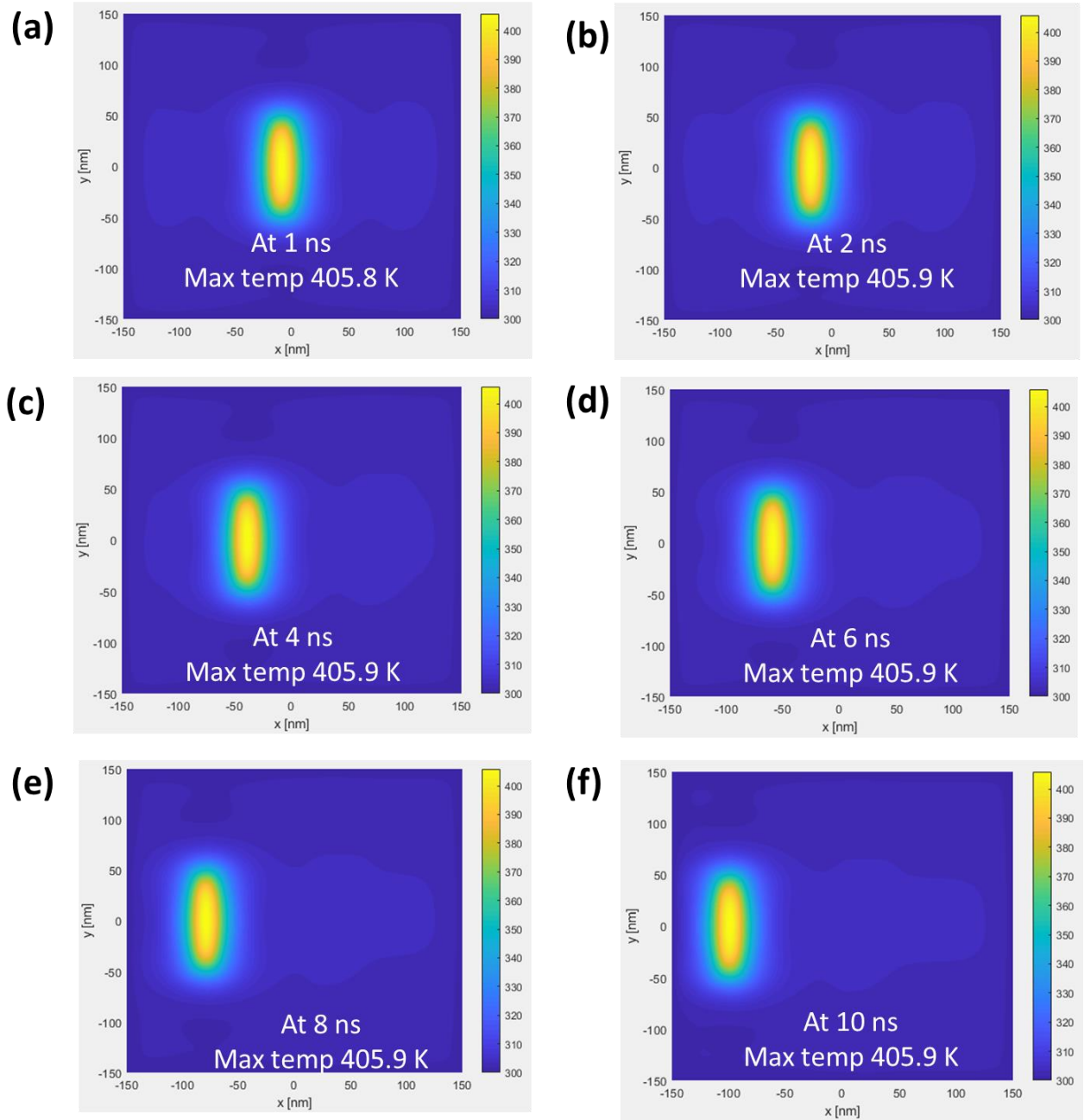


Figure 4.17 Temperature (K) of the recording medium with a horizontal velocity of 10 m/s, with
h (a) At 1 ns (b) At 2 ns (c) 4 ns (d) 6 ns (e) 8 ns (f) 10 ns

The temperature of moving and stationary recording medium is compared in Figure 4.18.

Figure 4.18a and Figure 4.18b shows the temperature at 6 ns for moving and stationary recording

medium respectively. Temperature profiles along x and y axes at 6 ns are shown in Figure 4.18c and Figure 4.18d respectively for moving and stationary medium.

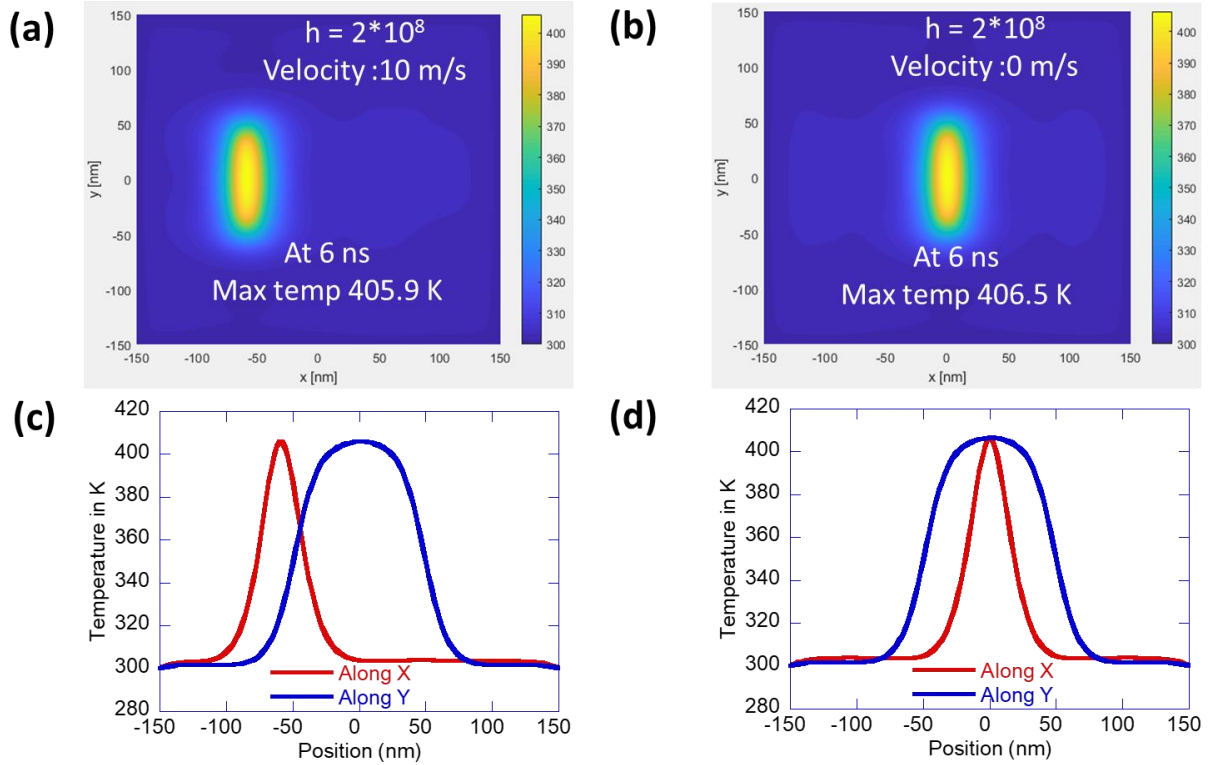


Figure 4.18 Comparing the temperature of moving and stationary recording medium with h . (a) Moving medium (b) Stationary medium (c) Temperature along the x and y axes for moving medium (d) Temperature along the x and y axes for stationary medium.

The temperature hot spot size and gradients for scaled temperature rise at 430 K and 400 K along both x and y axes, for $h = 2 \times 10^8$ W/m²K are shown in Table 4-7. Table 4-7 also shows the gradient on either side of the maximum temperature. We observe the slight asymmetry in the gradients at lower temperature similar to in Figure 4.15. Table 4-8 shows the temperature hot spot size and gradients for scaled temperature rise at 430 K and 400 K along both x and y axes for $h = 2 \times 10^7$ W/m²K.

Table 4-7 The temperature hot spot size and gradients for scaled temperature rise at 430 K and 400 K along both x and y axes, for $h = 2 \times 10^8 \text{ W/m}^2\text{K}$

X axis

	Gradient (K/nm)				Spot size (nm)	
Case	neg X	pos X	neg X	pos X		
	At 430 K		At 400 K		At 430 K	At 400 K
Moving	8.6	9.0	14.7	12.1	8.4	13.8
Stationary	10.5	10.6	13.5	13.5	8.3	13.6

Y axis

	Gradient (K/nm)				Spot size (nm)	
Case	neg Y	pos Y	neg Y	pos Y		
	At 430 K		At 400 K		At 430 K	At 400 K
Moving	2.2	2.5	5.2	5.0	43.2	61.0
Stationary	2.2	2.5	5.2	5.0	43.1	61.0

Table 4-8 The temperature hot spot size and gradients for scaled temperature rise at 430 K and 400 K along both x and y axes, for $h = 2 \times 10^7 \text{ W/m}^2\text{K}$

X axis

	Gradient (K/nm)				Spot size (nm)	
Case	neg X	pos X	neg X	pos X		
	At 430 K		At 400 K		At 430 K	At 400 K
Moving	6.1	5.2	9.1	7.9	12.9	21.1
Stationary	6.5	6.5	8.8	8.8	12.6	20.7

Y axis

	Gradient (K/nm)				Spot size (nm)	
Case	neg Y	pos Y	neg Y	pos Y		
	At 430 K		At 400 K		At 430 K	At 400 K
Moving	2.4	2.3	4.1	4.1	34.5	53.3
Stationary	2.4	2.3	4.1	4.0	34.8	53.7

Hence the moving medium did not affect the spot size and gradients at a temperature rise of 430 K and 400 K.

4.9 Summary

In summary, we demonstrate using an inverse design process to design NFTs to obtain targeted heated spot size in the recording medium for heat-assisted magnetic recording. Inverse thermal calculation is first performed to obtain the desired volumetric heat generation (electric field) in the recording medium. Then the inverse electromagnetic field calculation is performed to obtain an NFT that produces the desired electric field. NFT designs for generating a smallest heated spot is carried out, which is found to be $\sim 14 \text{ nm} \times 17 \text{ nm}$ at 430 K, or 20 K below the peak temperature. It is also shown that the obtained NFTs are able to produce a smaller heated spot compared with NFTs for which the intricate curvatures are removed. A desired aspect ratio of ~ 2 can be obtained by initially selecting a higher targeted aspect ratio. The effect of adding waveguide, write pole to the HAMR model and moving medium is studied, and did not significantly affect the spot size and gradients at a temperature rise of 430 K and 400 K. This work indicates that inverse design can be used to obtain NFTs with desired requirements, and to produce NFT structures that are not intuitively considered, thus possibly open up more design options of NFT.

5. SUMMARY AND FUTURE WORK

5.1 Summary

In this thesis, we study the applications of surface plasmons in the emerging two-dimensional materials black phosphorus, bismuth telluride selenide, and for heat assisted magnetic recording. In the first work, we demonstrated enhanced photosensitivity and polarization selectivity of black phosphorus photodetectors at 1550 nm wavelength, using resonant plasmonic structures. In the first design using bowtie antennas, we obtained an enhancement of photo response. In the second design, polarization selectivity is obtained by using bowtie apertures. Enhanced photosensitivity and polarization selectivity at near infrared wavelengths will be useful in various applications including telecommunication, remote sensing, and infrared polarimetry imaging.

In the second work, we studied the distinct surface plasmons of the bulk and surface state of the topological insulator, $\text{Bi}_2\text{Te}_2\text{Se}$. The optical properties are studied and the bulk $\text{Bi}_2\text{Te}_2\text{Se}$ is plasmonic below the wavelength 650 nm. The propagating surface plasmons at the nanoslit are imaged using near-field scanning optical microscopy. The surface state plasmons are studied with a below band gap excitation of 10.6 μm wavelength and the surface plasmons from the bulk are studied with a visible wavelength of 633 nm. The surface state plasmon wavelength is 100 times shorter than the incident wavelength in sharp contrast to the plasmon wavelength of the bulk. The strong optical confinement of the surface state plasmons can be exploited for various applications including integrated optical circuits and subwavelength optical devices.

In the third work, we use topology optimization for an inverse design of NFT for a desired temperature profile of the recording medium in heat assisted magnetic recording. We first perform an inverse thermal calculation to obtain a required volumetric heat generation (electric field) in the

recording medium for achieving a desired temperature profile. Then the inverse electromagnetic field calculation is performed to obtain an NFT that produces the desired electric field using topology optimization. NFT designs for generating a smallest heated spot is carried out, which is found to be $\sim 14 \text{ nm} \times 17 \text{ nm}$ at 430 K, or 20 K below the peak temperature. We studied the effect of the intricate curvatures of the obtained NFTs and it is shown that the obtained NFTs are able to produce a smaller heated spot compared with NFTs for which the intricate curvatures are removed. A desired aspect ratio of ~ 2 in the heated spot can be obtained by initially selecting a higher targeted aspect ratio. We studied the effect of adding waveguide, write pole and moving medium to the HAMR model and found that it did not significantly affect the temperature hot spot size and gradients at 430 K and 400 K temperature rise. This work indicates that inverse design can be used to obtain NFTs with desired requirements, and to produce NFT structures that are not intuitively considered, thus possibly open up more design options of NFT.

5.2 Ongoing work

In the ongoing work, we are using machine learning to obtain the inverse design of NFT for a desired temperature profile. This work is in collaboration with Nick Winovich and Prof. Guang Lin. The process of obtaining the inverse design of NFT using topology optimization is computationally expensive. It takes few days to obtain each inverse design. We can use neural network as a surrogate model for the combined optical and thermal simulations. For doing this, we need to generate lot of data and train the neural network using 80% of the data and validate the network with remaining 20% of data. Once we have the neural network, getting a temperature distribution is significantly faster for a given NFT design. Then we can use optimization techniques to obtain the inverse design. So, this method would be significantly faster and more efficient but not necessarily perfect. But we can always check with finite element simulation to see if the final

obtained temperature distribution of neural network matches. We can use this method to find NFT design with better figures of merit, including high temperature gradients, efficient design. Also, our goal is to find a design which provides rectangular heated spot in the recording medium. Unfortunately, we could not find the design which provides rectangular heated spot (with high gradients) using topology optimization. The aim of the project is to find designs which can give closer to the desired rectangular heated spot.

We first generate 500 designs and do the forward calculations to train the neural network. The schematic of how the NFT designs is generated is shown in Figure 5.1. As shown in Figure 5.1a, we choose random points in the first quadrant where radial basis functions are generated. These basis functions can have different amplitude, standard deviation. These basis functions are added as shown in Figure 5.1b. A cut off value is chosen which decides the location of aperture as shown in Figure 5.1c. This gives us the aperture location in first quadrant as shown in Figure 5.1d. By performing the symmetry operations, we obtain the aperture region of NFT as shown in Figure 5.1e.

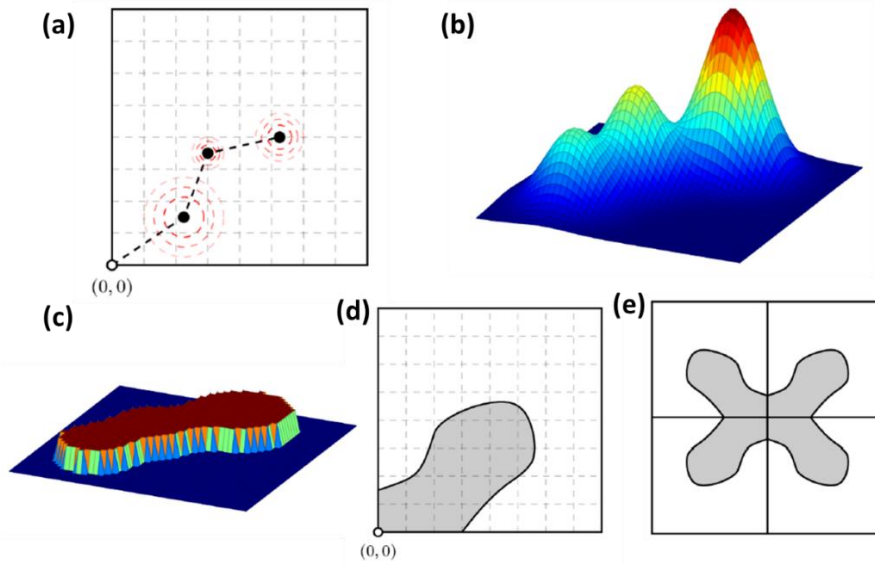


Figure 5.1 Schematic of generation of NFT designs (a) Choosing the random points for generation of radial basis function (b) Radial basis functions generated at these points are summed up. (c) Choosing the cutoff value decides the location of aperture. (d) Schematic of aperture in the first quadrant. (e) Schematic of the aperture of the design by performing symmetry operations.

By choosing different locations, amplitude, standard deviation of the radial basis functions, different NFT designs are generated. The design data of NFT (1s and 0s, where 0 is represented by aperture) is converted to STL file using MATLAB. The STL file is converted to STEP file using ANSYS Spaceclaim and the STEP file can be imported into ANSYS Electronics Desktop. Script is written to perform electromagnetic simulations in ANSYS Electronics Desktop automatically and obtain the electric field at the center plane of the recording medium. This electric field profile is used to calculate the temperature rise in the recording medium using an explicit method code in MATLAB. Once we have the direct calculations of NFT design and the corresponding temperature profile, we train the artificial neural network. Generation of the randomized NFT designs and training of neural network is done by Nick Winovich. The schematic of the neural network training procedure is shown in Figure 5.2. We have given design and the

corresponding temperature profile by finite element simulations. We update the weights of neural network by the loss, i.e., difference in the temperature profile predicted by current network and actual finite element simulations. We train the neural network using 80% of the data and validate with the remaining 20% of the data.

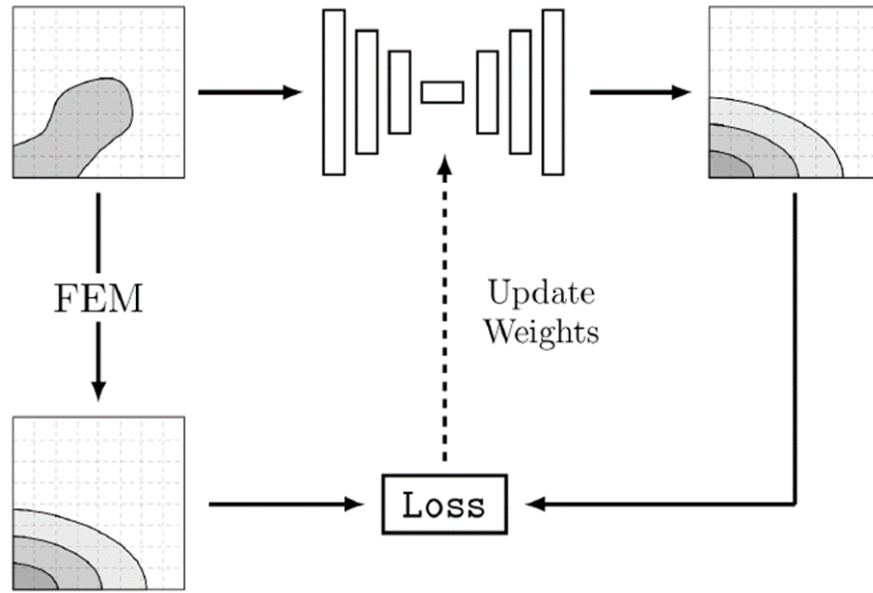


Figure 5.2 Schematic of the neural network training procedure.

Prior knowledge of having a high aspect ratio in the design to get an aspect ratio of 2 for the heated spot is used in generating the NFT designs. This will help in training the neural network faster and accurate in the desired design space. We used a plane wave of 10 mW in electromagnetic field calculations with a simplified HAMR model (Figure 4.1). 2D thermal calculations are performed with an effective $h = 2 \times 10^8 \text{ W/m}^2\text{K}$. Figure 5.3 shows the forward calculation for one case. Figure 5.3a shows the NFT design and Figure 5.3b shows the corresponding temperature rise in the recording medium.

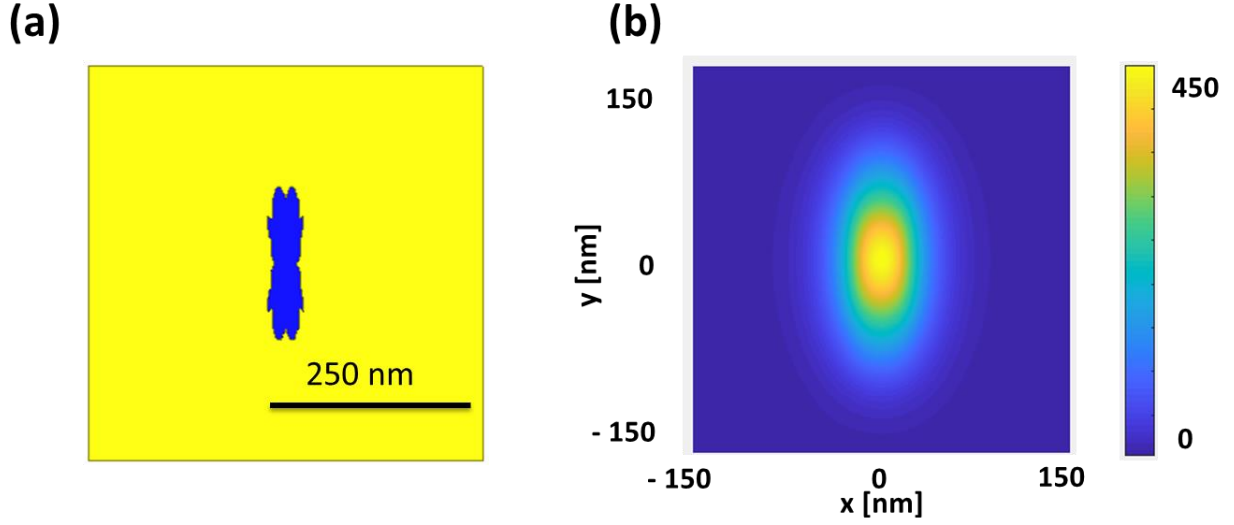


Figure 5.3 Forward calculation for one case (a) NFT design, where blue region indicates the aperture. (b) Temperature rise (K) in the recording medium for NFT design shown in Figure 5.3a.

Temperature spot size and gradients at 430 K along both axes are shown in Figure 5.4 for first ~ 100 forward calculations. Figure 5.4 also shows the aspect ratio and the factor, which is defined as power required/10 mW to have a peak temperature rise of 450 K in the recording medium. After doing 500 simulations, neural network is trained. The preliminary results of neural network prediction of temperature profile for the validation data is shown for two cases (a) and (b) in Figure 5.5. Figure 5.5(i) shows the prediction from the neural network and the actual solution. Figure 5.5(ii) shows the error in prediction by neural network. So, we see a reasonably good prediction from neural network for some cases. The ongoing work is focused on improving the neural network by training more data. Our goal is to find a design which provides rectangular heated spot in the recording medium with high gradients.

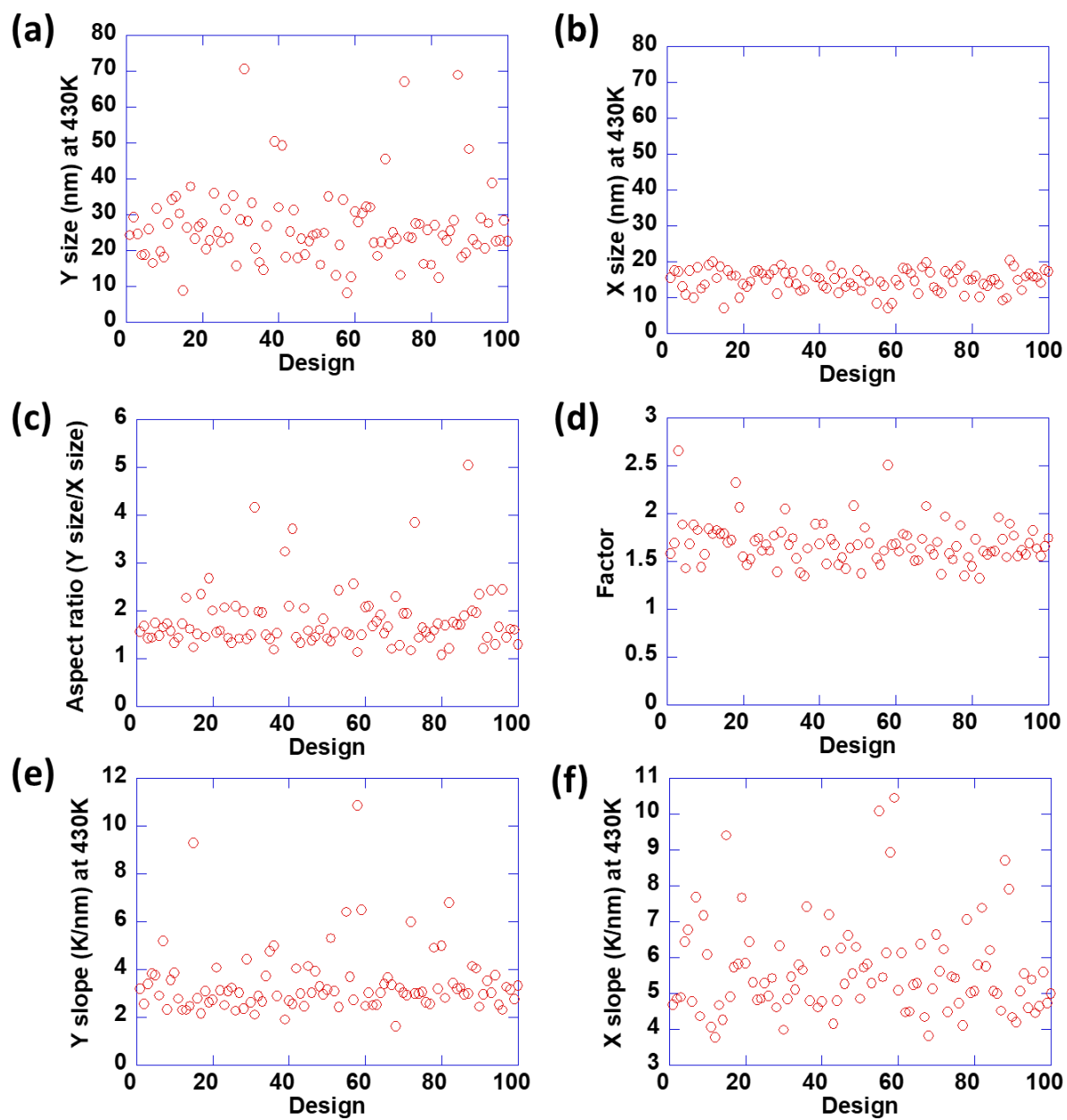


Figure 5.4 Simulation results of 100 randomized designs.

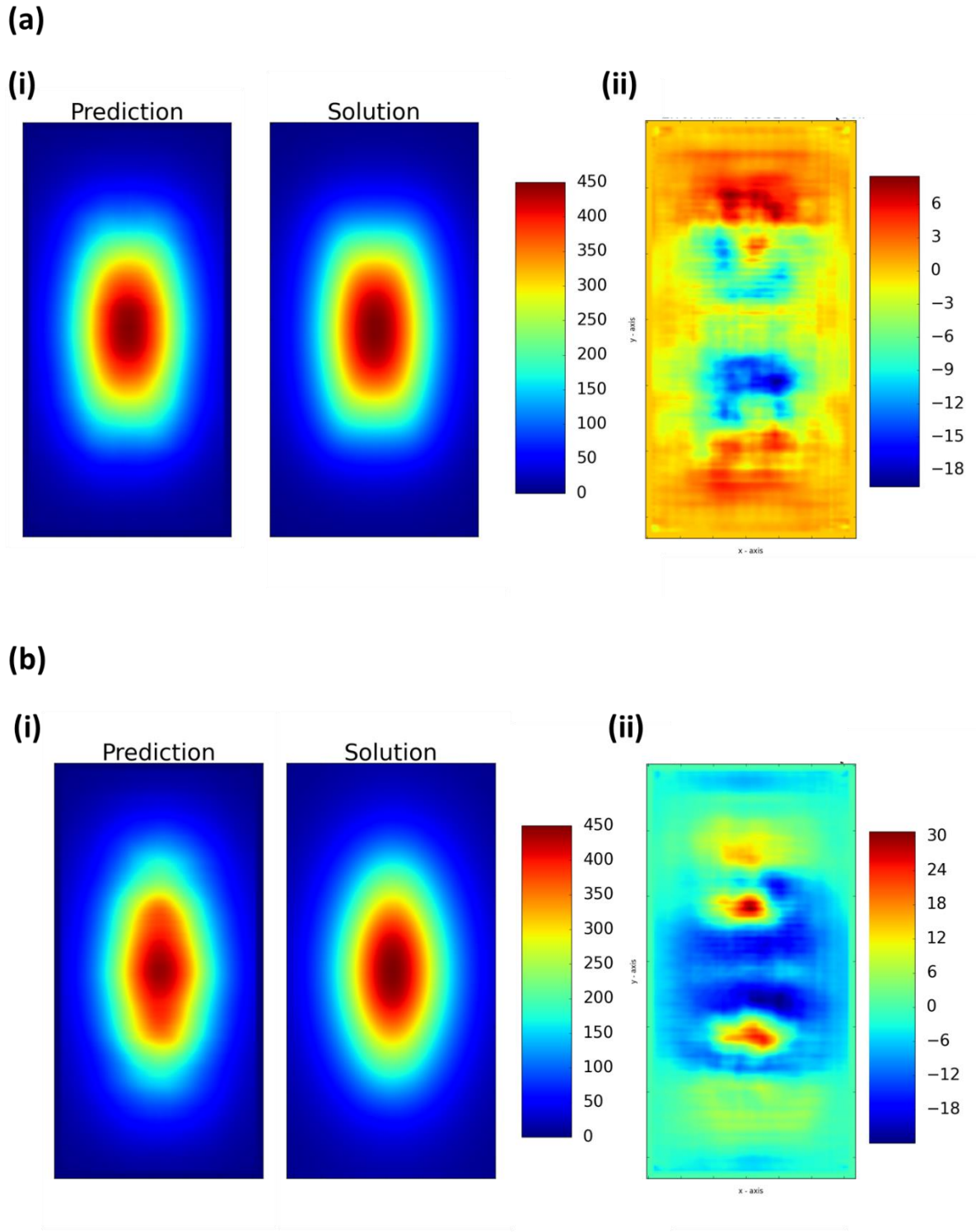


Figure 5.5 Preliminary results of neural network from validation data. (a) and (b) show the results for two NFT designs. (i) Shows the temperature rise (K) prediction from the neural network and the solution. (ii) Shows the error (K) in prediction by neural network.

5.3 Future work

For other works in this thesis, there could be number of directions for future research. For bismuth telluride selenide project, future work can explore the surface plasmon resonance of the surface state of the topological insulator $\text{Bi}_2\text{Te}_2\text{Se}$ at mid IR wavelengths. In the literature, the surface plasmon resonance in graphene at mid IR wavelengths is studied using graphene nanoribbons [144] and the results are shown in Figure 5.6. Surface plasmon resonance was observed for the light polarization perpendicular to the grating. The momentum required by the surface plasmons was provided by the grating. Figure 5.6b shows the extinction spectra ratio for two polarizations showing the surface plasmon resonance and the resonance wavelength is controlled by the width of the graphene ribbons.

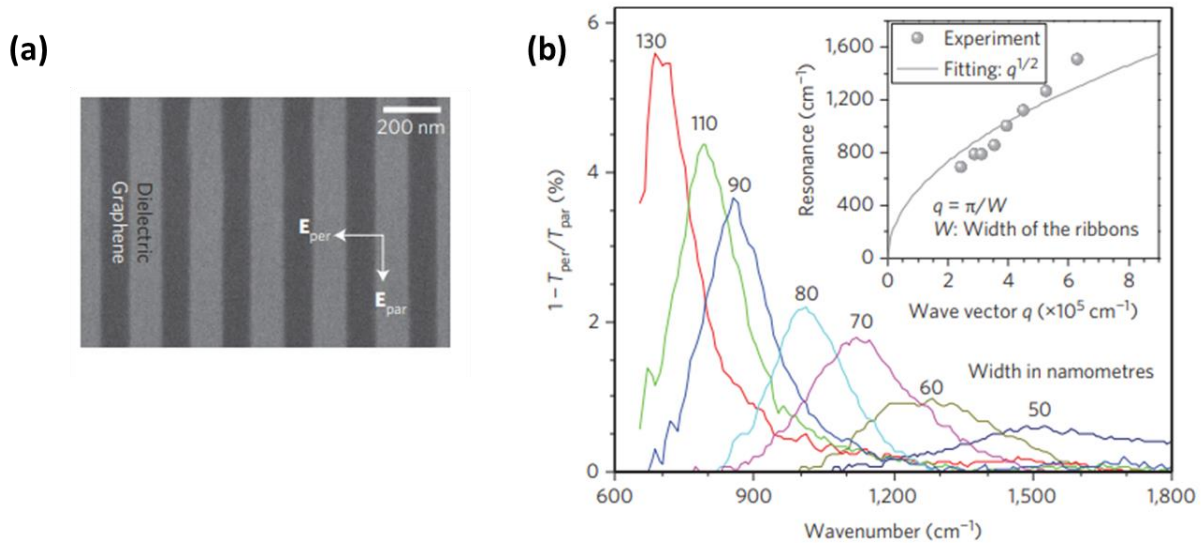


Figure 5.6 Surface plasmon resonance in graphene at mid IR wavelengths. (a) SEM image of graphene nanoribbons (b) Extinction spectra of the graphene nanoribbons. Adopted from [144].

We can extend the similar work to the topological insulator Bi₂Te₂Se. As discussed in Chapter 3, the dispersion of the surface state surface plasmon is given as,

$$v(k) = \frac{1}{2\pi} \sqrt{k} \left(\frac{e^2}{4\pi\epsilon_0\epsilon(h/2\pi)} v_f \sqrt{2\pi n_d} \right)^{1/2} \quad (5.1)$$

In our BTS, with a Fermi velocity [107] of 6×10^5 m/s and SS carrier concentration of $n_d \sim 10^{13} \text{ cm}^{-2}$ [109], [123], the width of the grating for plasmon resonance at $10.6 \mu\text{m}$ wavelength is ~ 35 nm by considering the momentum of the grating k as $\frac{\pi}{W}$. In addition to the investigation of the surface plasmon resonance of the surface state by controlling the width of the grating, we can study the surface plasmon resonance by controlling the charge density of the surface state by gating and design the devices using the surface plasmon resonance. The surface plasmon resonance at mid IR wavelengths can open up various applications including thermal radiation control.

For the work on black phosphorus, we can extend enhancing the photodetection till the bandgap of black phosphorus $\sim 4 \mu\text{m}$. Also, we can investigate a design which can enhance both photocurrent and polarization ratio in the same design. With bowtie aperture design, we could obtain high polarization selectivity but not enhanced absorption. By using a ground plate, with bowtie aperture design we can enhance both photocurrent and polarization ratio.

REFERENCES

- [1] M. L. Brongersma and V. M. Shalaev, “The Case for Plasmonics,” *Science.*, vol. 328, no. 5977, pp. 440–441, 2010, doi: 10.1126/science.1186905.
- [2] Y. Fu, "Subwavelength Optics: Theory and Technology," vol. 1. Bentham Science Publishers, 2010.
- [3] R. Zia, J. A. Schuller, A. Chandran, and M. L. Brongersma, “Plasmonics: the next chip-scale technology,” *Mater. Today*, vol. 9, no. 7–8, pp. 20–27, Jul. 2006, doi: 10.1016/S1369-7021(06)71572-3.
- [4] S. A. Maier, “Plasmonics: Fundamentals and Applications,” Springer: New York, 2007.
- [5] J. J. Mock, M. Barbic, D. R. Smith, D. A. Schultz, and S. Schultz, “Shape effects in plasmon resonance of individual colloidal silver nanoparticles,” *J. Chem. Phys.*, vol. 116, p. 6755, 2002, doi: 10.1063/1.1462610.
- [6] J. Takahara, S. Yamagishi, H. Taki, A. Morimoto, and T. Kobayashi, “Guiding of a one-dimensional optical beam with nanometer diameter,” *Opt. Lett.*, vol. 22, no. 7, p. 475, Apr. 1997, doi: 10.1364/OL.22.000475.
- [7] W. Cai, J. S. White, and M. L. Brongersma, “Compact, High-Speed and Power-Efficient Electrooptic Plasmonic Modulators,” *Nano Lett.*, vol. 9, no. 12, pp. 4403–4411, 2009, doi: 10.1021/nl902701b.
- [8] C. Hoessbacher *et al.*, “Plasmonic modulator with >170 GHz bandwidth demonstrated at 100 GBd NRZ,” *Opt. Express*, vol. 25, no. 3, p. 1762, 2017, doi: 10.1364/oe.25.001762.
- [9] A. Datta and X. Xu, “Improved Near-Field Transducer Design for Heat-Assisted Magnetic Recording,” *IEEE Trans. Magn.*, vol. 52, no. 12, pp. 1–6, Dec. 2016, doi: 10.1109/TMAG.2016.2595496.

- [10] L. Tang *et al.*, “Nanometre-scale germanium photodetector enhanced by a near-infrared dipole antenna,” *Nat. Photonics*, vol. 2, pp. 226–229, 2008, doi: 10.1038/nphoton.2008.30.
- [11] X. Wen, A. Datta, L. M. Traverso, L. Pan, X. Xu, and E. E. Moon, “High throughput optical lithography by scanning a massive array of bowtie aperture antennas at near-field,” *Sci. Rep.* 5, 16192 2015, doi: 10.1038/srep16192.
- [12] K. S. Novoselov *et al.*, “Electric field in atomically thin carbon films,” *Science*, vol. 306, no. 5696, pp. 666–669, 2004, doi: 10.1126/science.1102896.
- [13] S. V Morozov *et al.*, “Giant Intrinsic Carrier Mobilities in Graphene and Its Bilayer,” *Phys. Rev. Lett.* 100, 016602, 2008, doi: 10.1103/PhysRevLett.100.016602.
- [14] and A. K. R. Eric Pop , Vikas Varshney, “Thermal properties of graphene: Fundamentals and applications,” *MRS Bull.*, vol. 37, pp. 1273–1281, 2012, doi: 10.1557/mrs.2012.203.
- [15] C. Lee, X. Wei, J. W. Kysar, and J. Hone, “Measurement of the elastic properties and intrinsic strength of monolayer graphene,” *Science*, vol. 321, no. 5887, pp. 385–8, Jul. 2008, doi: 10.1126/science.1157996.
- [16] P. Avouris, “Graphene: Electronic and Photonic Properties and Devices,” *Nano Lett.* vol. 10, no. 11, 4285–4294 2010, doi: 10.1021/nl102824h.
- [17] F. Schwierz, “Graphene transistors,” *Nat. Nanotechnol.* vol. 5, pp 487–496, 2010, doi: 10.1038/nnano.2010.89.
- [18] D. Loc Duong, S. Joon Yun, and Y. Hee Lee, “Van der Waals Layered Materials: Opportunities and Challenges,” *ACS Nano*, vol. 11, no. 12, pp. 11803–11830, 2017, doi: 10.1021/acsnano.7b07436.

- [19] Z. Zhang *et al.*, “Direct Chemical Vapor Deposition Growth and Band-Gap Characterization of MoS₂/h-BN van der Waals Heterostructures on Au Foils,” *ACS Nano*, vol. 11, pp. 4328–4336, 2017, doi: 10.1021/acsnano.7b01537.
- [20] G. Zhang *et al.*, “Infrared fingerprints of few-layer black phosphorus,” *Nat. Commun.*, vol. 8, 2017, doi: 10.1038/ncomms14071.
- [21] H. Liu *et al.*, “Phosphorene: An Unexplored 2D Semiconductor with a High Hole Mobility,” *ACS Nano*, vol. 8, pp. 4033–4041, 2014, doi: 10.1021/nn501226z.
- [22] J. E. Moore, “The birth of topological insulators A primer on topological insulators,” *Nature* 464, pp. 194–198, 2010. doi: 10.1038/nature08916.
- [23] M. König *et al.*, “Quantum Spin Hall Insulator State in HgTe Quantum Wells” *Science.*, vol. 318, no. 5851, pp. 766–770, 2007, doi: 10.1126/science. 1148047.
- [24] C. L. Kane and E. J. Mele, “Z₂ Topological Order and the Quantum Spin Hall Effect,” 2005. Available: <https://arxiv.org/pdf/cond-mat/0506581>.
- [25] J. W. Mciver, D. Hsieh, H. Steinberg, P. Jarillo-Herrero, and N. Gedik, “Control over topological insulator photocurrents with light polarization,” *Nat. Nanotechnol.*, vol. 7, 2012, doi: 10.1038/NNANO.2011.214.
- [26] Z. Ren, A. A. Taskin, S. Sasaki, K. Segawa, and Y. Ando, “Large bulk resistivity and surface quantum oscillations in the topological insulator Bi₂Te₂Se,” *Phys. Rev. B*, vol. 82, no. 24, p. 241306, Dec. 2010, doi: 10.1103/PhysRevB.82.241306.
- [27] J. Xiong, Y. Luo, Y. Khoo, S. Jia, R. J. Cava, and N. P. Ong, “High-field Shubnikov-de Haas oscillations in the topological insulator Bi₂Te₂Se,” *Phys. Rev. B*, vol. 86, p. 45314, 2012, doi: 10.1103/PhysRevB.86.045314.

- [28] B. C. Stipe *et al.*, “Magnetic recording at 1.5Pbm-2 using an integrated plasmonic antenna,” *Nat. Photonics*, vol. 4, no. 7, pp. 484–488, 2010, doi: 10.1038/nphoton.2010.90.
- [29] W. A. Challener *et al.*, “Heat-assisted magnetic recording by a near-field transducer with efficient optical energy transfer,” *Nat. Photonics*, vol. 3, no. 4, pp. 220–224, 2009, doi: 10.1038/nphoton.2009.26.
- [30] L. Pan and D. B. Bogy, “Heat-assisted magnetic recording,” *Nat. Photonics*, vol. 3, no. April, pp. 2–3, 2009.
- [31] N. Zhou *et al.*, “Plasmonic near-field transducer for heat-assisted magnetic recording,” *Nanophotonics*, vol. 3, no. 3. pp. 141–155, Jun. 01, 2014, doi: 10.1515/nanoph-2014-0001.
- [32] R. E. Rottmayer *et al.*, “Heat-Assisted magnetic recording,” *IEEE Trans. Magn.*, vol. 42, no. 10, pp. 2417–2421, 2006, doi: 10.1109/TMAG.2006.879572.
- [33] C. Rea *et al.*, “Areal-Density Limits for Heat-Assisted Magnetic Recording and Perpendicular Magnetic Recording,” *IEEE Trans. Magn.*, vol. 52, no. 7, Jul. 2016, doi: 10.1109/TMAG.2016.2527735.
- [34] M. H. Kryder *et al.*, “Heat assisted Magnetic Recording,” *Proceedings of the IEEE*, vol. 96, no. 11, 2008.
- [35] P. K. Venuthurumilli, P. D. Ye, and X. Xu, “Plasmonic Resonance Enhanced Polarization-Sensitive Photodetection by Black Phosphorus in Near Infrared,” *ACS Nano*, vol. 12, no. 5, pp. 4861–4867, 2018, doi: 10.1021/acsnano.8b01660.
- [36] A. K. Geim and K. S. Novoselov, “The rise of graphene,” *Nat. Mater.*, vol. 6, no. 3, pp. 183–191, 2007, doi: 10.1038/nmat1849.
- [37] A. K. Geim, “Graphene: Status and Prospects,” *Science.*, vol. 324, no. 5934, pp. 1530–1534, 2009, doi: 10.1126/science.1158877.

- [38] Q. H. Wang, K. Kalantar-Zadeh, A. Kis, J. N. Coleman, and M. S. Strano, “Electronics and optoelectronics of two-dimensional transition metal dichalcogenides,” *Nat. Nanotechnol.*, vol. 7, no. 11, pp. 699–712, 2012, doi: 10.1038/nnano.2012.193.
- [39] D. Jariwala, V. K. Sangwan, L. J. Lauhon, T. J. Marks, and M. C. Hersam, “Emerging Device Applications for Semiconducting Two-Dimensional Transition Metal Dichalcogenides,” *ACS Nano*, vol. 8, no. 2, pp. 1102–1120, 2014, doi: 10.1021/nn500064s.
- [40] B. Radisavljevic, A. Radenovic, J. Brivio, V. Giacometti, and A. Kis, “Single-layer MoS₂ transistors,” *Nat. Nanotechnol.*, vol. 6, no. 3, pp. 147–150, 2011, doi: 10.1038/nnano.2010.279.
- [41] H. Liu, A. T. Neal, and P. D. D. Ye, “Channel Length Scaling of MoS₂ MOSFETs,” *ACS Nano*, vol. 6, no. 10, pp. 8563–8569, 2012, doi: 10.1021/nn303513c.
- [42] R. W. Keyes, “The Electrical properties of Black Phosphorus,” *Phys. Rev.*, vol. 92, no. 3, pp. 580–584, 1953, doi: 10.1103/PhysRev.92.580.
- [43] S. Zhang *et al.*, “Extraordinary Photoluminescence and Strong Temperature/Angle-Dependent Raman Responses in Few-Layer Phosphorene,” *ACS Nano*, vol. 8, no. 9, pp. 9590–9596, 2014, doi: 10.1021/nn503893j.
- [44] V. Tran, R. Soklaski, Y. F. Liang, and L. Yang, “Layer-controlled band gap and anisotropic excitons in few-layer black phosphorus,” *Phys. Rev. B*, vol. 89, no. 23, 2014, doi: 10.1103/PhysRevB.89.235319.
- [45] G. W. Zhang *et al.*, “Infrared fingerprints of few-layer black phosphorus,” *Nat. Commun.*, vol. 8, 2017, doi: 10.1038/ncomms14071.

- [46] K. F. Mak, C. Lee, J. Hone, J. Shan, and T. F. Heinz, “Atomically Thin MoS₂: A New Direct-Gap Semiconductor,” *Phys. Rev. Lett.*, vol. 105, no. 13, 2010, doi: 10.1103/PhysRevLett.105.136805.
- [47] A. Splendiani *et al.*, “Emerging Photoluminescence in Monolayer MoS₂,” *Nano Lett.*, vol. 10, no. 4, pp. 1271–1275, 2010, doi: 10.1021/nl903868w.
- [48] L. K. Li *et al.*, “Black phosphorus field-effect transistors,” *Nat. Nanotechnol.*, vol. 9, no. 5, pp. 372–377, 2014, doi: 10.1038/nnano.2014.35.
- [49] M. Buscema, D. J. Groenendijk, S. I. Blanter, G. A. Steele, H. S. J. van der Zant, and A. Castellanos-Gomez, “Fast and Broadband Photoresponse of Few-Layer Black Phosphorus Field-Effect Transistors,” *Nano Lett.*, vol. 14, no. 6, pp. 3347–3352, 2014, doi: 10.1021/nl5008085.
- [50] L. M. Yang *et al.*, “Few-Layer Black Phosphorous PMOSFETs with BN/Al₂O₃ Bilayer Gate Dielectric: Achieving I-on=850 μ A/ μ m, g(m)=340 μ S/ μ m, and Rc=0.58 k Ω . μ m,” *IEEE Int. Electron Devices Meet.* **2016**, 127-130.
- [51] L. Y. Bai *et al.*, “Solution-processed black phosphorus/PCBM hybrid heterojunctions for solar cells,” *J. Mater. Chem. A*, vol. 5, no. 18, pp. 8280–8286, 2017, doi: 10.1039/c6ta08140a.
- [52] M. Engel, M. Steiner, and P. Avouris, “Black Phosphorus Photodetector for Multispectral, High-Resolution Imaging,” *Nano Lett.*, vol. 14, no. 11, pp. 6414–6417, 2014, doi: 10.1021/nl502928y.
- [53] Q. S. Guo *et al.*, “Black Phosphorus Mid-Infrared Photodetectors with High Gain,” *Nano Lett.*, vol. 16, no. 7, pp. 4648–4655, 2016, doi: 10.1021/acs.nanolett.6b01977.

- [54] H. Liu, Y. Du, Y. Deng, and P. D. Ye, “Semiconducting black phosphorus: synthesis, transport properties and electronic applications,” *Chem. Soc. Rev.*, vol. 44, p. 2732, 2015, doi: 10.1039/c4cs00257a.
- [55] M. Köpf *et al.*, “Access and in situ Growth of Phosphorene-Precursor Black Phosphorus,” *Journal of crystal growth*, 405, pp.6-10, 2014, doi: 10.1016/j.jcrysgro.2014.07.029.
- [56] Z. Luo *et al.*, “Anisotropic in-plane thermal conductivity observed in few-layer black phosphorus,” *Nat. Commun.*, vol. 6, 2015, doi: 10.1038/ncomms9572.
- [57] H. T. Yuan *et al.*, “Polarization-sensitive broadband photodetector using a black phosphorus vertical p-n junction,” *Nat. Nanotechnol.*, vol. 10, no. 8, pp. 707–713, 2015, doi: 10.1038/nnano.2015.112.
- [58] J. S. Qiao, X. H. Kong, Z. X. Hu, F. Yang, and W. Ji, “High-mobility transport anisotropy and linear dichroism in few-layer black phosphorus,” *Nat. Commun.*, vol. 5, 2014, doi: 10.1038/ncomms5475.
- [59] T. Low *et al.*, “Tunable optical properties of multilayer black phosphorus thin films,” *Phys. Rev. B*, vol. 90, no. 7, 2014, doi: 10.1103/PhysRevB.90.075434.
- [60] A. Castellanos-Gomez, “Black Phosphorus: Narrow Gap, Wide Applications,” *J. Phys. Chem. Lett.* vol. 6, no. 21, 4280–4291 2015, doi: 10.1021/acs.jpclett.5b01686.
- [61] M. Razeghi and B. M. Nguyen, “Advances in mid-infrared detection and imaging: a key issues review,” *Reports Prog. Phys.*, vol. 77, no. 8, 2014, doi: 10.1088/0034-4885/77/8/082401.
- [62] Y. D. Liu and K. W. Ang, “Monolithically Integrated Flexible Black Phosphorus Complementary Inverter Circuits,” *ACS Nano*, vol. 11, no. 7, pp. 7416–7423, 2017, doi: 10.1021/acsnano.7b03703.

- [63] M. Buscema, D. J. Groenendijk, G. A. Steele, H. S. J. van der Zant, and A. Castellanos-Gomez, “Photovoltaic effect in few-layer black phosphorus PN junctions defined by local electrostatic gating,” *Nat. Commun.*, vol. 5, 2014, doi: 10.1038/ncomms5651.
- [64] L. Ye, H. Li, Z. F. Chen, and J. B. Xu, “Near-Infrared Photodetector Based on MoS₂/Black Phosphorus Heterojunction,” *Acs Photonics*, vol. 3, no. 4, pp. 692–699, 2016, doi: 10.1021/acsp Photonics.6b00079.
- [65] M. M. Adachi, A. J. Labelle, S. M. Thon, X. Lan, S. Hoogland, and E. H. Sargent, “Broadband solar absorption enhancement via periodic nanostructuring of electrodes,” *Sci. Rep.* 3, 2928, 2013, doi: 10.1038/srep02928.
- [66] G. I. Koleilat *et al.*, “Folded-light-path colloidal quantum dot solar cells,” *Sci. Rep.*, vol. 3, no. 1, pp. 1–5, Jul. 2013, doi: 10.1038/srep02166.
- [67] L. Zeng *et al.*, “Efficiency enhancement in Si solar cells by textured photonic crystal back reflector,” *Appl. Phys. Lett.*, vol. 89, no. 11, p. 111111, Sep. 2006, doi: 10.1063/1.2349845.
- [68] P. Bermel, C. Luo, L. Zeng, L. C. Kimerling, and J. D. Joannopoulos, “Improving thin-film crystalline silicon solar cell efficiencies with photonic crystals,” *Opt. Express*, vol. 15, no. 25, p. 16986, Dec. 2007, doi: 10.1364/oe.15.016986.
- [69] Y. Liu *et al.*, “Plasmon resonance enhanced multicolour photodetection by graphene,” *Nat. Commun.*, vol. 2, 2011, doi: 10.1038/ncomms1589.
- [70] Y. Liu *et al.*, “Plasmon resonance enhanced multicolour photodetection by graphene,” *Nat. Commun.*, vol. 2, no. 1, p. 579, Sep. 2011, doi: 10.1038/ncomms1589.
- [71] T. J. Echtermeyer *et al.*, “Strong plasmonic enhancement of photovoltage in graphene,” *Nat. Commun.*, vol. 2, 2011, doi: 10.1038/ncomms1464.

- [72] J. S. Miao *et al.*, “Surface Plasmon-Enhanced Photodetection in Few Layer MoS₂ Phototransistors with Au Nanostructure Arrays,” *Small*, vol. 11, no. 20, pp. 2392–2398, 2015, doi: 10.1002/sml.201403422.
- [73] E. C. Kinzel and X. F. Xu, “Extraordinary infrared transmission through a periodic bowtie aperture array,” *Opt. Lett.*, vol. 35, no. 7, pp. 992–994, 2010, doi: 10.1364/ol.35.000992.
- [74] G. P. Nordin, J. T. Meier, P. C. Deguzman, and M. W. Jones, “Micropolarizer array for infrared imaging polarimetry,” *J. Opt. Soc. Am. a-Optics Image Sci. Vis.*, vol. 16, no. 5, pp. 1168–1174, 1999, doi: 10.1364/josaa.16.001168.
- [75] P. B. Johnson and R. W. Christy, “Optical Constants of the Noble Metals,” 1972. Available: <https://journals.aps.org/prb/pdf/10.1103/PhysRevB.6.4370>.
- [76] L. Wang and X. Xu, “Spectral resonance of nanoscale bowtie apertures in visible wavelength,” *Appl. Phys. a-Materials Sci. Process.*, vol. 89, no. 2, pp. 293–297, 2007, doi: 10.1007/s00339-007-4125-3.
- [77] E. Flores, J. R. Ares, A. Castellanos-Gomez, M. Barawi, I. J. Ferrer, and C. Sanchez, “Thermoelectric power of bulk black-phosphorus,” *Appl. Phys. Lett.*, vol. 106, no. 2, 2015, doi: 10.1063/1.4905636.
- [78] Y. W. Zhang *et al.*, “Photothermoelectric and photovoltaic effects both present in MoS₂,” *Sci. Rep.*, vol. 5, 2015, doi: 10.1038/srep07938.
- [79] X. D. Xu, N. M. Gabor, J. S. Alden, A. M. van der Zande, and P. L. McEuen, “Photo-Thermoelectric Effect at a Graphene Interface Junction,” *Nano Lett.*, vol. 10, no. 2, pp. 562–566, 2010, doi: 10.1021/nl903451y.

- [80] B. C. St-Antoine, D. Menard, and R. Martel, “Position Sensitive Photothermoelectric Effect in Suspended Single-Walled Carbon Nanotube Films,” *Nano Lett.*, vol. 9, no. 10, pp. 3503–3508, 2009, doi: 10.1021/nl901696j.
- [81] T. DeBorde, L. Aspitarte, T. Sharf, J. W. Kevek, and E. D. Minot, “Photothermoelectric Effect in Suspended Semiconducting Carbon Nanotubes,” *ACS Nano*, vol. 8, no. 1, pp. 216–221, 2014, doi: 10.1021/nn403137a.
- [82] Y. X. Deng *et al.*, “Black Phosphorus-Monolayer MoS₂ van der Waals Heterojunction p-n Diode,” *ACS Nano*, vol. 8, no. 8, pp. 8292–8299, 2014, doi: 10.1021/nn5027388.
- [83] Z. F. Chen *et al.*, “Synergistic Effects of Plasmonics and Electron Trapping in Graphene Short-Wave Infrared Photodetectors with Ultrahigh Responsivity,” *ACS Nano*, vol. 11, no. 1, pp. 430–437, 2017, doi: 10.1021/acsnano.6b06172.
- [84] Z. F. Chen *et al.*, “High Responsivity, Broadband, and Fast Graphene/Silicon Photodetector in Photoconductor Mode,” *Adv. Opt. Mater.*, vol. 3, no. 9, pp. 1207–1214, 2015, doi: 10.1002/adom.201500127.
- [85] M. W. Knight, H. Sobhani, P. Nordlander, and N. J. Halas, “Photodetection with Active Optical Antennas,” *Science*, vol. 332, no. 6030, pp. 702–704, 2011, doi: 10.1126/science.1203056.
- [86] N. Youngblood and M. Li, “Ultrafast photocurrent measurements of a black phosphorus photodetector,” *Appl. Phys. Lett.*, vol. 110, no. 5, 2017, doi: 10.1063/1.4975360.
- [87] Z. Y. Fang *et al.*, “Plasmon-Induced Doping of Graphene,” *ACS Nano*, vol. 6, no. 11, pp. 10222–10228, 2012, doi: 10.1021/nn304028b.

- [88] G. Giovannetti, P. A. Khomyakov, G. Brocks, V. M. Karpan, J. van den Brink, and P. J. Kelly, “Doping graphene with metal contacts,” *Phys. Rev. Lett.*, vol. 101, no. 2, 2008, doi: 10.1103/PhysRevLett.101.026803.
- [89] P. K. Venuthurumilli, X. Wen, V. Iyer, Y. P. Chen, and X. Xu, “Near-Field Imaging of Surface Plasmons from the Bulk and Surface State of Topological Insulator Bi₂Te₂Se,” *ACS Photonics*, vol. 6, no. 10, pp. 2492–2498, Oct. 2019, doi: 10.1021/acsp Photonics.9b00814.
- [90] S. A. Maier *et al.*, “Local detection of electromagnetic energy transport below the diffraction limit in metal nanoparticle plasmon waveguides,” *Nat. Mater.*, vol. 2, pp. 229–232, 2003, doi: 10.1038/nmat852.
- [91] Y. Fang and M. Sun, “Nanoplasmonic waveguides: towards applications in integrated nanophotonic circuits,” *Light Sci. Appl.*, vol. 4, p. 294, 2015, doi: 10.1038/lsa.2015.67.
- [92] D. Rodrigo *et al.*, “Mid-infrared plasmonic biosensing with graphene,” *Science*, vol. 349, no. 6244, pp. 165–168, 2015, doi: 10.1126/science.aab0129.
- [93] D. Punj *et al.*, “A plasmonic ‘antenna-in-box’ platform for enhanced single-molecule analysis at micromolar concentrations,” *Nat. Nanotechnol.*, vol. 8, 2013, doi: 10.1038/NNANO.2013.98.
- [94] F. De Angelis *et al.*, “A Hybrid Plasmonic-Photonic Nanodevice for Label-Free Detection of a Few Molecules,” *Nano Lett.*, vol. 8, no. 8, pp. 2321–2327, 2008, doi: 10.1021/nl801112e.
- [95] H. A. Atwater and A. Polman, “Plasmonics for improved photovoltaic devices,” *Nat. Mater.*, vol. 9, no. 3, pp. 205–213, Mar. 2010, doi: 10.1038/nmat2629.

- [96] G. V. Naik, V. M. Shalaev, and A. Boltasseva, “Alternative Plasmonic Materials: Beyond Gold and Silver,” *Adv. Mater.*, vol. 25, no. 24, pp. 3264–3294, Jun. 2013, doi: 10.1002/adma.201205076.
- [97] Z. Fei *et al.*, “Gate-tuning of graphene plasmons revealed by infrared nano-imaging,” *Nature*, vol. 487, no. 7405, pp. 82–85, Jul. 2012, doi: 10.1038/nature11253.
- [98] J. Chen *et al.*, “Optical nano-imaging of gate-tunable graphene plasmons,” *Nature*, vol. 487, no. 7405, pp. 77–81, Jul. 2012, doi: 10.1038/nature11254.
- [99] J. Y. Ou, J. K. So, G. Adamo, A. Sulaev, L. Wang, and N. I. Zheludev, “Ultraviolet and visible range plasmonics in the topological insulator $\text{Bi}_{1.5}\text{Sb}_{0.5}\text{Te}_{1.8}\text{Se}_{1.2}$,” *Nat. Commun.*, vol. 5, no. 1, p. 5139, Dec. 2014, doi: 10.1038/ncomms6139.
- [100] L. Fu and C. L. Kane, “Topological insulators with inversion symmetry,” *Phys. Rev. B* 76, 045302, 2007, doi: 10.1103/PhysRevB.76.045302.
- [101] P. Roushan *et al.*, “Topological surface states protected from backscattering by chiral spin texture,” *Nature*, vol. 460, no. 7259, pp. 1106–1109, Aug. 2009, doi: 10.1038/nature08308.
- [102] P. Di Pietro *et al.*, “Observation of Dirac plasmons in a topological insulator,” *Nat. Nanotechnol.*, vol. 8, 2013, doi: 10.1038/NNANO.2013.134.
- [103] M. Zhao *et al.*, “Visible Surface Plasmon Modes in Single Bi_2Te_3 Nanoplate,” *Nano Lett.*, vol. 15, no. 12, pp. 8331–8335, Dec. 2015, doi: 10.1021/acs.nanolett.5b03966.
- [104] A. M. Dubrovkin *et al.*, “Visible Range Plasmonic Modes on Topological Insulator Nanostructures,” *Adv. Opt. Mater.*, vol. 5, no. 3, p. 1600768, Feb. 2017, doi: 10.1002/adom.201600768.

- [105] J. Yuan *et al.*, “Infrared Nanoimaging Reveals the Surface Metallic Plasmons in Topological Insulator,” *ACS Photonics*, vol. 4, no. 12, pp. 3055–3062, 2017 doi: 10.1021/acsp Photonics.7b00568.
- [106] P. Gehring, B. F. Gao, M. Burghard, and K. Kern, “Growth of High-Mobility Bi₂Te₂Se Nanoplatelets on hBN Sheets by van der Waals Epitaxy,” *Nano Lett.*, vol. 12, no. 10, pp. 5137–5142, 2012, doi: 10.1021/nl3019802.
- [107] H. Cao *et al.*, “Controlling and distinguishing electronic transport of topological and trivial surface states in a topological insulator,” Sep. 2014. Available: <http://arxiv.org/abs/1409.3217>.
- [108] D. K. Gramotnev and S. Bozhevolnyi, “Plasmonics beyond the diffraction limit,” *Nat. Photonics*, vol. 4, 2010, doi: 10.1038/nphoton.2009.282.
- [109] Z. Luo *et al.*, “Large Enhancement of Thermal Conductivity and Lorenz Number in Topological Insulator Thin Films,” *ACS Nano*, vol. 12, no. 2, pp. 1120–1127, Feb. 2018, doi: 10.1021/acsnano.7b06430.
- [110] P. G. Etchegoin, E. C. Le Ru, and M. Meyer, “An analytic model for the optical properties of gold,” *J. Chem. Phys.*, vol. 125, no. 16, p. 164705, Oct. 2006, doi: 10.1063/1.2360270.
- [111] G. E. Jellison and F. A. Modine, “Parameterization of the optical functions of amorphous materials in the interband region,” *Appl. Phys. Lett.*, vol. 69, p. 371, 1996, doi: 10.1063/1.118064.
- [112] H. Chen and W. Z. Shen, “Perspectives in the characteristics and applications of Tauc-Lorentz dielectric function model,” *Eur. Phys. J. B*, vol. 43, pp. 503–507, 2005, doi: 10.1140/epjb/e2005-00083-9.

- [113] “Introduction,” in *Kramers-Kronig Relations in Optical Materials Research*, Berlin/Heidelberg: Springer-Verlag, pp. 1–3.
- [114] J. Yin *et al.*, “Plasmonics of topological insulators at optical frequencies,” *NPG Asia Mater.*, vol. 9, no. 8, p. e425, Aug. 2017, doi: 10.1038/am.2017.149.
- [115] B. Wang, L. Aigouy, E. Bourhis, J. Gierak, J. P. Hugonin, and P. Lalanne, “Efficient generation of surface plasmon by single-nanoslit illumination under highly oblique incidence,” *Appl. Phys. Lett.*, vol. 94, no. 1, p. 011114, Jan. 2009, doi: 10.1063/1.3068747.
- [116] Y. Li, N. Zhou, E. C. Kinzel, X. Ren, and X. Xu, “The origin of interferometric effect involving surface plasmon polariton in scattering near-field scanning optical microscopy,” *Opt. Express*, vol. 22, no. 3, p. 2965, Feb. 2014, doi: 10.1364/OE.22.002965.
- [117] K. G. Lee *et al.*, “Vector field mapping of local polarization using gold nanoparticle functionalized tips: independence of the tip shape,” Vol. 15, Issue 23, pp. 14993-15001 2007, doi.org/10.1364/OE.15.014993
- [118] J. T. Krug, E. J. Sánchez, and X. S. Xie, “Design of near-field optical probes with optimal field enhancement by finite difference time domain electromagnetic simulation,” *J. Chem. Phys.*, vol. 116, p. 10895, 2002, doi: 10.1063/1.1479723.
- [119] A. Akrap *et al.*, “Optical properties of Bi₂Te₂Se at ambient and high pressures,” *Phys. Rev. B*, vol. 86, p. 235207, 2012, doi: 10.1103/PhysRevB.86.235207.
- [120] G. Cheng *et al.*, “Nano-imaging of an edge-excited plasmon mode in graphene,” *Nanoscale*, vol. 10, no. 34, pp. 16314–16320, Aug. 2018, doi: 10.1039/C8NR04623A.
- [121] R. E. V Profumo, R. Asgari, M. Polini, and A. H. Macdonald, “Double-layer graphene and topological insulator thin-film plasmons,” *Phys. Rev. B*, vol. 85, p. 85443, 2012, doi: 10.1103/PhysRevB.85.085443.

- [122] T. Stauber, “Plasmonics in Dirac systems: from graphene to topological insulators,” *J. Phys. Condens. Matter*, vol. 26, no. 12, p. 123201, Mar. 2014, doi: 10.1088/0953-8984/26/12/123201.
- [123] V. Iyer, Y. P. Chen, and X. Xu, “Ultrafast Surface State Spin-Carrier Dynamics in the Topological Insulator $\text{Bi}_2\text{Te}_2\text{Se}$,” *Phys. Rev. Lett.*, vol. 121, no. 2, p. 026807, Jul. 2018, doi: 10.1103/PhysRevLett.121.026807.
- [124] F. Neubrech, A. Pucci, T. W. Cornelius, S. Karim, A. García-Etxarri, and J. Aizpurua, “Resonant Plasmonic and Vibrational Coupling in a Tailored Nanoantenna for Infrared Detection,” 2008, doi: 10.1103/PhysRevLett.101.157403.
- [125] I. Appelbaum, H. D. Drew, and M. S. Fuhrer, “Proposal for a topological plasmon spin rectifier,” *Appl. Phys. Lett.*, vol. 98, p. 23103, 2011, doi: 10.1063/1.3541545.
- [126] W. A. Challener and A. V. Itagi, “Near-Field Optics for Heat-Assisted Magnetic Recording (Experiment, Theory, and Modeling),” Springer, New York, NY, 2009, pp. 53–111.
- [127] N. Zhou, L. M. Traverso, and X. Xu, “Power delivery and self-heating in nanoscale near field transducer for heat-assisted magnetic recording,” *Nanotechnology*, vol. 26, no. 13, p. 134001, Mar. 2015, doi: 10.1088/0957-4484/26/13/134001.
- [128] N. Zhou, E. C. Kinzel, and X. Xu, “Nanoscale ridge aperture as near-field transducer for heat-assisted magnetic recording,” *Appl. Opt.*, vol. 50, no. 31, pp. G42–G46, Nov. 2011, doi: 10.1364/AO.50.000G42.
- [129] X. Shi and L. Hesselink, “Mechanisms for enhancing power throughput from planar nano-apertures for near-field optical data storage,” *Jpn. J. Appl. Phys.*, vol. 41, pp. 1632–1635, 2002, doi: 10.1143/jjap.41.1632.

- [130] A. Datta and X. Xu, “Comparative study of optical near-field transducers for heat-assisted magnetic recording,” *Opt. Eng.*, vol. 56, no. 12, p. 121906, May 2017, doi: 10.1117/1.oe.56.12.121906.
- [131] N. Abadía *et al.*, “Optical and thermal analysis of the light-heat conversion process employing an antenna-based hybrid plasmonic waveguide for HAMR,” *Opt. Express*, vol. 26, no. 2, p. 1752, Jan. 2018, doi: 10.1364/oe.26.001752.
- [132] J. Andkjær, S. Nishiwaki, T. Nomura, and O. Sigmund, “Topology optimization of grating couplers for the efficient excitation of surface plasmons,” *J. Opt. Soc. Am. B*, vol. 27, no. 9, p. 1828, Sep. 2010, doi: 10.1364/josab.27.001828.
- [133] R. E. Christiansen, J. Vester-Petersen, S. P. Madsen, and O. Sigmund, “A non-linear material interpolation for design of metallic nano-particles using topology optimization,” *Comput. Methods Appl. Mech. Eng.*, vol. 343, pp. 23–39, Jan. 2019, doi: 10.1016/j.cma.2018.08.034.
- [134] S. Bhargava and E. Yablonovitch, “Lowering HAMR near-field transducer temperature via inverse electromagnetic design,” *IEEE Trans. Magn.*, vol. 51, no. 4, Apr. 2015, doi: 10.1109/TMAG.2014.2355215.
- [135] C. Huber *et al.*, “Topology optimized and 3D printed polymer-bonded permanent magnets for a predefined external field,” *J. Appl. Phys.*, vol. 122, no. 5, p. 053904, Aug. 2017, doi: 10.1063/1.4997441.
- [136] J. S. Jensen and O. Sigmund, “Topology optimization for nano-photonics,” *Laser Photon. Rev.*, vol. 5, no. 2, pp. 308–321, Mar. 2011, doi: 10.1002/lpor.201000014.

- [137] Y. Deng, Z. Liu, C. Song, J. Wu, Y. Liu, and Y. Wu, “Topology Optimization-Based Computational Design Methodology for Surface Plasmon Polaritons,” *Plasmonics*, vol. 10, no. 3, pp. 569–583, Jun. 2015, doi: 10.1007/s11468-014-9842-9.
- [138] C. -b. Rong *et al.*, “Size-Dependent Chemical and Magnetic Ordering in L10-FePt Nanoparticles,” *Adv. Mater.*, vol. 18, no. 22, pp. 2984–2988, Nov. 2006, doi: 10.1002/adma.200601904.
- [139] Z. Zeng and X. Xu, “Topology Optimization of Plasmonics with the FDTD method in Frequency Domain,” Jul. 2020. Available: <http://arxiv.org/abs/2007.11442>.
- [140] A. Datta and X. Xu, “Infrared Near-Field Transducer for Heat-Assisted Magnetic Recording,” *IEEE Trans. Magn.*, vol. 53, no. 12, Dec. 2017, doi: 10.1109/TMAG.2017.2743078.
- [141] Z. Zeng, “Sensitivity Analysis and Topology Optimization in Plasmonics,” Purdue University Graduate School, Aug. 2019. doi: 10.25394/PGS.8945135.V1.
- [142] R. H. Byrd, P. Lu, J. Nocedal, and C. Zhu, “A Limited Memory Algorithm for Bound Constrained Optimization,” *SIAM J. Sci. Comput.*, vol. 16, no. 5, pp. 1190–1208, Sep. 1995, doi: 10.1137/0916069.
- [143] Incropera, Frank P. Fundamentals of Heat and Mass Transfer. 7th ed. John Wiley, 2011.
- [144] H. Yan *et al.*, “Damping pathways of mid-infrared plasmons in graphene nanostructures,” *Nat. Photonics*, vol. 7, no. 5, pp. 394–399, May 2013, doi: 10.1038/nphoton.2013.57.

VITA

Prabhu Kumar Venuthurumilli received his B. Tech. (Honours) degree in mechanical engineering from Indian Institute of Technology, Madras, in 2014. He is currently a PhD candidate in the Department of Mechanical Engineering at Purdue University, working with Prof. Xianfan Xu. He is the recipient of Ross fellowship from Purdue University. His research interests include applications of plasmonics in 2D materials: semiconductors, topological insulators, and heat assisted magnetic recording.

PUBLICATIONS

1. **Venuthurumilli, P. K.**; Ye, P. D.; Xu, X. Plasmonic Resonance Enhanced Polarization-Sensitive Photodetection by Black Phosphorus in Near Infrared. *ACS Nano*, **2018**, *12*, 4861–4867.
2. **Venuthurumilli, P. K.**; Wen, X.; Iyer, V.; Chen, Y.; Xu, X. Near-Field Imaging of Surface Plasmons from the Bulk and Surface State of Topological Insulator Bi₂Te₂Se. *ACS Photonics*, **2019**, *6*, 2492–2498.
3. **Venuthurumilli, P. K.***; Zeng, Z.*; Xu, X. Inverse Design of Near-Field Transducer for Heat Assisted Magnetic Recording Using Topology Optimization (Submitted - * denotes equal contribution)
4. Zeng, Z.; **Venuthurumilli, P. K.**; Xu, X. Inverse Design of Plasmonic Structures with FDTD. (Submitted)
5. Qiu, G.; Huang, S.; Segovia, M.; **Venuthurumilli, P. K.**; Wang, Y.; Wu, W.; Xu, X.; Ye, P. D. Thermoelectric Performance of 2D Tellurium with Accumulation Contacts. *Nano Letters*, **2019**, *19*, 1955–1962.
6. Salihoglu, H., Nam, W., Traverso, L., Segovia, M., **Venuthurumilli, P. K.**, Liu, W., Wei, Y., Li, W., & Xu, X. Near-Field Thermal Radiation between Two Plates with Sub-10 nm Vacuum Separation. *Nano Letters*, **2020**, *20*, 6091–6096.
7. **Venuthurumilli, P. K.**; Wen, X.; Iyer, V.; Chen, Y.; Xu, X. Imaging of Surface Plasmons from the Bulk and Surface State of Topological Insulator Bi₂Te₂Se. *FIO Conference*, **2019**.
8. Deng, Y.; **Venuthurumilli, P. K.**; Luo, Z.; Conrad, N.; Xu, X.; Ye, P. D. Plasmonic Enhanced Polarization Sensitive Black Phosphorus Photodetection Device. *Device Research Conference, IEEE*, **2017**, 1–2.